UNIVERSIDAD NACIONAL AUTÓNOMA DE MÉXICO

PROGRAMA DE MAESTRÍA Y DOCTORADO EN INGENIERÍA

FACULTAD DE INGENIERÍA

DYNAMICS OF NON-NEWTONIAN VORTEX RINGS

T E S I S

QUE PARA OPTAR POR EL GRADO DE:

DOCTOR EN INGENIERÍA

MECÁNICA - TERMOFLUIDOS

P R E S E N T A :

CARLOS ALBERTO PALACIOS MORALES

TUTOR:
DR. ROBERTO ZENIT CAMACHO

MÉXICO, D.F. AGOSTO 2010

JURADO ASIGNADO:

Presidente:	Dr. Jaime Cervantes de Gortari
Secretario:	Dr. Francisco Javier Solorio Ordaz
Vocal:	Dr. José Roberto Zenit Camacho
1er Suplente:	Dr. Gabriel Ascanio Gasca
2do. Suplente	Dra. Catalina Elizabeth Stern Forgach

Lugar o lugares donde se realizó la tesis:

INSTITUTO DE INVESTIGACIONES EN MATERIALES

TUTOR DE TESIS:

DR. ROBERTO ZENIT CAMACHO

_____

FIRMA

Universidad Nacional Autónoma de México

Programa de maestría y doctorado en Ingeniería

Dynamics of Non-Newtonian vortex rings

Tesis

que para obtener el grado de

Doctor en Ingeniería Mecánica

presenta

Carlos Alberto Palacios Morales

Director de tesis: Dr. Roberto Zenit Camacho

México D.F., Agosto de 2010

A mi esposa: Katya
Con todo mi cariño.

A mis padres: Laura y Hernán.
Por todo su amor y apoyo incondicional.

Agradecimientos

En esta aventura de realizar un doctorado, quiero agradecer en primer lugar a la Universidad Nacional Autónoma de México por darme la oportunidad de aprender un sin número de conocimientos tanto en el ámbito profesional como en el personal. Concluyo con éxito, satisfacción y también con mucha nostalgia este último ciclo en mi carrera estudiantil. Puedo afirmar que estos años de estudio e investigación han valido la pena y me han permitido crecer individualmente.

Agradezco de todo corazón a mis padres Laura y Hernán por su apoyo incondicional, su protección y su amor; pero sobretodo por la confianza que siempre han depositado en mi. Agradezco a mis hermanos Yanni y Hernán por su cariño y por toda la ayuda que me han brindado. Agradezco infinitamente a mi esposa Katya por impulsarme a seguir siempre adelante, por todo su amor, por su paciencia y por la ayuda en la elaboración de esta tesis.

Agradezco a mi tutor, Roberto Zenit, por darme su voto de confianza, por darme la oportunidad de trabajar en este proyecto tan interesante, pero sobretodo agradezco todos sus consejos, su enseñanza y ante todo su amistad, la cual valoro infinitamente. En particular quiero mencionar la valiosa aportación de mi colega Ian Monsiváis quien participó en las primeras etapas de la presente investigación. Agradezco a todos los que directa o indirectamente contribuyeron a la elaboración de la presente tesis.

A los miembros del jurado, los doctores Jaime Cervantes de Gortari, Francisco Solorio, Catalina Stern y Gabriel Ascanio, agradezco sus comentarios, críticas y el enriquecimiento general al presente trabajo. Agradezco a la Dirección General de Estudios de Posgrado de la UNAM por la beca que me otorgó para poder realizar los estudios de doctorado. A mi querida Facultad de Ingeniería, la cual siempre recordaré con mucho orgullo.

A mis amigos de toda la vida, Angel, Daniel, Nacho, Fabiola, Lina y Paty que siempre han creído en mi, han estado y siempre estarán en los momentos importantes de mi vida. A todos mis compañeros y colegas del Instituto de Investigaciones en Materiales, muchos de los cuales contribuyeron a la elaboración de la presente tesis y cuya lista es interminable; gracias por su compañía, apoyo y por todos los ratos inolvidables.

Contents

Resumen

Se estudió la dinámica de formación y evolución de vórtices anulares Newtonianos y no Newtonianos generados en un arreglo pistón-cilindro. La razón entre el desplazamiento del pistón L_m y el diámetro interno del cilindro D_0, así como la velocidad media del pistón U_p determinan las propiedades y evolución del vórtice. Se presentan experimentos con diferentes condiciones: velocidad de traslación del pistón, razón de empuje L_m/D_0 y líquidos con propiedades reológicas diferentes. Se obtuvieron mediciones del campo vectorial de velocidades en 2D utilizando la técnica PIV. La circulación del vórtice Γ se calculó usando un esquema de identificación de vórtices (criterio Q). El número de Reynolds se define como $Re_0 = D_0 U_p/\nu$, donde ν es la viscosidad cinemática del fluido. Para el caso Newtoniano, se realizaron mediciones en el rango $150 < Re_0 < 2000$. Se generaron vórtices anulares usando líquidos adelgazantes en el rango $138 < Re_0 < 616$. El número de Reynolds para estos vórtices se calculó en términos de los parámetros del modelo de 'ley de potencia': el índice de potencia n y la consistencia m.

Los resultados experimentales indican que la circulación del vórtice aumenta con la razón de empuje hasta llegar a un valor crítico de L_m/D_0 arriba del cual no se puede incrementar y permanece constante. En general, el valor crítico de L_m/D_0 depende del número de Reynolds. La razón de empuje crítica es 4 para $Re_0 \sim \mathrm{O}(100)$, 8 para $Re_0 \sim \mathrm{O}(1000)$ y 10 para $Re_0 = 2000$. Para números de Reynolds mayores, la velocidad de propagación del vórtice es mayor, pero su circulación disminuye para un mismo L_m/D_0. Encontramos que es posible generar vórtices más gruesos al disminuir Re_0; por tanto, la circulación en su centro aumenta. Considerando diferentes líquidos adelgazantes que se comportan de acuerdo a un modelo de ley de potencia manteniendo Re_0 constante, la circulación del vórtice disminuye con el índice de potencia n. Mostramos que la circulación total generada en la descarga del cilindro es menor con los líquidos más adelgazantes; por tanto, la circulación del vórtice disminuye también. Un valor de circulación adimensional de $\Gamma/D_0 U_p \approx 2$ puede indicar una condición

de saturación arriba de la cual no es posible incrementar la circulación del vórtice para cualquier número de Reynolds.

Abstract

The dynamics of formation and evolution of Newtonian and non-Newtonian vortex rings generated in a piston-cylinder arrangement is studied. The ratio of the piston displacement L_m to the internal cylinder diameter D_0, as well as the mean piston velocity U_p determine the vortex properties and evolution. Experiments with different conditions are presented: translation velocity of the piston, stroke ratios L_m/D_0 and liquids with different rheological properties. Measurements of the 2D velocity field were obtained with a PIV technique. The vortex circulation Γ was computed considering a vortex identification scheme (Q criterion). The Reynolds number (Newtonian vortex rings), defined as $Re_0 = D_0 U_p/\nu$, where ν is the kinematic viscosity of the fluid, was in the range $150 < Re_0 < 2000$. We also generated vortex rings using shear-thinning liquids in the range $138 < Re_0 < 616$. The Reynolds number for these vortices is computed in terms of the 'power-law' model parameters: the power index n and the consistency m.

The experimental results indicate that the vortex circulation increases with the stroke ratio until it reaches a critical value above which the circulation inside the vortex cannot increase and remains constant. In general, the critical L_m/D_0 depends on the Reynolds number. The critical stroke ratio is 4 for $Re_0 \sim \mathrm{O}(100)$, 8 for $Re_0 \sim \mathrm{O}(1000)$ and as large as 10 for $Re_0 \approx 2000$. As the Reynolds number increases the vortex propagation velocity increases but the vortex ring circulation decreases for the same L_m/D_0. We found that it is possible to generate thick vortices as Re_0 decreases; hence, the circulation in their core also increases. Considering different power-law liquids (shear-thinning) and fixed Reynolds number, the vortex circulation decreases with the power index n. We show that the total circulation ejected from the cylinder is reduced for more shear-thinning liquids; thus, the circulation confined inside the vortex ring, is reduced too. A value of the non-dimensional circulation $\Gamma/D_0 U_p \approx 2$ may indicate a saturation condition beyond which it is not possible to increase the vortex circulation for any Reynolds number.

Color Plates

Figure 1: The volcano, Mount Etna (Italy), blows 200m diameter steam rings.

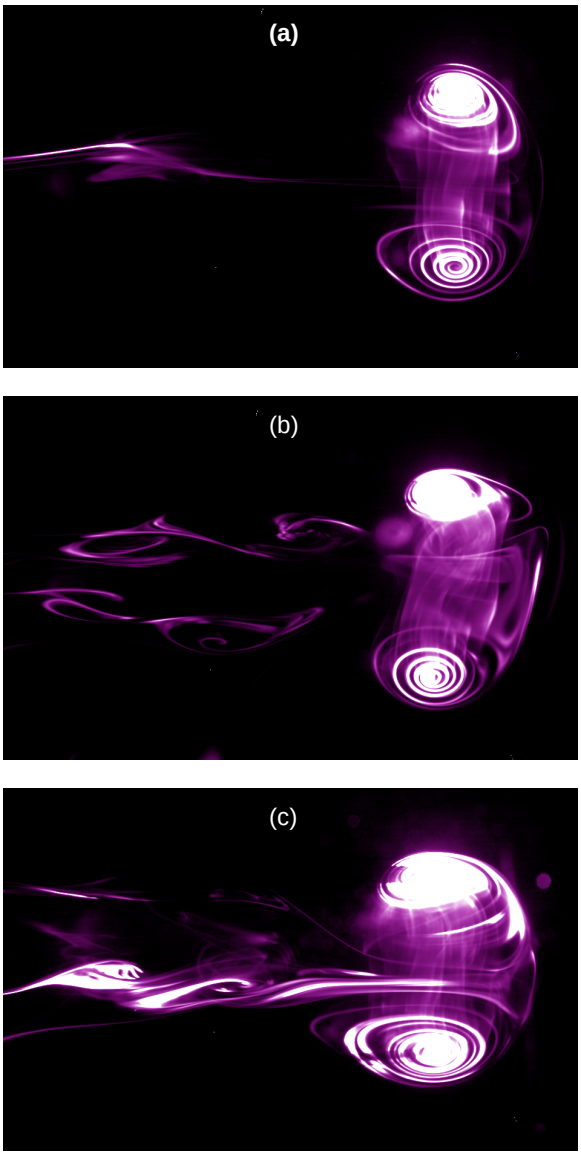

Figure 2: Vortex rings by LIF (Laser-induced fluorescence). Stroke ratios: (a) $L_m/D_0 = 2$ (b) $L_m/D_0 = 4$ (c) $L_m/D_0 = 6$. Palacios-Morales & Zenit (2008).

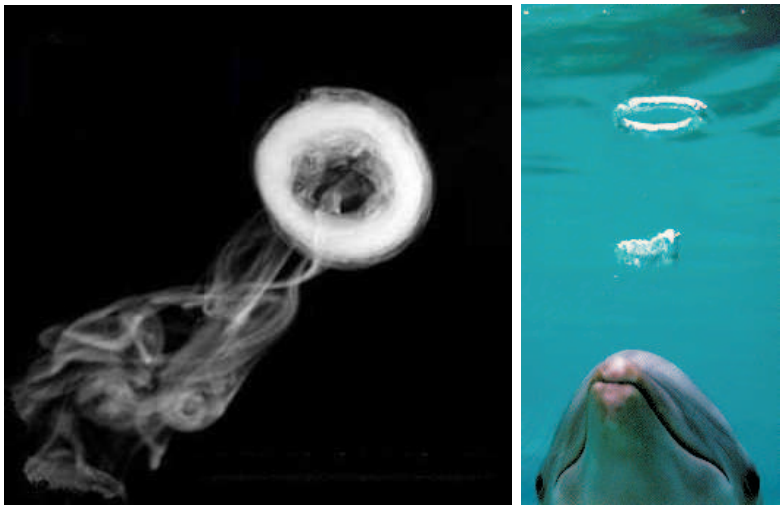

Figure 3: (a) A smoke ring (b) Dolphin blowing bubble rings.

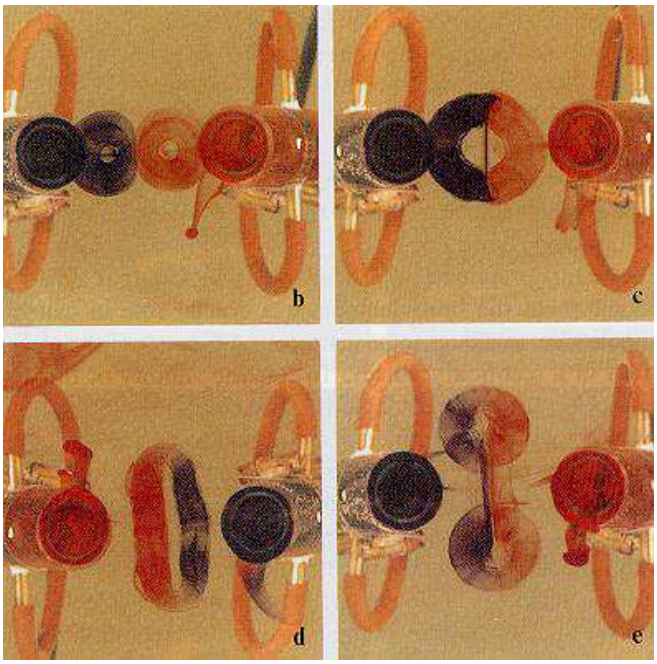

Figure 4: A series of front-view photographs showing different stages of collision of two vortex rings at an angle. Lim (1989).

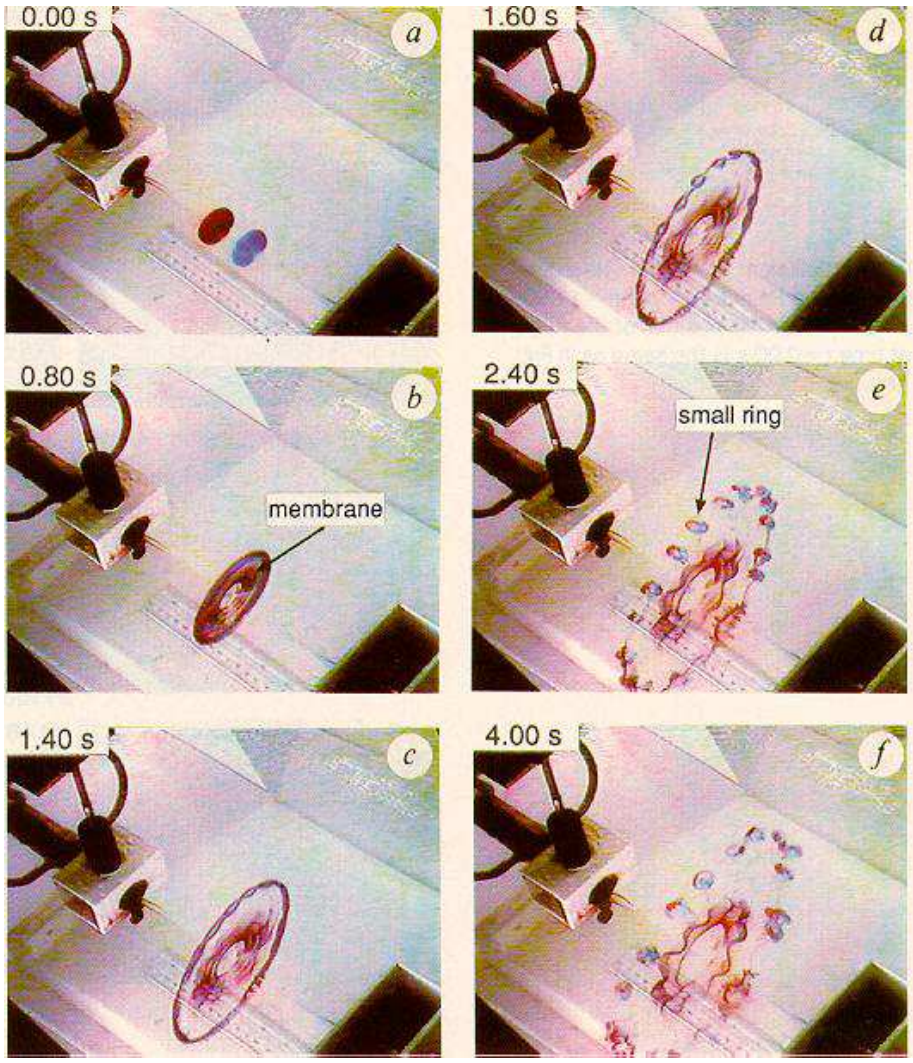

Figure 5: Head-on collision of two vortex rings (color dyes in water). Lim & Nickels (1992).

Chapter 1

Introduction

The vortex ring is one of the most common fluid structure in nature (see Fig. 1.1). One can observe a ring, for example, if a person breathes out a puff of smoke through rounded lips. Vortex rings are generated in any starting propulsion jet. It is possible to see vortex rings coming from a car o tractor tailpipe. Many biological flows are characterized by vortex production and vortex shedding. In animal locomotion, the production of coherent structures such as vortex rings is common; these structures have been found in squid jet propulsion by Anderson & Grosenbaugh (2005) as well as Bartol *et al.* (2009 a,b). Dabiri *et al.* (2006) studied a species of jellyfish that creates a single vortex ring. This kind of vortex can also be seen in internal biological flows, such like the discharge of blood into the heart left ventricle (Gharib *et al.* 2006). In the laboratory vortex rings can be generated by the movement of a piston which pushes a column of fluid inside a cylinder through an orifice or nozzle. To characterize the flow, the Reynolds number (for Newtonian vortex rings) can be defined in two different forms. Considering the inner diameter of the cylinder exit D_0, the piston mean velocity (during discharge) U_p and the kinematic viscosity of the liquid, we define $Re_0 = D_0 U_p/\nu$. On the other hand, considering the vortex ring diameter D_v (distance between centers of the upper and lower half plane) and the vortex instantaneous propagation velocity U_v, the Reynolds number can be defined as $Re_v = D_v U_v/\nu$. Some authors have defined the Reynolds number as the relation between the vortex ring circulation (Eq. 1.7) and the fluid viscosity: $Re = \Gamma/\nu$.

In the last thirty years there has been an increased interest in the study of vortex rings. The formation and evolution of vortex rings have been the main subjects of interest. In the literature it is possible to find theoreti-

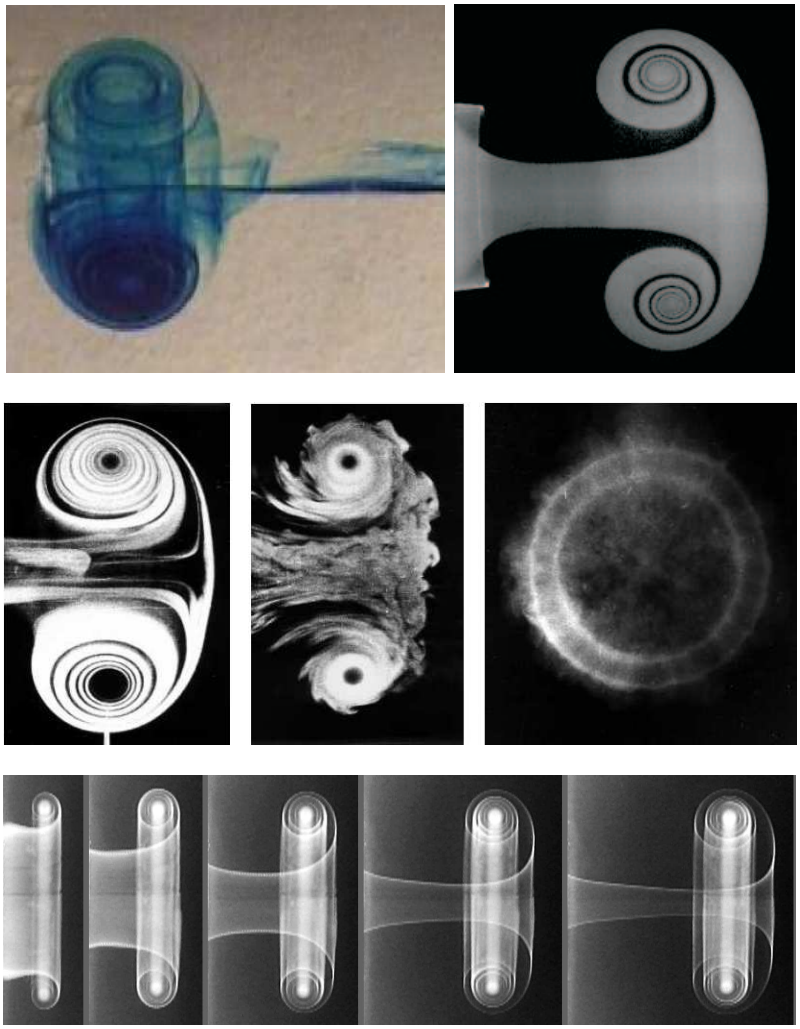

Figure 1.1: Top left: visualization using ink (Palacios C. [1]). Top right: LIF technique, (Krueger P. [2]). Middle: Smoke visualization (Akhmetov 2001). Bottom: Vortex evolution (Adhikari & Lim [3]).

cal, numerical and experimental studies. Many of the early works can be found in the reviews of Shariff & Leonard (1992) and Lim & Nickels (1995). Saffman (1992) presented different theoretical studies of axisymmetric vortex rings; in particular he gave different relations to obtain the propagation velocity of thin cored rings. For the case of laminar vortex rings, in particular for those generated by a piston-cylinder arrangement, there are many experimental studies: Maxworthy (1977), Didden (1979), Glezzer (1988) Glezer & Coles (1990), Weigand & Gharib (1997) and Gharib *et al.* (1998). Maxworthy (1977) carried out experimental measurements through flow visualization and laser Doppler techniques; he observed that the formation process is strongly Reynolds number dependent. Didden (1979) presented flow visualizations of the formation of vortex rings and gave information of the role of the internal and external boundary layers in the formation process and circulation of the vortex ring. Glezeer (1988) studied vortex ring formation with different piston velocities as a function of time called the 'velocity program'. He analyzed the conditions under which transition from laminar to turbulent vortex rings is produced. Weigand & Gharib (1997) studied the vortex ring properties for different Re numbers using the particle image velocimetry (PIV) technique. They found that the vorticity distributions in the vortex core have self-similar Gaussian profiles.

The first numerical work is probably the simulation of a vortex ring using a spectral method by Stanaway *et al.* (1988). The numerical works of Nitsche & Kransy(1994) and James & Madnia (1996) simulated the vortex ring during formation. Using a vortex sheet model Nitsche & Krasny obtained results which proved a good global agreement with Didden's (1979) experiments; in particular with his vortex ring visualizations. James & Madnia (1996) used the Navier-Stokes equations to simulate the formation and propagation of the vortex ring; they also compared their results with those from Didden experiments and concluded that the total circulation in the flow field of the ring is the same for different nozzle exit configurations. Rosenfeld *et al.* (1998) used the Navier-Stokes equation to simulate the vortex ring formation and evolution for relatively long discharge times (long displacement of the piston) and compared their numerical results with the Gharib *et al.* (1998) experiments. They presented results for different geometrical configurations and piston velocity programmes. Finally, Mohseni *et al.* (2001) simulated the formation of vortex rings that are generated by

[1]Rheology Lab., Instituto de Investigaciones en Materiales, UNAM.
[2]Experimental fluid dynamics Lab., Southern Methodist University.
[3]Fluid mechanics group, National University of Singapore.

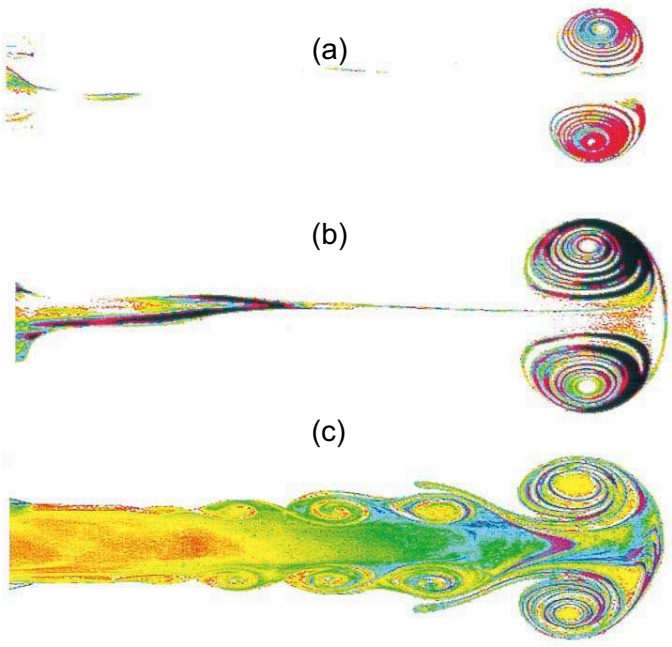

Figure 1.2: Visualization of vortex rings. Taken from Gharib *et al.* (1998) (a) $L_m/D_0 = 2$ (b) $L_m/D_0 = 3.8$ (c) $L_m/D_0 = 14.5$. Pictures are taken at $\bar{U}_p t/D = 8$.

applying a non-conservative force of long duration.

1.1 Formation number

The seminal paper of Gharib *et al.* (1998) revived the interest in the study of vortex ring formation. Their results are of direct relevance to the present thesis. They generated vortex rings using a piston-cylinder arrangement in a water tank and obtained the velocity field by the PIV technique. They found that the circulation that a vortex ring could attain was finite: there was a maximum amount of fluid vorticity that could be contained within a ring. The parameter that determined whether the circulation had reached a maximum was the piston "stroke ratio" L/D_0, where $L = L(t)$ is the piston displacement and D_0 is the inner diameter of the cylinder exit. The stroke ratio is equivalent to the non-dimensional time

$$t^* = \frac{\overline{U_p} t}{D_0} = \frac{L}{D_0} \tag{1.1}$$

referred as *formation time* by Gharib *et al.* (1998). $\overline{U_p}$ is the mean piston velocity during fluid discharge and t is the discharge time. The "total stroke ratio" is equivalent to the total non-dimensional time

$$T^* = \frac{\overline{U_p} T_0}{D_0} = \frac{L_m}{D_0} \tag{1.2}$$

where L_m is the total piston displacement and T_0 is the total discharge time. They found that for values smaller than $L_m/D_0 \approx 4$, a solitary vortex ring was formed; for larger values of L_m/D_0, a leading vortex followed by a trailing jet or secondary vortices was observed (see Fig. 1.2). The circulation contained within the leading vortex ring could not be further increased even if L_m/D_0 kept on increasing. The critical value of L_m/D_0 in which the transition between these two states occurs was called the **formation number**. Considering the cylinder diameter and the piston mean velocity, Gharib *et al.* (1998) presented results of flows with $Re_0 = 1905$ and $Re_0 = 3810$. For different experimental configurations the formation number lay in the range of 3.6 to 4.5.

Some authors have discussed that changing the conditions of the ejected fluid, the formation number of vortex rings can be different from the value obtained experimentally by Gharib *et al.* (1998). Some of these conditions are: changes in the piston velocity program (Mohseni *et al.* 2001), the cylinder exit velocity profile (Rosenfeld *et al.* 1998) or, more recently, the existence of an imposed bulk counter-flow (Dabiri & Gharib 2004) and a background co-flow (Krueger *et al.* 2006). In particular, Linden & Turner (2001), discussed that the maximum value of L_m/D_0 above which a single ring cannot be formed may be as large as 7.83. By temporally varying the exit cylinder diameter during formation, Dabiri & Gharib (2005) observed that the formation number could be delayed up to 8. Based on the study of a jellyfish swimming kinematics, Dabiri *et al.* (2006) reported that the limiting vortex formation time was delayed to at least 8. Akhmetov (2001) studied the formation of vortex rings in air using a jet generator. The starting jet was produced using compressed air; so there was not a piston nor mechanical devices. He measured the vortex circulation using the hot wire anemometry technique. The Reynolds number was $Re_0 = 3.65 \cdot 10^4$. The non-dimensional jet length was defined as $L* = U_0 T_0 / R_0$; where U_0 is the jet velocity, T_0 is the discharge time and R_0 is the nozzle radius. This jet length is equivalent to the stroke ratio $L* = 2U_p T_0/D_0 = 2L_m/D_0$ for an impulse velocity program. Akhmetov found that the vortex ring circulation increases monotonically with the non dimensional jet length $L*$ at least up to $L* \approx 20$ or $L_m/D_0 \approx 10$. The experimental results from Gharib *et al.* (1998) and

Akhmetov (2001) will be discussed further in chapter 3.

1.2 Motivation and objectives

Vortex rings are fundamentally important in fluid mechanics due to their prevalence in a variety of flows including turbulent flow fields. The vortex rings are present in many engineering applications and natural phenomena. Some examples are starting jets, helicopter rotors, propulsion, volcanic eruptions, animal locomotion etc. A great volume of research has been published since the end of 19^{th}. Recently, vortex rings have been implemented as a method to extinguish fires in oil wells (Akhmetov 2009).

One of the objectives of the present investigation is to verify the formation number under different experimental conditions; particulary we want to verify some of the arguments described above. If there is a limiting process above which a vortex ring is no longer able to accumulate more vorticity in its core, where or when it occurs. Is the formation time $t^* \approx 4$ defined by Gharib an universal time scale for vortex ring formation for any Re number?. In particular, we extend the analysis of the process of vortex formation for Reynolds numbers as low as 150. We found that the schemes of vortex identification previously used for smaller Re are not appropriate. Hence, we propose an alternative method based on the so-called Q criterion (described in section 1.5) to identify vortex structures; also, we measure the vortex ring circulation considering this identification scheme. This method was also used to analyze the formation process of vortex rings for a range of Re in between 150 and 2000. To our knowledge, measurements of the formation process of vortex rings for Re of O(100) do no exist in the literature. We also propose a procedure to improve the location of vortex ring centers by computing the curvature of Lagrangian trajectories in the flow (section 1.6).

It is important to highlight that all of the vortex ring studies have been focused on Newtonian fluids; however, most of the fluids in nature and in many industrial applications have non-Newtonian characteristics. In particular we are interested in the study of vortex ring formation using blood-like liquids. We have mentioned that vortex rings are generated inside the human heart at the left ventricle when blood is discharged during cardiac diastole. It has been demonstrated that the optimal ring formation might be an indicator of cardiac health. We did experiments and obtained vortex ring properties for different shear-thinning liquids at a fixed Re number. We want to know how does the non-Newtonian behavior affect the circulation in vortex rings.

1.3 Vorticity and circulation

The *vorticity* $\boldsymbol{\omega}$ of a flow field $\mathbf{u}$, is defined by

$$\boldsymbol{\omega} = \nabla \times \boldsymbol{u} \tag{1.3}$$

In Cartesian tensor notation $\boldsymbol{\omega}$ is expressed as

$$\omega_{ijk} = \epsilon_{ijk}\frac{\partial u_k}{\partial x_j} = \left(\frac{\partial \omega}{\partial y} - \frac{\partial v}{\partial z}, \frac{\partial u}{\partial z} - \frac{\partial \omega}{\partial x}, \frac{\partial v}{\partial x} - \frac{\partial u}{\partial y}\right) \tag{1.4}$$

The vorticity is a measure of the rate of rotation of a small fluid element about its own axes. The motion of a fluid element with zero vorticity ($\nabla \times \boldsymbol{u} = 0$) is called *irrotational*. Applying the divergence to 1.3, and considering a continuous medium it follows that

$$\nabla \cdot \boldsymbol{\omega} = \nabla \cdot (\nabla \times \boldsymbol{u}) = 0 \tag{1.5}$$

i.e., the vorticity field is *solenoidal*. The *circulation* Γ is another important concept in fluid dynamics and is defined as a linear integral of fluid velocity $\boldsymbol{u}$ along a closed circuit C.

$$\Gamma = \oint_C \boldsymbol{u} \cdot d\boldsymbol{l} \tag{1.6}$$

where $d\boldsymbol{l}$ is a differential longitude on the curve C. Applying the *Stokes theorem*, a linear integral can be transformed into the surface integral:

$$\Gamma = \oint_C \boldsymbol{u} \cdot d\boldsymbol{l} = \int_S (\nabla \times \boldsymbol{u}) \cdot \boldsymbol{n} dS = \int_S \boldsymbol{\omega} \cdot \boldsymbol{n} dS \tag{1.7}$$

where S is a small planar area perpendicular to $\boldsymbol{n}$. The circulation is a scalar quantity and is a measure of the integrated component of vorticity normal to the surface surrounded by C. In a 2D flow the circulation equals to the total vorticity (integrated vorticity) in the field flow.

1.3.1 The vorticity equation

The vorticity equation is obtained from the momentum equation:

$$\frac{D\boldsymbol{u}}{Dt} = \frac{\partial \boldsymbol{u}}{\partial t} + (\boldsymbol{u} \cdot \nabla)\boldsymbol{u} = \frac{-\nabla p}{\rho} + \frac{\nabla \cdot \boldsymbol{\tau}}{\rho} + \boldsymbol{g} \tag{1.8}$$

where ρ is the fluid density, p is the pressure, $\boldsymbol{\tau}$ is the viscous stress tensor and $\boldsymbol{g}$ represents the body forces. Using the vector identity $(\boldsymbol{u} \cdot \nabla)\boldsymbol{u} = \nabla(\frac{1}{2}\boldsymbol{u} \cdot \boldsymbol{u}) - \boldsymbol{u} \times \boldsymbol{\omega}$ the above expression can be rewritten as:

$$\frac{\partial \boldsymbol{u}}{\partial t} + \nabla\left(\frac{\boldsymbol{u}\cdot\boldsymbol{u}}{2}\right) - \boldsymbol{u}\times\boldsymbol{\omega} = \frac{-\nabla p}{\rho} + \frac{\nabla\cdot\boldsymbol{\tau}}{\rho} + \boldsymbol{g}$$

Taking the curl of this equation and considering two vector identities one can show that:

$$\begin{aligned}\frac{D\boldsymbol{\omega}}{Dt} &= -\boldsymbol{\omega}(\nabla\cdot\boldsymbol{u}) + (\boldsymbol{\omega}\cdot\boldsymbol{\nabla})\boldsymbol{u} \\ +\frac{1}{\rho^2}\nabla\rho\times\nabla p - \frac{1}{\rho^2}\nabla\rho\times(\nabla\cdot\boldsymbol{\tau}) + \frac{1}{\rho}\nabla\times(\nabla\cdot\boldsymbol{\tau}) + \nabla\times\boldsymbol{g}&\end{aligned} \tag{1.9}$$

To eliminate ∇p, one can use the momentum equation, to obtain:

$$\begin{aligned}\frac{D\boldsymbol{\omega}}{Dt} &= -\boldsymbol{\omega}(\nabla\cdot\boldsymbol{u}) + (\boldsymbol{\omega}\cdot\boldsymbol{\nabla})\boldsymbol{u} \\ +\frac{1}{\rho}\nabla\rho\times\left(\boldsymbol{g} - \frac{D\boldsymbol{u}}{Dt}\right) + \frac{1}{\rho}\nabla\times(\nabla\cdot\boldsymbol{\tau}) + \nabla\times\boldsymbol{g}&\end{aligned} \tag{1.10}$$

Equations 1.9 and 1.10 are the most general forms of the vorticity equation. Considering a Newtonian fluid and only potential body forces, the vorticity equation reduces to:

$$\frac{D\boldsymbol{\omega}}{Dt} = (\boldsymbol{\omega}\cdot\nabla)\boldsymbol{u} + \nu\nabla^2\boldsymbol{\omega} \tag{1.11}$$

where ν is the kinematic viscosity of the fluid. In expanded form the vorticity equation is expressed as:

$$\frac{\partial \boldsymbol{\omega}}{\partial t} + (\boldsymbol{u}\cdot\nabla)\boldsymbol{\omega} = (\boldsymbol{\omega}\cdot\nabla)\boldsymbol{u} + \nu\nabla^2\boldsymbol{\omega} \tag{1.12}$$

1.4 Mathematical background of vortex rings

1.4.1 Invariants

Consider the cylindrical coordinates (r,ϕ,x); r radial, ϕ azimuthal and x axial (see Fig. 1.3). For a general axisymmetric flow ($\partial/\partial\phi = 0$) with swirl (i.e. flow in the azimuthal direction $u_\phi \neq 0$), we can define the following invariants:

Hydrodynamic Impulse (I): The hydrodynamic impulse is equal to the mechanical impulse required to generate a flow from rest.

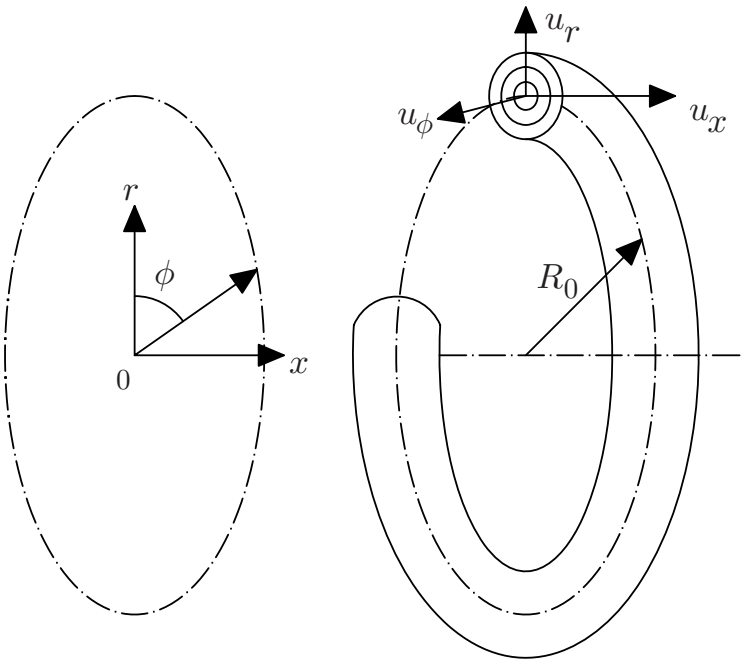

Figure 1.3: The coordinate system for a vortex ring.

$$I = \tfrac{1}{2}\rho \int \boldsymbol{x} \times \boldsymbol{\omega} dV \tag{1.13}$$

where $\boldsymbol{x}$ is a position vector and dV is a differential of volume. In the case of an axisymmetric flow the axial component of the impulse is:

$$I_x = \pi\rho \int_0^\infty \int_{-\infty}^\infty \omega_\phi r^2 dx dr \tag{1.14}$$

where ω_ϕ is the azimuthal component of the vorticity. In the absence of external forces, the impulse is invariant even in the presence of viscosity.

Circulation (Γ): For a closed circuit the circulation is defined in Eq. 1.7. To calculate the vortex ring circulation we first consider a plane of constant ϕ. Then we encircle the region of vorticity of the upper half part of the plane (Fig. 1.3). This is expressed as

$$\Gamma = \int_0^\infty \int_{-\infty}^\infty \omega_\phi dx dr \tag{1.15}$$

If the fluid is inviscid, the vortex circulation is constant; however, if the effect of viscosity is important, the vortex ring circulation will decrease with time.

Kinetic Energy ($\boldsymbol{E}$): the total kinetic energy is defined as

$$E = \rho \int \boldsymbol{u} \cdot (\boldsymbol{x} \times \boldsymbol{\omega}) dV \tag{1.16}$$

for an axisymmetric flow:

$$E = \pi\rho \int_0^\infty \int_{-\infty}^\infty (\psi\omega_\phi + u_\phi^2 r) dx dr \tag{1.17}$$

where $\psi = \psi(r, x)$ is the Stokes stream function. The kinetic energy is only invariant in an ideal fluid where the effect of viscosity can be neglected.

The Integral of the Helicity density ($\boldsymbol{H}$): In inviscid, barotropic flows for which al body forces are conservative, this quantity is conserved and in general is given by

$$H = \int \boldsymbol{u} \cdot \boldsymbol{w} dV \tag{1.18}$$

In the case of an axisymmetric flow:

$$H = -4\pi \int_0^\infty \int_{-\infty}^\infty \omega_\phi u_\phi r dx dr \tag{1.19}$$

Angular momentum ($\boldsymbol{M}$): For an unbounded flow this quantity is defined as:

$$M = -\frac{1}{2}\rho \int r^2 \boldsymbol{\omega} dV \tag{1.20}$$

In the axisymmetric case it can only exists one component of angular impulse

$$M_x = -\pi\rho \int_{-\infty}^\infty \int_0^\infty r^3 \omega_x dr dx = 2\pi\rho \int_{-\infty}^\infty \int_0^\infty r^2 u_\phi dr dx \tag{1.21}$$

If the vortex rings do not have swirl (i.e. $u_\phi = 0$), both $\boldsymbol{H}$ and $\boldsymbol{M}$ are zero.

1.4.2 Formation of vortex ring: Slug model

This model is based on the assumption that the vortex ring is generated by a cylindrical 'slug' of fluid that is ejected from a nozzle using a piston-cylinder arrangement (Didden 1979, Lim & Nickels 1995). The model considers that the boundary layer thickness $\delta \ll D/2$ and the wall-normal velocity component u_r is much smaller than the streamwise component u_x. Under this conditions, we may write the circulation as

$$\frac{d\Gamma_p}{dt} \approx \int_{D/2-\delta}^{D/2} \omega_\phi u_x dr \approx \int_{D/2-\delta}^{D/2} u_x \left(-\frac{du_x}{dr}\right) dr \tag{1.22}$$

considering that the velocity at the edge of the boundary layer is equal to the piston velocity U_p, the total circulation ejected through the cylinder exit is expressed as

$$\Gamma_p \approx \int_0^{T_0} \left[-\frac{u_x^2}{2}\right]_{D/2-\delta}^{D/2} dt = \tfrac{1}{2} U_p^2 T_0 = \tfrac{1}{2} U_p L_m \tag{1.23}$$

where T_0 is the total duration of the piston stroke (total discharge time) and L_m is the total piston displacement. The impulse I_p and the kinetic energy E_p per unity density of the ejected fluid can be obtained:

$$I_p = \tfrac{1}{4}\pi U_p D_0^2 L_m \tag{1.24}$$

$$E_p = \tfrac{1}{8}\pi c U_p^2 D_0^2 L_m \tag{1.25}$$

where c is the fraction of the nominal kinetic energy of the 'plug' of fluid actually injected into the ring (Linden & Turner 2001). Previous investigations have found some differences between the slug model and the actual experimental results. These discrepancies are attributed to different causes (Didden 1979):

- When the piston starts moving, there is an acceleration of flow near the wall leading to increased velocity gradients and, therefore, increased vorticity flux into the ring.

- At larger times the boundary layer grows leading to an increment in the velocity at the center of the cylinder in order to satisfy continuity. Thus, the slug model underestimates the maximum real velocity. This is more critical for low Reynolds numbers.

- The ingestion of secondary vorticity of opposite sign produced at the external wall leads to reduced circulation.

Despite all this limitations, the slug model is often used for comparison with experimental data since it requires the knowledge of easily measurable parameters.

1.4.3 Thin cored vortex rings

The first studies of vortex rings appeared in the 19^{th} century. For a vortex ring with circulation Γ, radius R_0 (i.e. the distance from the vortex center to the symmetry axis), core radius $\epsilon \ll R_0$ and uniform vorticity distribution (see Fig. 1.4), Kelvin (1867) obtained the formula for the vortex translation velocity

$$U = \frac{\Gamma}{4\pi R_0}\left(\log\frac{8R_0}{\epsilon} - \frac{1}{4}\right) \tag{1.26}$$

For the case of a hollow vortex ring (or filled with immobile fluid) Hicks(1885) obtained the equation

$$U = \frac{\Gamma}{4\pi R_0}\left(\log\frac{8R_0}{\epsilon} - \frac{1}{2}\right) \tag{1.27}$$

Based of Lamb's (1932) ideas, Saffman (1992) studied thin vortices and derived relations which allow consideration of viscosity effect, swirling, unsteadiness and compressibility. Consider s and θ, the polar coordinates about an origin in the core distance from the axis of symmetry (Fig. 1.4). Saffman defined the function

$$\Gamma_0(s) = \int_0^s 2\pi\omega_0(s')s'ds' \tag{1.28}$$

so $\Gamma = \Gamma_0(\epsilon)$. The velocity and vorticity in the azimuthal direction could be defined in terms of s so $u_\phi = u_{\phi 0}(s)$ and $\omega_\phi = \omega_0(s)$; where $u_{\phi 0}$ and ω_0 are constants. The expression to obtain the vortex ring translation velocity is defined as:

$$U = \frac{\Gamma}{4\pi R_0}\left(\log\frac{8R_0}{\epsilon} - \frac{1}{2} + 2\frac{\pi^2\epsilon^2\overline{u_\theta^2}}{\Gamma^2} - 4\frac{\pi^2\epsilon^2\overline{u_{\phi 0}^2}}{\Gamma^2}\right) \tag{1.29}$$

where $u_\theta = \Gamma_0(s)/2\pi s$. The lines above the velocity components represent the average over the vortex cross-section. Saffman also derived an estimation for the kinematic energy:

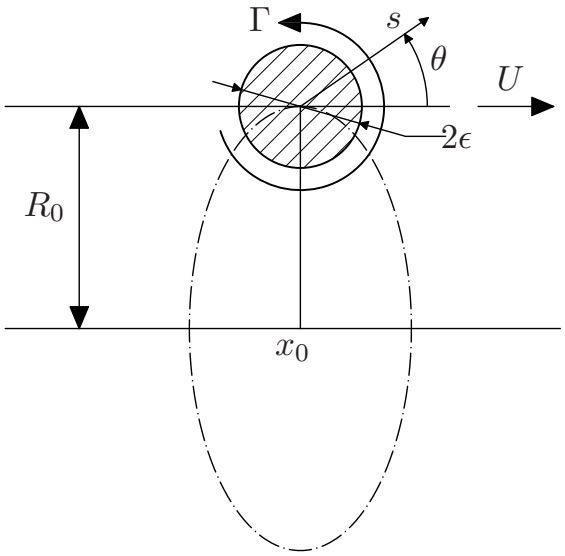

Figure 1.4: The coordinate system for a vortex ring with finite area.

$$E = \frac{1}{2} R_0 \Gamma^2 \left(\log \frac{8R_0}{\epsilon} - 2 + 2\frac{\pi^2 \epsilon^2 \overline{u_\theta^2}}{\Gamma^2} + 2\frac{\pi^2 \epsilon^2 \overline{u_{\phi 0}^2}}{\Gamma^2} \right) \tag{1.30}$$

It is important to note from Eq. 1.29 that the swirl velocity could slow down the vortex velocity; in fact, when u_ϕ is high enough the ring could go backwards. Saffman derived the translation velocity for a viscous vortex ring considering the distribution of circulation corresponding to the Oseen-Lamb vortex filament

$$\Gamma(s,t) = \Gamma(1 - e^{-s^2/4\nu t}) \tag{1.31}$$

the speed for the viscous vortex ring with a thin core is obtained

$$U = \frac{\Gamma}{4\pi R_0} \left[\log \frac{8R_0}{\sqrt{4\nu t}} - 0.688 \right] \tag{1.32}$$

The above equation is valid only in the limit as $t \ll R_0^2/4\nu$, i.e. for small time and as long as the vortex core remains small. Kaplanski & Rudi (1999) derived the translation velocity for a viscous vortex ring using a vorticity distribution $\boldsymbol{\omega} = \boldsymbol{\omega}(r, x, t)$ which is valid for a wider time range. Following

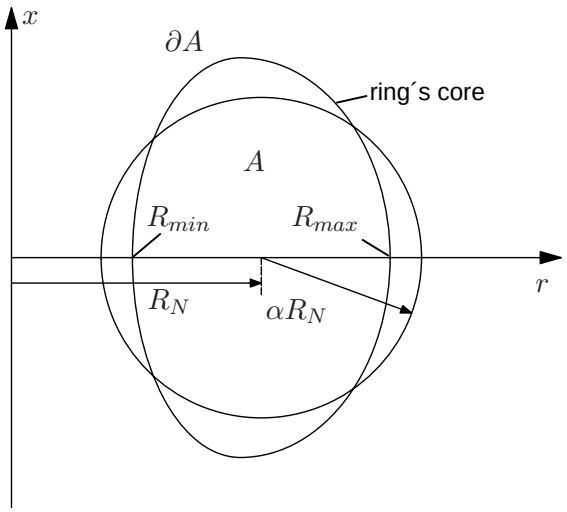

Figure 1.5: The meridional cross-section area of the Fraenkel-Norbury vortices.

the approach by Saffman, Moore (1985) obtained the velocity translation of a uniform vortex ring in a compressed medium

$$U = \frac{\Gamma}{4\pi R_0}\left[\log\frac{8R_0}{\epsilon} - \frac{1}{4} - \frac{5M^2}{12}\right] \tag{1.33}$$

where $M = \Gamma/2\pi\epsilon c_\infty$ is the Mach number and c_∞ is the sound velocity at infinity.

1.4.4 Fraenkel-Norbury vortices

Fraenkel (1970) proved the existence of steady vortex rings with sufficiently small core size, i.e. $\epsilon/R_0 \ll 1$, in an inviscid fluid. Without swirling, Fraenkel derived relations for the shape, the translation velocity and other properties of these vortex rings with the help of expansion in the small parameter ϵ/R_0 in the solution of integral equation on the stream function (Fraenkel 1972):

$$\psi(r,x) = -\frac{1}{2}Wr^2 + \frac{1}{2\pi}\int\int G(r,r',x-x')F(\psi')dr'dx' \tag{1.34}$$

where W is an uniform stream velocity (in the axial direction), which corresponds to the propagation velocity U of the ring when it moves through

fluid at rest at infinity. $F(\psi) = \omega_\phi/r$ is the vorticity distribution and $\psi' \equiv \psi(r', x')$. The kernel G is the stream function at $\boldsymbol{x} = (r, x)$ of a singular vortex circle about axis of symmetry through the point $\boldsymbol{x'} = (r', x')$.

Fraenkel (1972) studied examples of steady vortices with convex cross section and relatively small area, while Norbury (1972) gave examples of steady vortex rings with large cross section close to the so called Hill's (1894) spherical vortex. Finally, Norbury (1973) proposed the existence of a family of steady vortex rings in terms of a non-dimensional mean core radius α defined by the equation:

$$\alpha^2 = \frac{A}{\pi R_N^2} \tag{1.35}$$

where A is the cross-sectional area of the rings's core and $R_N = (R_{\min} + R_{\max})/2$ is a measure of the ring radius (see Fig. 1.5). The values of α are in the range $0 < \alpha \leq \sqrt{2}$, extending from a vortex ring with small cross-section (where $\alpha \to 0$) to the Hill's spherical vortex (for which $\alpha = \sqrt{2}$). The vorticity equation $\boldsymbol{u} \cdot \mathrm{grad}(\omega_\phi/r) = 0$ is satisfied trivially by the particular distribution $\omega_\phi = \Omega_0 r$ (Ω_0=constant) of vorticity. The problem can be stated as (Norbury 1973): find the Stokes stream function $\psi(r, x)$ and boundary ∂A of the cross section area A such that:

$$\left\{ \frac{\partial^2}{\partial r^2} - \frac{1}{r}\frac{\partial}{\partial r} + \frac{\partial^2}{\partial x^2} \right\} \psi(r, x) = \left\{ \begin{matrix} -\Omega_0 r^2 & \text{inside } \partial A \\ 0 & \text{outside } \partial A \end{matrix} \right\} \tag{1.36}$$

These vortices were named as the "Norbury-Fraenkel" family. Introducing the function $F(\psi') = \Omega_0$ in Eq. 1.34 and considering that $\psi(r, x) = k$ on ∂A (k is a positive constant), Norbury obtained:

$$k = -\frac{1}{2} W r^2 + \frac{\Omega_0}{2\pi} \int\int G(r, r', x - x') dr' dx' \text{ for } (r, x) \in \partial A \tag{1.37}$$

The problem is reduced to finding curves ∂A that satisfy Eq. 1.37 for different W,Ω_0 and k. Norbury (1973) resolved the above equation using a numerical scheme. He gave results for the core boundary shape and propagation velocity, as well as other vortex properties like the circulation, impulse and kinetic energy and presented them in tabular form for different α. The shape of the vortex ring cross-section is presented in Fig. 1.6.

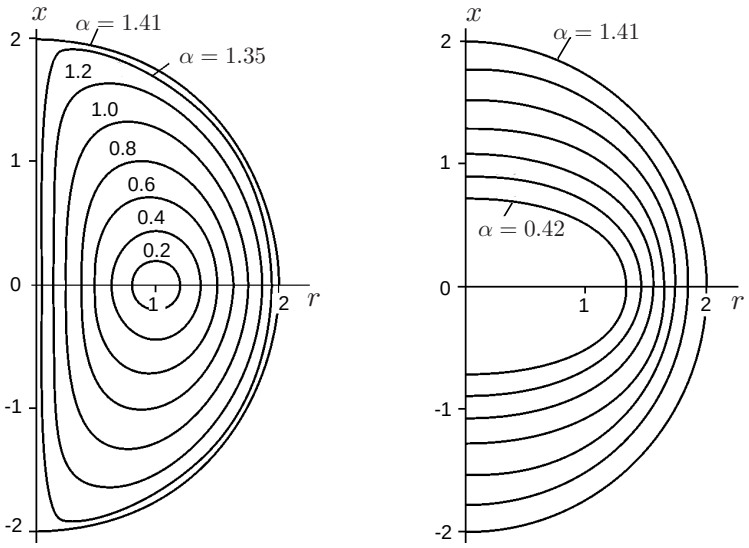

Figure 1.6: Shape and streamlines of Norbury vortices for different α.

.

1.5 Vortex identification

Notwithstanding vortices have been studied for a long time, there is not a consensus of a mathematical definition of a vortex in the fluid mechanics community. Normally a vortex is associated with a region of flow with high vorticity, however, as noted by Haller (2005): "...there is no universal threshold over which vorticity is to be considered high". In parallel shear flows it is possible to find regions with high vorticity but no vortices are present. Definitions requiring pressure minima are incomplete or unsatisfactory while criteria based on closed pathlines or streamlines are ambiguous because the topology of the these lines can change with different frames of reference. Jeong & Hussain (1995) discuss the problems of using these definitions.

In real fluids, the diffusion of vorticity by viscosity impedes the existence of a sharp boundary between rotational and irrotational flow. The interaction of vorticity distribution with strain field, makes the problem of identifying vortices more complicated (Chakraborty *et al.* 2005). Concerning vortex rings, some authors have limited the size of the vortex by choosing an arbitrary minimum vorticity contour value or a percentage of the maximum vorticity at the center of the ring. Such criteria are subjective and

inappropriate when there is not a 'physical' separation between the vortex ring and the trailing jet.

There are some schemes to identify vortices based on local analysis of the velocity gradient tensor $\nabla \boldsymbol{u}$. These vortex identification criteria are Galilean invariant, i.e. remain invariant in different inertial frames of reference. Examples of these techniques are the Q criterion of Hunt *et al.* (1988), the λ_2 criterion of Jeong and Hussain (1995) and the Δ criterion proposed by Chong *et al.* (1990). For two dimensional flows, the Q criterion is known as the *Okubo-Weiss* criterion proposed by Okubo (1970) and Weiss (1991). The Q criterion uses the velocity gradient decomposition

$$\nabla \boldsymbol{u} = \boldsymbol{D} + \boldsymbol{\Omega} \tag{1.38}$$

where $\boldsymbol{D} = \frac{1}{2}((\nabla \boldsymbol{u}) + (\nabla \boldsymbol{u})^t)$ is the symmetric and $\boldsymbol{\Omega} = \frac{1}{2}((\nabla \boldsymbol{u}) - (\nabla \boldsymbol{u})^t)$ the antisymmetric components of $\nabla \boldsymbol{u}$, respectively. The tensor $\boldsymbol{D}$ is usually called the 'rate of deformation tensor' (or rate of strain tensor) while $\boldsymbol{\Omega}$ is also known as the 'vorticity tensor' (or rate of rotation tensor). The second invariant Q, for an incompressible flow ($\nabla \cdot \boldsymbol{u} = 0$) is defined by

$$Q = \frac{1}{2}(|\boldsymbol{\Omega}|^2 - |\boldsymbol{D}|^2) \tag{1.39}$$

where $|\boldsymbol{\Omega}| = tr[\boldsymbol{\Omega}\boldsymbol{\Omega}^t]^{1/2}$ and $|\boldsymbol{D}| = tr[\boldsymbol{D}\boldsymbol{D}^t]^{1/2}$. In regions where $Q > 0$ the local measure of rotation rate is larger than the strain rate, therefore the spatial region belong to a vortex. This function can be evaluated point-by-point and we can classify each point as being inside or outside the vortex ring.

1.6 Center of vortices

We use a method to find topologically relevant points in the flow to locate the vortex ring center. In a two-dimensional flow, special points can be found in the regions where the local velocity becomes zero (Oullette & Gollub 2007). There are two types of special points. When located in a region of the flow where the vorticity dominates, such points are elliptic; in a strain-dominated region, they are hyperbolic (i.e., saddlelike). It has been shown that the elliptical points correspond to the center of the vortices presented in the flow (Chong *et al.* 1990). It is possible to find the elliptic and hyperbolic points by computing the curvature of Lagrangian trajectories, that is, the trajectories of individual moving fluid elements; in this investigation, we use the 2D velocity field obtained by the PIV technique (described in

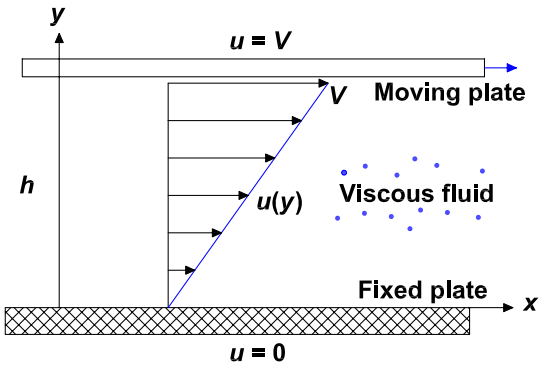

Figure 1.7: Viscous flow between two parallel plates.

chapter 2). Near both hyperbolic and elliptic points, the direction of fluid particle trajectories changes over very short length scales, producing large curvature values. The curvature was obtained following the scheme of Braun *et al.* (2006):

$$k(t) = \frac{|\boldsymbol{u} \times \partial_t \boldsymbol{u} + \boldsymbol{u} \times [\boldsymbol{u} \cdot \nabla \boldsymbol{u}]|}{|\boldsymbol{u}|^3} \tag{1.40}$$

where $\boldsymbol{u}$ is the velocity field and ∂_t is the partial time derivative. Once the points of local maximum curvature are identified, it is possible to classify them as elliptic or hyperbolic using the Q criterion described above. If the special point has a Q value $Q < 0$ the local flow is dominated by strain; if $Q > 0$, where rotation dominates, the point is the center of a vortex ring.

1.7 Viscous fluids

Since part of this investigation is focused in the determination of the effects of non-Newtonian behavior in the vortex ring formation process, it is appropriate to define the fluid properties. In particular, in this section we present some definitions of non-Newtonian rheology.

1.7.1 Newtonian fluids

Consider the fluid between two horizontal plates shown in Fig. 1.7. A flow is induced between the fixed lower plate and the upper plate moving steadily at a velocity V. The distance between plates is h and there is

not slip between the plates and the fluid. If the plates are large enough so $u_y = u_z = 0$, a velocity distribution $u_x(y)$ is found. Consider also that there is not acceleration nor pressure variation in the flow direction. If the fluid between plates is *Newtonian*, the local stress (shear stress) necessary to keep moving the upper plate at constant velocity is proportional to the velocity gradient perpendicular to the plane of shear:

$$\tau_{xy} = \mu \frac{du_x}{dy} = \mu \dot{\gamma} \tag{1.41}$$

where μ is the fluid kinematic viscosity. The velocity gradient du_x/dy is usually known as the *shear strain rate* (or simply shear rate). Isaac Newton first described this phenomenon in his famous *Principia Mathematica* (1687). Equation 1.41 is only valid for simple shear flows (Fig. 1.7). In three dimensions (tensor form), the viscous stress tensor is defined as:

$$\boldsymbol{\tau} = \mu 2\boldsymbol{D} \tag{1.42}$$

where $\boldsymbol{D}$ is the rate of strain tensor defined in section 1.5. Equation 1.42 represents the constitutive equation for Newtonian fluids. Temperature has a strong effect and pressure a moderate effect on viscosity. Gas viscosity increases with temperature, while liquid viscosity decreases with temperature and is roughly exponential $\mu \approx ae^{-bT}$. Viscosity measurements on Newtonian fluids, conducted at constant temperature and pressure, have the following characteristics (Barnes 1989, §15):

- The stress versus shear rate curve is linear and passes through the origin.
- The only stress generated in simple shear flow is the shear stress $\boldsymbol{\tau}$.
- The fluid viscosity does not vary whit shear rate.
- The viscosity is constant with respect of the time of shearing and the stress in a liquid falls to zero immediately the shearing is stopped.
- The viscosities measured in different instruments and different types of deformation are always proportional to one another. For example, the viscosity measured in an uniaxial extensional flow is always three times the value measured in simple shear flow.

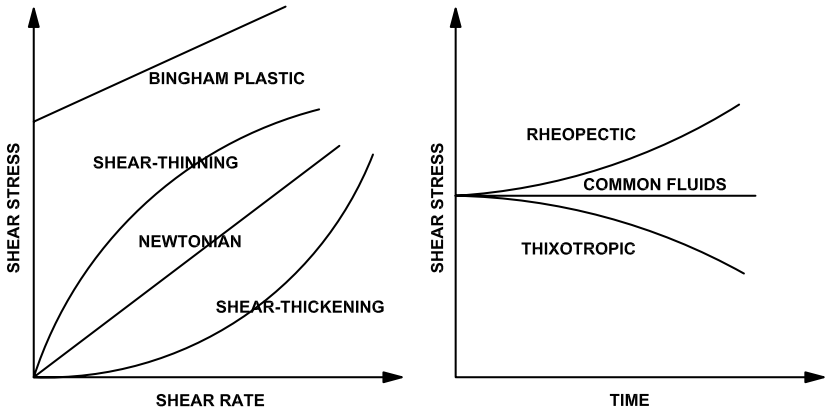

Figure 1.8: Rheological properties for different viscous fluids.

1.7.2 Non-Newtonian fluids

Any fluid showing different behavior than the listed above, is considered non-Newtonian. As soon as the first instruments to measure viscosity appeared and it was possible to observe the influence of the shear rate on the viscosity, many materials presented a different behavior from the Newtonian fluids. In Fig. 1.8 we show the rheological behavior of different viscous materials. The main types of non-Newtonian fluids are:

- **Shear-thinning fluids**. In these materials, the viscosity decreases with increasing the shear rate. These fluids are also known as *pseudo-plastics*. Many materials such as dispersions, emulsions and polymer solutions present this behavior. This effect is explained from the rearrangement of the material internal structure in the fluid; for example, long chains in polymers align in the shear direction reducing viscosity. Some examples are: lava, paints, whipped cream, ketchup and nail polish. The blood is an example of shear thinning fluid presented in nature.

- **Shear-thickening fluids**. These materials, also known as *dilatants* experiment an increment in viscosity with increasing the shear rate. The dilatant effect occurs when closely packed particles are combined with enough liquid to fill the gaps between them. At higher shear stress, the liquid is unable to fill the gaps created between particles, and friction greatly increases, causing an increase in viscosity. The

mixture of cornstarch with water is an example of dilatant fluid.

- **Bingham plastic**. This material behaves as a rigid body at low stresses but flows as a viscous fluid at high stress. The explanation of this behavior is that the liquid contains particles or large molecules which have a kind of interaction, creating a weak solid structure. A certain amount of stress is required to break this structure. Once the structure has been broken, the particles move with structure. A common example is toothpaste.

- **Thixotropic fluids**. These fluids show a time-dependent change in viscosity. The measured shear stress, and hence the viscosity change with time of shearing. Thixotropic fluids display a decrease in viscosity over time at constant shear rate. Some shear-thinning fluids show a thixotropic behavior. Some gels, colloids and clays present are thixotropic fluids.

- **Rheopectic fluids**. This materials present the opposite effect than the previous one. The longer the fluid undergoes a constant shear strain rate, the higher its viscosity. Similarly as the previous case, rheopectic materials are associated with shear-thickening. Rheopectic fluids like some lubricants, thicken or solidify when shaken. Another examples are the gypsum pastes and printer inks.

- **Viscoelastic fluids**. These materials exhibit both viscous and elastic characteristics when deformation. Some characteristics in viscoelastic materials are: (i) if the stress is held constant, the strain increases with time (creep); (ii) if the strain is held constant, the stress decreases with time (relaxation); (iii) if cyclic loading is applied, hysteresis (a phase lag) is observed in the stress-strain curve, leading to a dissipation of mechanical energy. Some examples include: amorphous polymers, semicrystalline polymers, biopolymers and metals at very high temperature.

1.7.3 General viscous fluid

In general, the Newtonian constitutive equation accurate describes the rheological behavior of low molecular weight liquids and some polymers at very slow rates of deformation. Many models that depend on rate of deformation arise from the so called 'general viscous model'. Consider that the total stress $\boldsymbol{\sigma}$ depends only on the rate of strain.

$$\boldsymbol{\sigma} = f(2\boldsymbol{D}) \tag{1.43}$$

expanding in a power series gives:

$$\boldsymbol{\sigma} = f_0\boldsymbol{D}^0 + f_1\boldsymbol{D}^1 + f_2\boldsymbol{D}^2 + f_3\boldsymbol{D}^3 + ... \tag{1.44}$$

For an incompressible fluid $\boldsymbol{D}^0 = \boldsymbol{I}$ and $f_0 = -p$. The Cayley-Hamilton theorem states that any tensor satisfies its own characteristic equation, so it is possible to write:

$$\boldsymbol{\sigma} = -p\boldsymbol{I} + \eta_1 2\boldsymbol{D} + \eta_2(2\boldsymbol{D})^2 \tag{1.45}$$

where $\eta_1(II_{2D}, III_{2D})$ and $\eta_2(II_{2D}, III_{2D})$ are scalar functions of the invariants of $2\boldsymbol{D}$. The Newtonian fluid is a special case with $\eta_1 = \mu$ and $\eta_2 = 0$. The η_2 term gives rise to normal stresses in steady shear flow; however they are not in qualitative agreement with experimental observations so it is usually discarded (Macosko 1994 §83). Much rheological work has been done with simple shear flows where $III_{2D} = 0$ so the last equation is reduced to:

$$\boldsymbol{\sigma} = -p\boldsymbol{I} + \eta(II_{2D})2\boldsymbol{D} \tag{1.46}$$

note that the viscous stress tensor is defined by $\boldsymbol{\tau} = 2\eta(II_{2D})\boldsymbol{D}$. Several models are based on $\eta(II_{2D})$; the most widely used one is the *power law model*:

$$\boldsymbol{\tau} = m|II_{2D}|^{(n-1)/2}(2\boldsymbol{D}) \quad \text{or} \quad \tau_{ij} = m|II_{2D}|^{(n-1)/2}(2D_{ij}) \tag{1.47}$$

This equation is most often applied to steady simple shear flows in which the absolute value of the second invariant becomes $|II_{2D}| = \dot{\gamma}^2$ and $D_{12} = D_{21} = \dot{\gamma}/2$ so

$$\tau_{12} = \tau_{21} = \eta\dot{\gamma} = m\dot{\gamma}^n \qquad \text{and} \qquad \eta = m\dot{\gamma}^{(n-1)} \tag{1.48}$$

where n is known as the power-law index and m is called the 'consistency'. $\eta = \eta(\dot{\gamma})$ is commonly known as the apparent fluid viscosity. It is important to note that Eq. 1.48 is valid only for simple shear flows. For three dimensional flows Eq. 1.47 must be used. If $n = 1$ and $m = \mu$ we recover the Newtonian case.

The power law model is a good approximation for the behavior of many polymeric liquids and dispersions. In particular for shear-thinning fluids, for which $n < 1$, at high shear rate ($\dot{\gamma} > 1$), the power law fits experimental

data well. This model has also been used to model shear thickening fluids, for which $n > 1$. One of the disadvantages of the power law is that it fails to describe the low shear rate region in which η goes to infinity rather than to a constant η_0.

Chapter 2

Experimental setup

In this chapter we describe the experimental setup and the measurement techniques used to obtain the velocity measurements and other properties of vortex rings. We discuss the methodology of data acquisition and report the rheological properties of the different liquids used in the present investigation.

2.1 Description of the experiment

The experimental setup is shown in Fig. 2.1. Experiments were performed in a tank using a piston-cylinder arrangement. Vortex rings were generated by the displacement L of a piston inside the cylinder of inner diameter D_0. The cylinder is submerged in liquid with fixed free surface. The piston is coupled to a driving mechanism which is moved in turn by a DC motor. The DC motor is fed by a power supply, which is controlled by a computer. It is possible to control and fix the piston velocity and displacement. Two dimensional velocities were obtained using the particle image velocimetry technique described in section 2.2. All the experimental system (tank, laser, camera) is mounted on an anti-vibration table which allows flatness and optical alignment (Fig. 2.9).

2.1.1 Piston-cylinder apparatus

In the present investigation, two different tanks were used. The first tank dimensions are: $30 \times 30 \times 70$ cm, it can contain approximately 53 liters of liquid. The cylinder is 40 cm long and is set horizontally at the center of the tank. The inner cylinder diameter is $D_0 = 25.7$ mm with 3 mm of thickness.

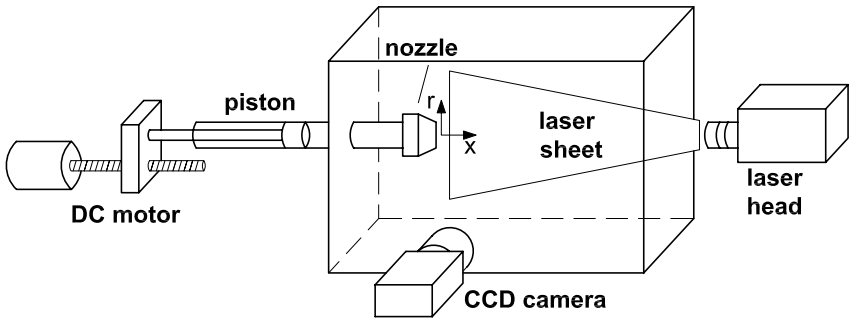

Figure 2.1: Experimental setup.

A sharp-edged cylindrical nozzle was coupled at the end of the cylinder. The tip angle of the nozzle is $\theta_{noz} = 20^\circ$ and the exit diameter is also 25.7 mm (see a nozzle detail in Fig. 2.2b). This angle avoids wall effects at the exit on the formed vortex rings. The nozzle exit plane is placed 25 cm ($\sim 7.8D_0$) from the quadratic wall, 15 cm ($\sim 5.8D_0$) from the side (rectangular) walls and 45 cm ($\sim 17.5D_0$) from the front wall. This tank was used mainly for Newtonian vortex ring experiments.

The second tank dimensions are $20 \times 18 \times 30$ cm. The cylinder is 40 cm long and its inner diameter is $D_0 = 19.4$ mm. In this case the nozzle exit was placed $\sim 3.6D_0$ from the wall, $\sim 6.4D_0$ from the lateral walls and $\sim 11.9D_0$ from the opposite wall. This tank was mainly used for flows with low Re numbers and all the non-Newtonian experiments. For both tanks, the axial axis x is placed to coincide with the center-line of the nozzle and the nozzle exit plane is located in the plane $x = 0$. The piston is made of stainless steel and it is machined with two grooves to fit 'o-rings' which seal the gap between the piston and cylinder.

2.1.2 Driving mechanism

The driving mechanism consists of the following. The piston is coupled with a stem or piston rod, which is pushed through by a screw rod, coupled to a DC motor (see Fig. 2.2 a). We used three screw rods with different travel distance (different thread and speed ratio) in order to generate different ranges in piston velocity. The DC motor is a BALDOR ® DC Gear motor with 1/25 HP and 90 Volts - 0.49 ampere maximum. It produces 5.1 lb.s of torque and output velocity of 344 rpm with gear reducer. By coupling the screw rod directly to the DC motor without gear reducer, the maximum out-

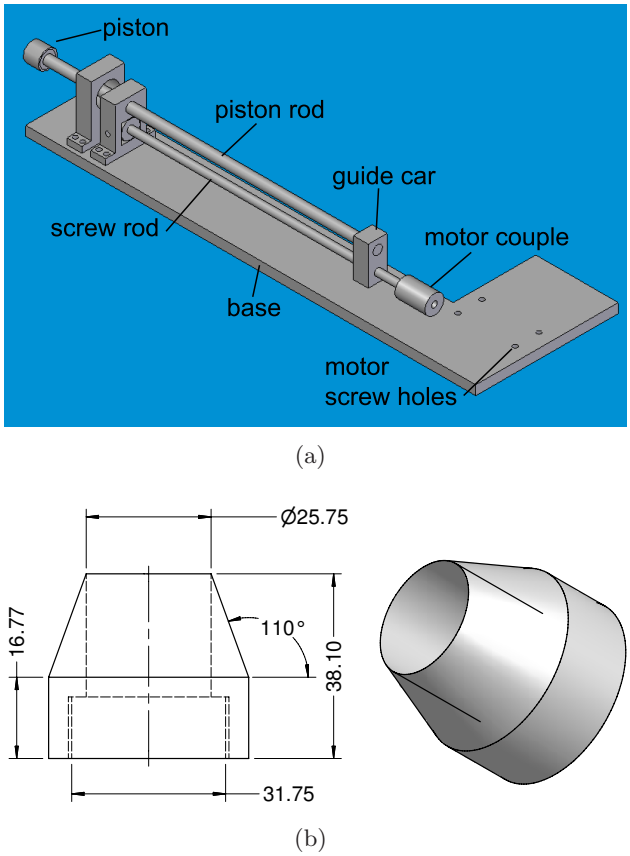

Figure 2.2: (a) Driving mechanism (b) Nozzle detail, dimensions in mm

put velocity is increased up to approximately 1700 rpm. This configuration allows a further increase of the mean piston velocity (see Fig. 2.8).

The DC motor is powered by a power supply which is able to provide a maximum current of 0.51 ampere and voltages in the range of 0-100 volts. The mean piston velocity U_p was proportional to the supplied voltage (Fig. 2.3a). The power supply was controlled by a computer; specifically, we controlled the piston velocity program introducing the voltage and duration of supply. Therefore, it was possible to control and fix the piston velocity and displacement. If the desired displacement was $L_m = jD_0$, where $j = 1, 2...10$, the piston moved a distance x_m so $|x_m - L_m| / L_m \leq 0.02$. Different piston velocities and displacements were implemented. In Fig.2.3(b) we

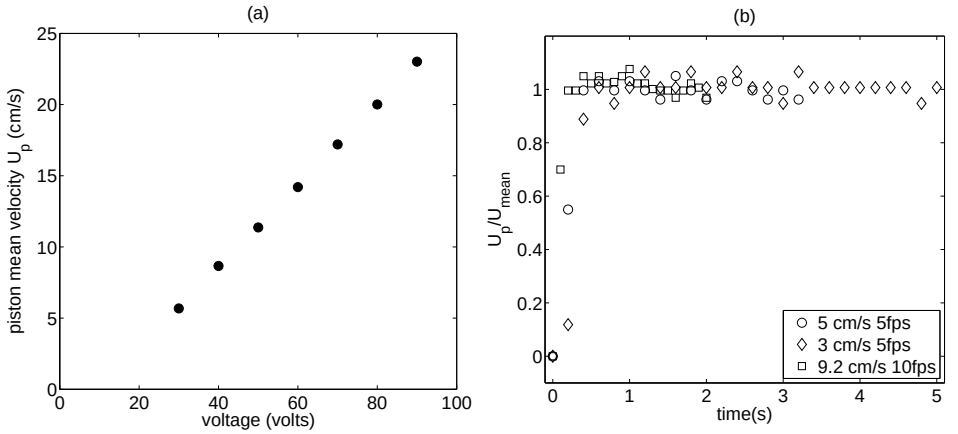

Figure 2.3: (a) Piston velocity as a function of voltage supply. (b) Piston velocity program for different voltages.

present three different piston velocities programs; velocities are normalized with the mean velocity. In these tests, we measured the piston velocity by calculating its displacement between consecutive frames obtained with a digital camera at different frame rates (fps). We can observe that the piston velocity program was *impulsive* and the mean piston velocity was reached at 0.25 s approximately.

2.2 Particle image velocimetry technique

The particle image velocimetry (PIV) is a non-invasive laser optical method for mapping flow fields in gases and liquids. This technique provides instantaneous velocity vector measurements in a cross-section of a flow. Two velocity components are obtained; however, using a stereoscopic scheme it is possible to measure the third component of velocity and obtain the 3D velocity vectors on a plane. PIV has been used broadly in industry and physics of fluids research.

Some applications examples include: general hydrodynamics, rotating machinery, vortex dynamics, wind tunnel measurements, mixing, convection phenomena, etc. PIV measurements are important for environmental research as combustion, wave dynamics, geophysical flows, coastal engineering, river hydrology and others. This technique has also been used in multiphase flows investigations as sprays, bubbly flows, granular flows and free

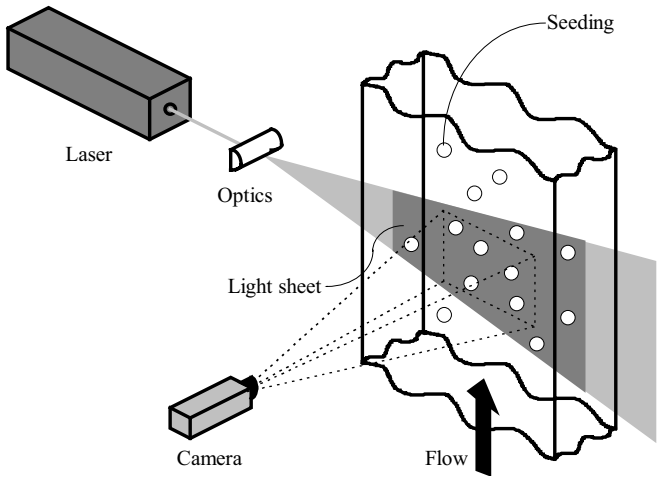

Figure 2.4: PIV principle.

surface measurements. There are also micro-fluidics applications as micro-channels, MEMS and biological flows.

At present it is possible to obtain PIV measurements from high speed flows using 'time resolved' PIV systems which incorporate high speed cameras. These systems now allow a complete study of turbulent flows and mixing phenomena. The new 'volumetric' PIV systems provide truly volumetric velocity data, using to four cameras and a thick light sheet or a scanning thick light sheet. The PIV measurements are also used for experimental verification of CFD models.

2.2.1 Principle

The PIV technique measures the distance traveled by particles suspended in the flow within a known time interval Δt. These particles, also known as 'seeding' or 'tracer' particles, could be made of different materials and have different sizes depending on the nature of the flow to be investigated. In air flows, oil drops in the range 1 μm to 5 μm are typically used. For water applications the tracers could be made of polystyrene, polyamide or hollow glass spheres in the range 5 μm to 100 μm. Seeding particles must be neutrally buoyant and able to follow the flow. In order to detect their movement, a 'flat' area of the flow field is illuminated by a light sheet. In Fig. 2.4 we show a diagram of the PIV principle. A pulsed laser beam

system and optical components generate a sheet-form laser which produces a stroboscopic effect, freezing the motion of the seeding particles. To detect the position of the illuminated particles, a CCD (charge coupled device) camera is placed at right angle to the light-sheet. In order to obtain actual particle displacements, the image scale factor has to be determined. This factor is defined as F=object/image, i.e. the relation between the object (real) space and the image (camera) space.

Two pulses with known time delay are generated from the laser system. These pulses and the camera shots are synchronized so that particle positions from laser pulse 1 are registered on camera frame 1, and particle positions from pulse 2 are registered on frame 2. The camera images are divided into quadratic or rectangular regions called *interrogation areas* and for each of these interrogation areas the image from the first and the second pulse of the light-sheet are 'correlated' to produce an average particle displacement vector (see Fig. 2.5). 10 to 25 particles should be seen in each interrogation area. Performing the same correlation procedure for all interrogation regions, produces a vector map of average particle displacements. Dividing with the time interval Δt between the two images captured, the instantaneous vector velocity field of the flow is generated.

The statistical spatial *cross-correlation* technique is used to estimate the average displacement of tracer particles in each interrogation area. Consider that the function $f(k,l)$ describes the light intensity within an interrogation area of frame 1 recorded in time t and the function $g(k,l)$ describes the light intensity recorded at time $t + \Delta t$. k and l are image co-ordinates in pixels. The discrete cross-correlation function is defined as the expected value:

$$\Phi_{fg}(k,l) = E[f(k,l), g(k,l)] \tag{2.1}$$

$$\Phi_{fg}(k,l) = \sum_{i=-\infty}^{i=\infty} \sum_{j=-\infty}^{j=\infty} f(i,j) \cdot g(i+k, j+l) \tag{2.2}$$

A high cross-correlation value is observed where many particles from frame 1, match up with their corresponding spatially shifted partners from frame 2. Small correlation peaks are observed when individual particles match up with different other particles. When the number of matching particles is large enough, the highest correlation peak is considered to represent the best match between functions $f(k,l)$ and $g(k,l)$. The position of the peak in the correlation plane corresponds directly to the average particle displacement within the interrogation area investigated. An accurate

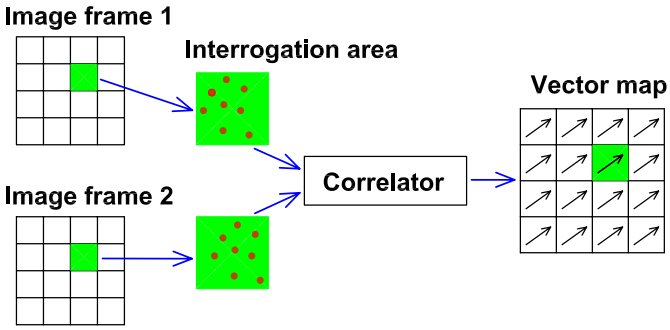

Figure 2.5: Interrogation areas.

measure of the displacement is achieved with sub-pixel interpolation. To efficiently compute the correlation plane, fast Fourier transform processing is often used in PIV.

Seeding particles entering or leaving the interrogation area between the recording of the first and the second frame, contribute to 'random' correlations and a decrease of the signal-to-noise ratio. This phenomenon is often referred to as 'loss-of-pair' or 'signal drop-out'. This is particularly more frequent close to the interrogation area edges. To overcome this problem an 'overlap' on the interrogation area could be implemented. By overlapping interrogation areas, one increases the chance that all particle pairs are completed within at least one interrogation area. Processing with overlap also produces additional vectors through suitable interpolations. The number of vectors that are actually obtained with PIV technique are defined by the relation:

$$\frac{\text{No. pixels in CCD row}}{(1-O_{int})N_{int,h}} \times \frac{\text{No. pixels in CCD column}}{(1-O_{int})N_{int,v}} \tag{2.3}$$

where O_{int} is the percentage of overlap, for example 0.25. $N_{int,h}$ is the horizontal length of the interrogation area in pixels and $N_{int,v}$ is the vertical length. Different validation and filter techniques can be implemented to the raw velocity velocity fields in order to obtain better results. Particulary we implemented the method 'adaptive correlation' which enables a 'window shifting' procedure (Westerwheel, 1997). The principle of this method is an iterative procedure: from an initial guessed offset value, an offset is introduced from the first window (the interrogation area in the image frame from laser pulse one) to the second window. The obtained vector es validated

and is used as a new estimate for the window offset. A new run is made, but this time with a smaller window (interrogation area). A more detailed description of the PIV technique can be found in Willert & Gharib (1991) and Raffel *et al.* (1998).

2.3 Data acquisition

In Fig. 2.6 we show the experimental scheme for data acquisition. Two dimensional velocity fields were obtained using a PIV Dantec Dynamics ® system. The laser sheet is aligned with the central vertical plane of the cylinder. In all our experiments, the axial x-axis coincides with the center-line of the nozzle and the nozzle exit plane is located in the plane $x = 0$. The laser is generated by the Solo III PIV Nd:YAG laser system of New Wave ®. The maximum energy is 50 mJ for a 532 nm laser beam (green light). The maximum repetition rate (measurement frequency) is 15 Hz, the pulse width is 3-5 ns and the beam diameter is 4 mm approximately. Special optical components are mounted to the laser head to generate and control the thickness of the laser-sheet.

A CCD camera is placed at right angle to the light-sheet. The Kodak ® Megaplus ES 1.0 used in the experiment has a resolution of 1008×1016 pixels. The camera contains a special electronic control mode used for fast inter-frame acquisition of two images (also known as double frame mode). Light-sensitive cells are exposed to the scattered light from the first pulse of the laser sheet; this information is then transferred to equal number of storage cells. The CCD chip is then cleared and exposed to scattered light from the second pulse of laser sheet. The storage cells now contain the first frame and the light sensitive cells the second. The minimum time between these two frames is $\Delta t = 1\mu$s. The maximum repetition rate for this camera is 15 Hz for double frame mode (15 image pairs per second).

Camera shots and laser pulses are triggered and synchronized by a control and acquisition unit. Both images frames from the camera are also transferred to this unit. The *Flowmap Processor* also includes input 'buffers' for image storage and a 'correlator' unit used for real-time (on-line) vector processing. The processor is controlled by a computer using the *FlowManager* software. This software is a visual database, which keeps track of the recorded data, the set-ups and the experimental configurations. This software is also used for velocity vector calculations. Post-processing, i.e. vorticity, Q criteria, vortex translation velocity etc, is carried out using the Matlab ® program.

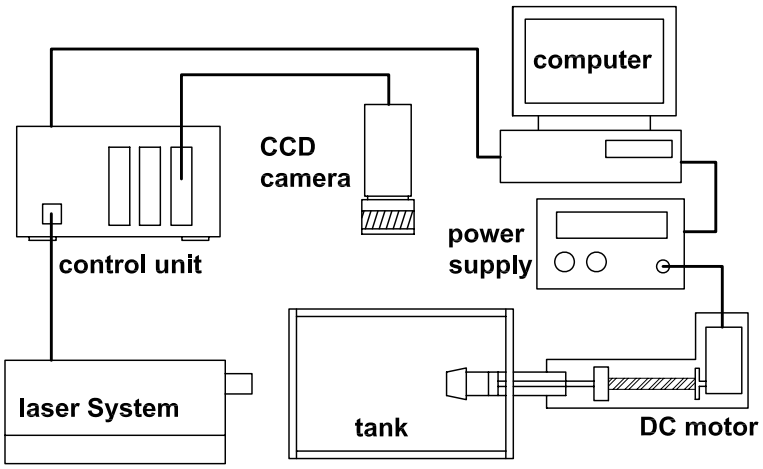

Figure 2.6: Acquisition control system.

In our experiment, a typical measurement area of 141×142 mm^2 was obtained. The velocity field consisted of 62×62 vectors using an interrogation area of 32×32 pixels and and overlap of 50 %. The spatial resolution, without vector interpolation, was 2.24×2.24 mm^2 approximately. Silver-coated glass spheres with an average diameter 10 ± 5 μm were used as particle tracers. The experimental sampling rate (frequency) was 8 to 15 Hz, depending on the velocity of the flow.

The DC motor was powered by a Agilent ® DC power supply which provides 0-100 volts and 0-0.5 amperes. The power supply was controlled by a computer via serial port using the LabView ® software.

2.4 Test liquids

Different liquids were used in the present study. In order to reduce the Reynolds number in Newtonian vortex rings, an aqueous solution of polyethylene glycol (PEG) 6% weight was used. The viscosity of the solution increases with concentration; for this particular case the dynamic viscosity is $\mu = 8$ mPa·s. PEG refers to an oligomer or polymer of ethylene oxide. It is also known as polyethylene oxide (PEO) or polyoxyethylene (POE) depending on its molecular weight. It has many application from industrial manufacturing to medicine. The PEG used in the present experiment has a molecular weight of 20,000 g/gmol and is fabricated by Clariant ®. For

Newtonian and non-Newtonian experiments we also used different concentrations of Glycerol (glycerine or glycerin). Pure glycerol has 1.26 g/cm^3 of density and 1.5 Pa·s of viscosity at 20 °C. To measure the Newtonian viscosity we used the Brookfield ® DV-III viscometer.

In the present work, we studied the effect of shear-thinning liquids on vortex ring formation. We used different aqueous solutions of xanthan gum. This high molecular weight extracellular microbial polysaccharide derives its name from the strain of bacteria using during the fermentation process, *Xanthomonas campestris*. It is produced by fermentation of glucose or sucrose and is used as food additive and rheology modifier. A small amount of gum increases water's viscosity by a large factor (100) at low shear rate. The viscosity of xanthan gum solutions increases with concentration and decreases with with higher shear rates (shear-thinning behavior). The addition of xantham gum to glycerol solutions and also diluted potassium thiocyanate solutions, has been used to produce transparent blood-like fluids (Benard *et al.* 2007). For the experiments we used a KELTROL ® xanthan gum which is used for food and personal care applications distributed by CP-kelco ® company. It is important to note that all the liquids used in the experiments do not have elastic properties or they are too small. For shear-thinning liquids we can define the Reynolds number in terms of the *power law* model parameters:

$$Re_0 = \frac{2^{1-n}\rho U_p^{2-n} D_0^n}{m} \tag{2.4}$$

where n is the power law index and m is the 'consistency'. Note that for Newtonian experiments $n = 1$ and $m = \mu$ is the liquid dynamic viscosity. In table 2.1 we present physical properties of the different solutions used in the present thesis as well as the experimental configuration: cylinder diameter D_0 piston velocity U_p. PEG-06 refers to an aqueous solution 6% weight of polyethylene glycol. Gly-65 refers to a mixture of 35 % water - 65% glycerol in weight. Xan-450 means 450 ppm (parts per million) of xanthan gum in water. G55-X200 is an aqueous solution of glycerol 55 % weight and 200 ppm. Note that the Reynolds number for all xanthan solutions (one case of Xan-450) is approximately 260. This allows us to study the effect of non-Newtonian behavior using different xanthan concentration (different n for example) for the same flow condition (Re number). We are also able to compare the shear-thinning behavior with the Newtonian liquid Gly-65 which has the same Re.

In Fig. 2.7 we present the viscosity as a function of the shear rate $\dot{\gamma}$ for different xanthan solutions. The rheological tests consist in producing

Liquid	Density [kg/m^3]	Consistency m [mPa.s^n]	Power index n	Diameter D_0 [mm]	Vel. piston U_p [cm/s]	Re_0
water	1000	$\mu = 1$	1	25.7	1.3	330
water	”	”	”	”	4.8	1230
water	”	”	”	19.4	10.5	2100
PEG-06	1000	$\mu = 8$	1	25.7	2.85	93
PEG-06	”	”	”	25.7	4.8	150
Gly-65	1151	$\mu = 13.59$	1	19.4	16	263
Xan-450	1000	23.5	0.6088	19.4	7.5	138
Xan-450	1000	”	”	”	12	265
Xan-450	1000	”	”	”	22	616
Xan-600	1000	41.5	0.5431	19.4	15.7	261.8
Xan-900	1000	88.9	0.4781	19.4	23	262
G55-X200	1125	27.06	0.814	19.4	18.7	263

Table 2.1: Physical properties of the test liquids and experimental configurations.

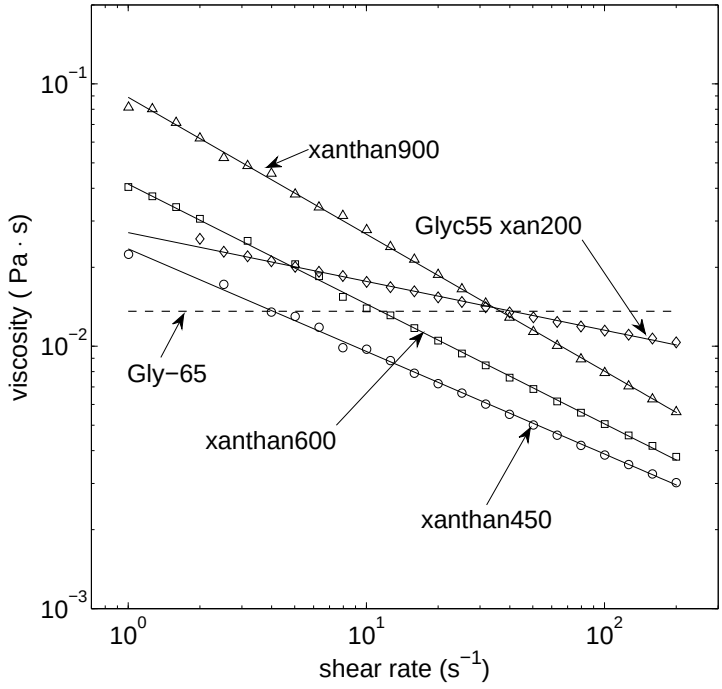

Figure 2.7: Viscosity as function of shear rate for different xanthan solutions.

a simple shear flow between two solid surfaces; one surface rotates as the other is maintained fixed. Viscosity measurements were obtained using a Rheometer AR 1000-N from T.A. Instruments ®. The rheometer measures viscosity in imposed shear stress mode, i.e. a torque is imposed to the rotating geometry and the fluid response is next measured with the corresponding shear strain. We use a steel cone and plate geometry with 60 mm diameter, 2° angle and gap equal to 65 μm. All measurements were performed at a controlled temperature of 23 °C. Liquid viscosity was obtained for shear strain rates in between $1 \leq \dot{\gamma} \leq 200$ s^{-1}. Different levels of shear stress were applied step by step by a decreasing way which allowed a better determination of liquid viscosity for low shear rates. It can be observed from Fig. 2.7 the non-Newtonian behavior of the xanthan solutions; even a small amount of xanthan (200 ppm) makes a glycerol solution a shear-thinning fluid. The plotted lines correspond to the power law model $\eta = m\dot{\gamma}^{n-1}$; where m and n are shown in table 2.1 for each liquid. We can observe that this model fits well experimental data for the measured shear rate range.

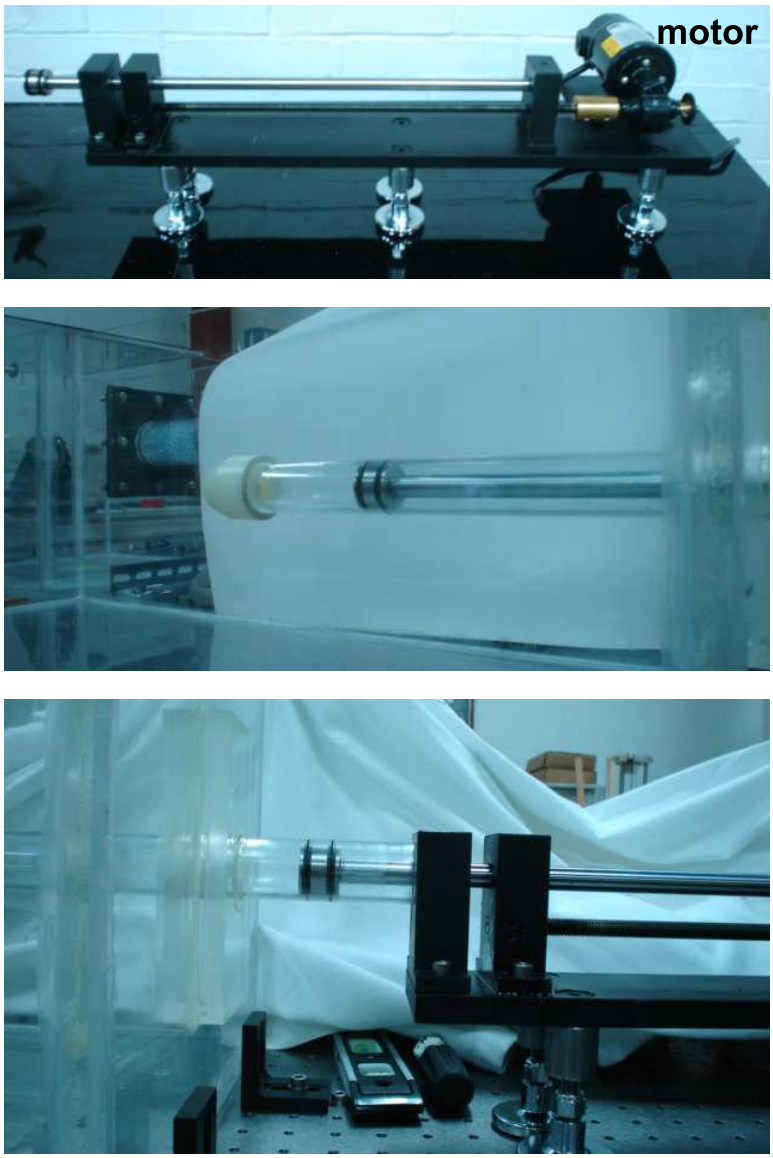

Figure 2.8: Piston-cylinder apparatus and driving mechanism.

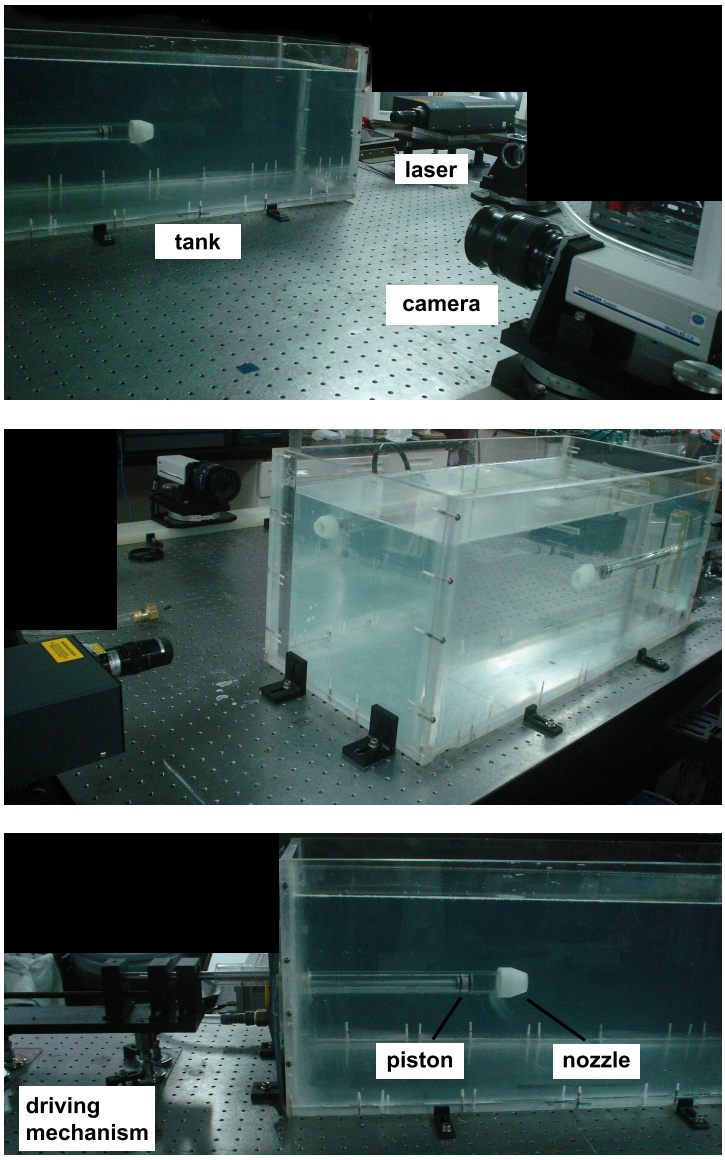

Figure 2.9: Experimental setup, tank 1.

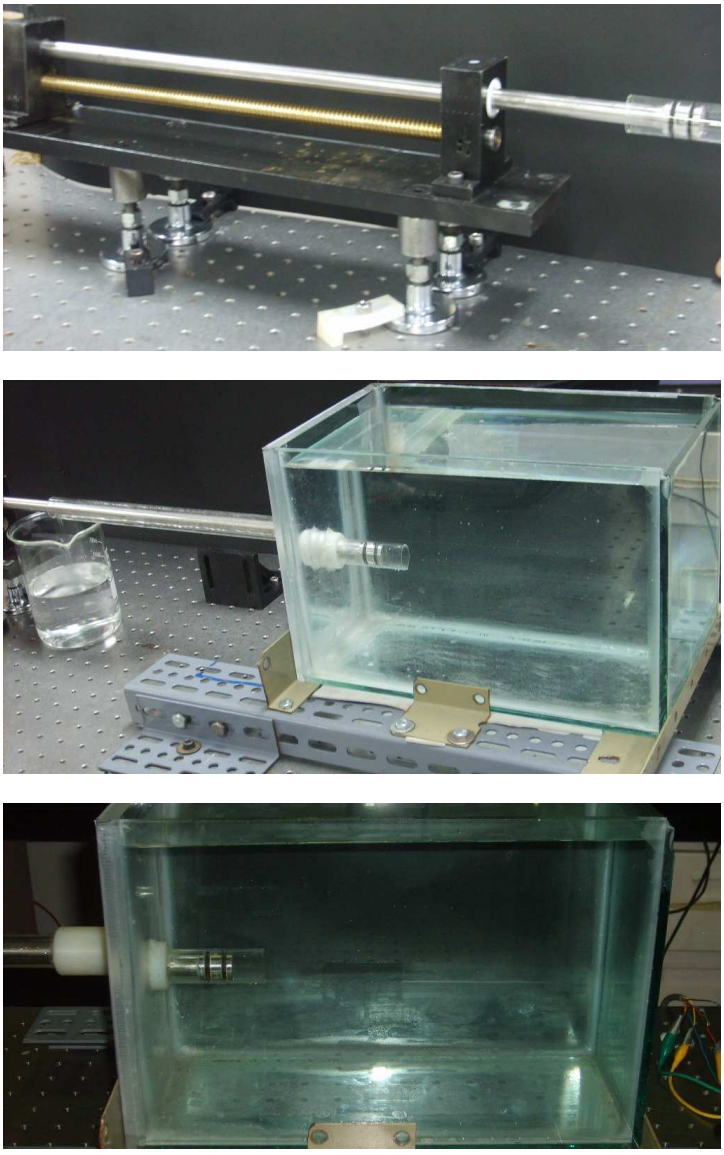

Figure 2.10: Experimental setup, tank 2.

Chapter 3

Newtonian vortices

In this chapter we present experimental results of vortex rings generated in Newtonian liquids at different Reynolds numbers. We first show some image maps to explain the characteristics of this type of flow structure. We present some vortex properties such as trajectories, diameters, velocity profiles propagation velocities. Then, we explain the method to determine the vortex ring circulation and compare with other methods described in the literature. We measure the vortex ring circulation at different distances from the nozzle and with different stroke ratios. We also compare the vortex ring circulation at different Reynolds numbers. Finally, we compare our data to those obtained by some experimental, analytical and numerical previous studies to validate our experimental results.

3.1 Image maps

Figure 3.1 shows the velocity, vorticity and the Q criterion fields (top, middle and bottom rows, respectively) of two flow cases. The first one (Fig. 3.1 a, b, c) corresponds to the production of a single and isolated vortex ring. This configuration occurs for a relatively small stroke ratio; in this case $L_m/D_0 = 3$. The second case (Fig. 3.1 d, e, f) correspond to a flow for which a leading vortex ring followed by a trailing jet was observed. This regime results for larger L_m/D_0 (in this case $L_m/D_0 = 10$). Both vortices are located at a position of $x = 4D_0$. For the case $L_m/D_0 = 3$, $Re_v = 1100$ and the vortex-jet case $Re_v = 1400$. In both cases $Re_0 = 1200$. Different experimental condition (exit diameters, exit plane geometries and non impulsive piston velocities) carried out by Gharib *et al.* (1998), showed that the transition between the two regimes occurs when $L_m/D_0 \approx 4$.

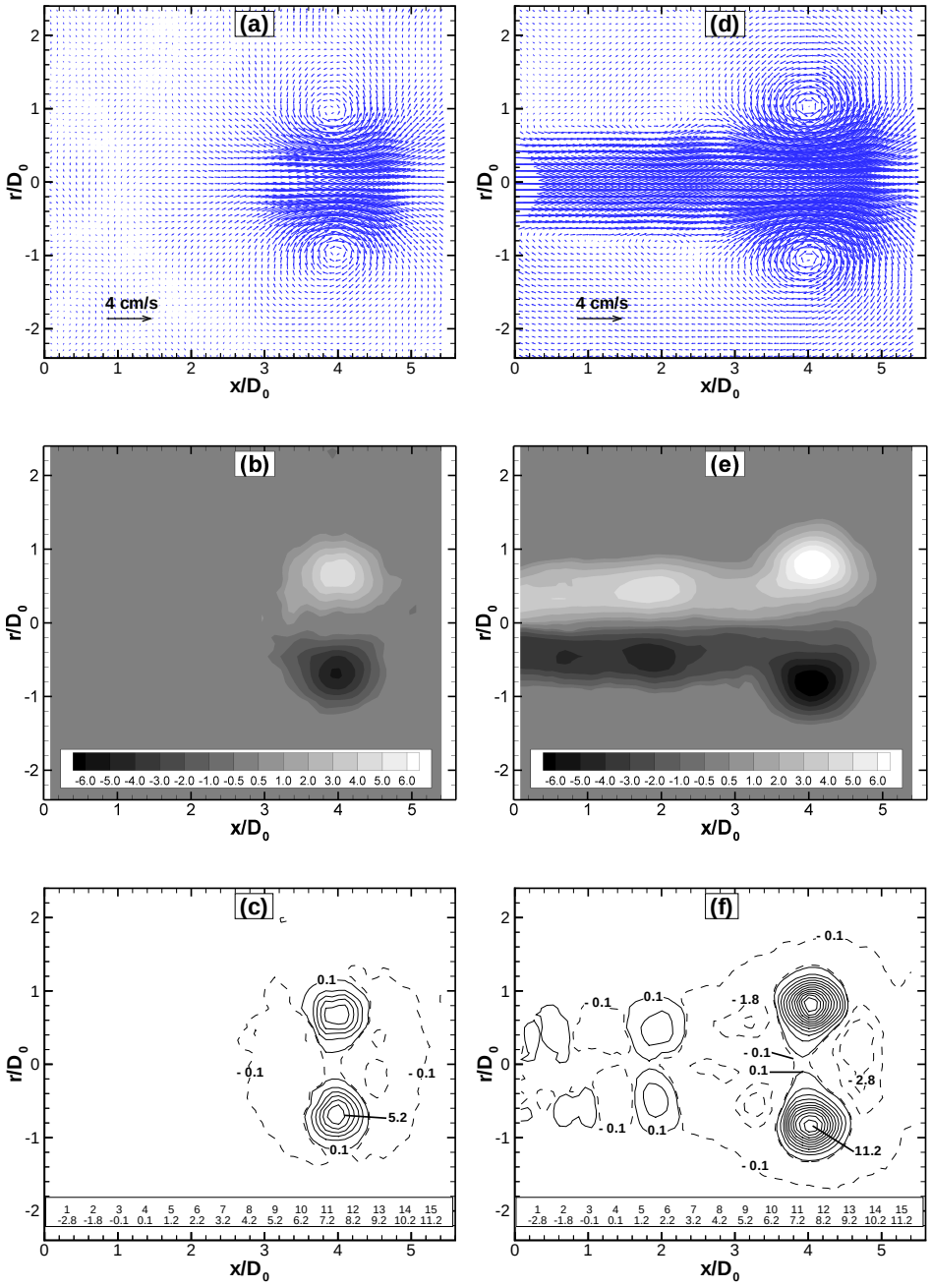

Figure 3.1: Velocity, vorticity and Q criterion fields (top, middle and bottom rows respectively). (a),(b),(c) $L_m/D_0 = 3$; (d),(f),(g) $L_m/D_0 = 10$. Vortex position at $x \approx 4$ $Re_0 = 1200$, vorticity values in s^{-1} and Q values in s^{-2}.

The vorticity fields of figure 3.1(b) show that most of the vorticity in the flow is concentrated in the vortex ring area. This means that the vorticity generated in the boundary layer inside the cylinder was introduced into the vortex ring. On the other hand, the vorticity field for the case $L_m/D_0 = 10$ shows a trailing shear layer connected with the leading vortex ring. It is important to note that a process of separation between the vortex ring and trailing jet can occur at different distances depending on the maximum stroke ratio (Rosenfeld *et al.* 1998). However, as Dabiri (2009) pointed out, the physical separation is not to be confused with the vortex ring "pinch-off" which is the process whereby a forming vortex ring is no longer able to entrain additional vorticity. The separation may occur later or not at all. In our experiments the latter case occurs for low Reynolds numbers. Most authors have limited the size of the vortex ring by choosing an arbitrary minimum vorticity contour value or a percentage of the maximum vorticity at the vortex core. Such criteria become subjective when a physical separation of the vortex ring and the trailing jet is not evidently observable.

Figures 3.1(c) and 3.1(f) show the Q fields for the previous cases. For the single vortex ring case we observe that the region of high rotation rate ($Q > 0$) coincides with the core of the vortex ring. The plot shows that this area is smaller than the corresponding vorticity field. The Q criterion map for the case $L_m/D_0 = 10$ shows a remarkable separation between the vortex ring and the trailing jet. In fact, it is possible to locate secondary vortices behind the leading one. We can also observe strain-dominant regions of the flow (negative Q values) which are located behind and in front of the leading vortex ring. Based on these observations, we will consider the area of the vortex ring to be that for which $Q > 0.01s^{-2}$ for all cases.

Figure 3.2 shows the location of points of maximum curvature (circles), and maximum (or minimum) vorticity (squares) for (a),(b) $Re_0 = 150$ and (c),(d) $Re_0 = 1200$. For both cases the stroke ratio is $L_m/D_0 = 4$ and the position of the vortex center (considering maximum curvature) is $x \approx 8D_0$. Contours of constant curvature (top) and constant vorticity (bottom) are shown in solid black lines. The minimum and maximum contour values are 150 m^{-1} and 3000 m^{-1} (vortex center) respectively. The minimum vorticity value is 0.5 s^{-1} for both cases and the maximum absolute vorticity value is 1.8 s^{-1} for $Re_0 = 150$ and 5 s^{-1} for $Re_0 = 1200$. We observe that vortex rings tend to broaden as Re decreases. To calculate vorticity and curvature scalar maps (and also peak values) we first constructed a subgrid of $dx/3$ and $dy/3$ (~ 0.75 mm) nodes, then we compute a interpolation of velocity vectors to fit the subgrid using triangle-based linear interpolation. If x is the

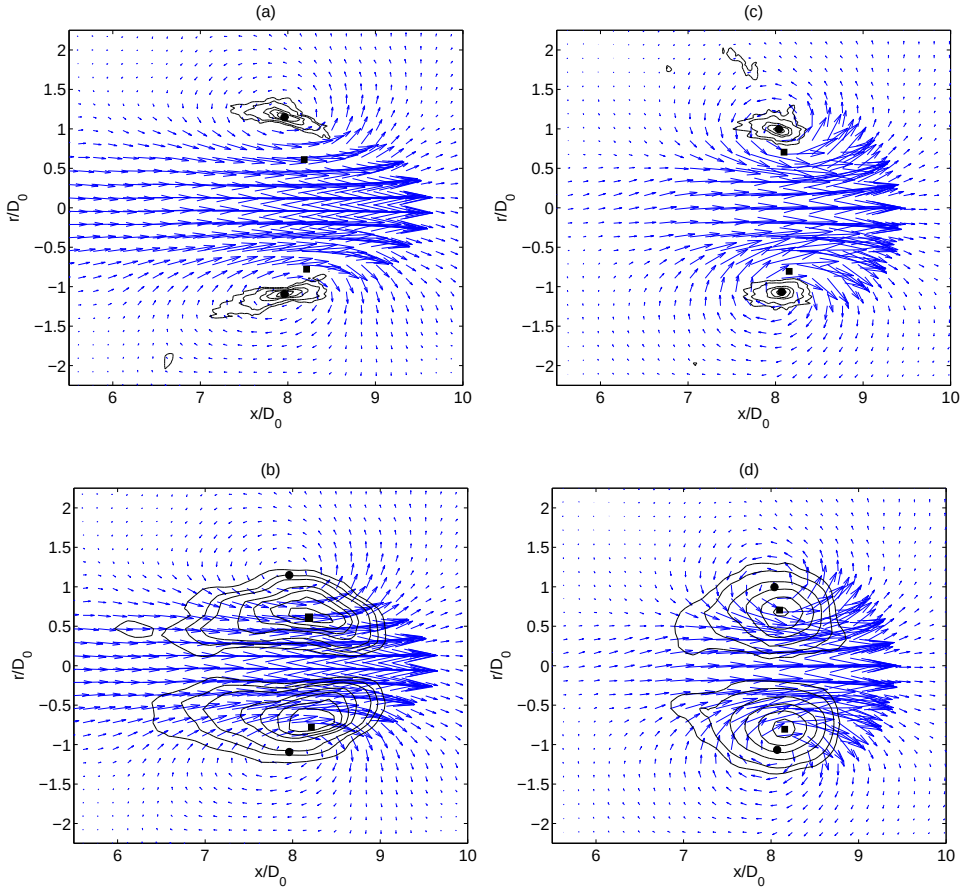

Figure 3.2: Comparison between points of maximum curvature (black circles) and maximum (or minimum) vorticity (black squares). Curvature (top) and vorticity (bottom) contours in solid lines. $L_m/D_0 = 4$ and $x \approx 8D_0$. (a),(b) $Re_0 = 150$ and (c)(d) $Re_0 = 1200$.

distance desired to locate the vortex ring (say $x = 8D_0$) we found a maximum error of $|x - x_k|/x \leq 3\%$ (where x_k is the vortex position measured with peak curvature) but typically less than 1%. Vectors from Fig. 3.2 are resampled for clarity. It is important to note that in most of our experiments, the maximum vorticity coincides with the maximum Q value, i.e. the region of the flow with high rotation rate. However, the point of maximum vorticity does not necessarily coincide with the point of maximum curvature. In general, the point of maximum vorticity tends to move towards the

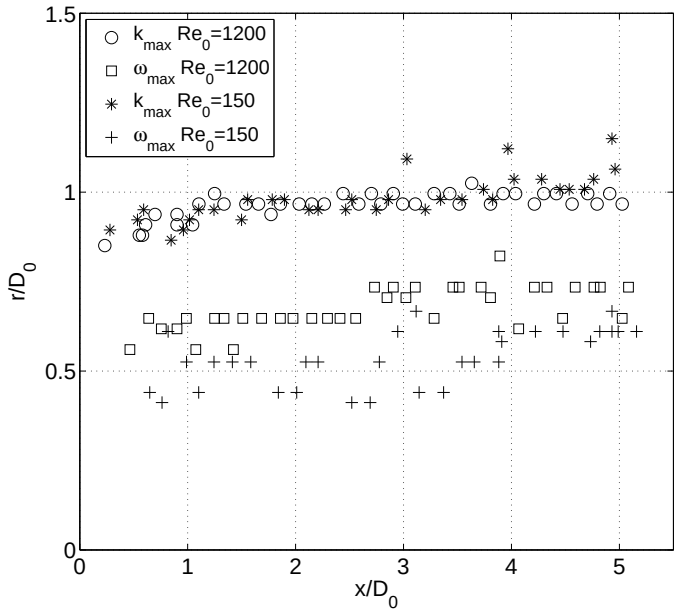

Figure 3.3: Trajectory of vortex ring center considering maximum curvature and maximum vorticity for $L_m/D_0 = 4$.

axis of symmetry; for lower Reynolds numbers (Fig. 3.2a) this difference is more noticeable. We observe in fact that the maximum point of curvature better locates the geometric centers of the vortex rings. Some previous publications (Michalke & Timme 1967) indicate that it is possible to have vortical structures with the extremum value of vorticity outside the rotation axis. The so-called "hollow vortices" are characterized by a slowly rotating center (weak vorticity), surrounding by a high speed circumferential jet (strong vorticity). These vortices have been observed in nature, specifically in geophysical flows like the Antarctic Stratospheric vortex (ozone hole) and the Great Red Spot(GRS) on Jupiter (Shetty *et al.* 2007).

3.2 Vortex properties

Figure 3.3 shows the vortex ring trajectory considering the points of maximum curvature and maximum vorticity for stroke ratio $L_m/D_0 = 4$ and two different Reynolds numbers. In this graph, the position of the vortex ring center on the upper half plane ($r > 0$) is plotted. The points of maximum

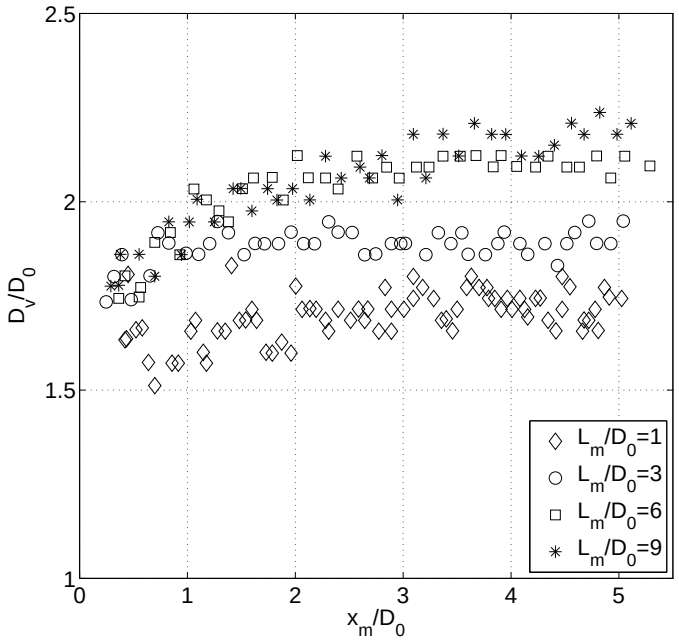

Figure 3.4: Diameter of vortex ring for different stroke ratios. $Re_0 = 1200$.

curvature (k_{max}) are located at a distance $r/D_0 \approx 1$ for both Reynolds number and the points of maximum vorticity are close to $r/D_0 = 0.5$. We can also observe that the vortex ring center uncertainty is larger for the computation of the points of maximum vorticity. For a given L_m/D_0 Weigand & Gharib (1997) found that the trajectories of the vortex rings centers are spatially independent of the Reynolds number, in agreement with our results presented in Fig. 3.3. For all the results presented in this paper, the vortex ring position is obtained from the point of maximum curvature.

Figure 3.4 shows the evolution of the non-dimensional vortex ring diameter D_v/D_0 for different stroke ratios, locating the center from the point of maximum curvature. The Reynolds number is $Re_0 = 1200$. Here x_m is the mean x-position of the centers, i.e. the upper and lower section of the vortex ring. The results indicate that the vortex ring diameter initially increases and then remains constant with a value close to $2D_0$. We can also observe that the vortex ring diameter increases with stroke ratio; however, the experimental data suggest that there is a limit in the vortex ring size for large L_m/D_0. This dependence of ring diameter on stroke ratio has been reported by Didden (1979). It is important to note that the vortex rings diameters

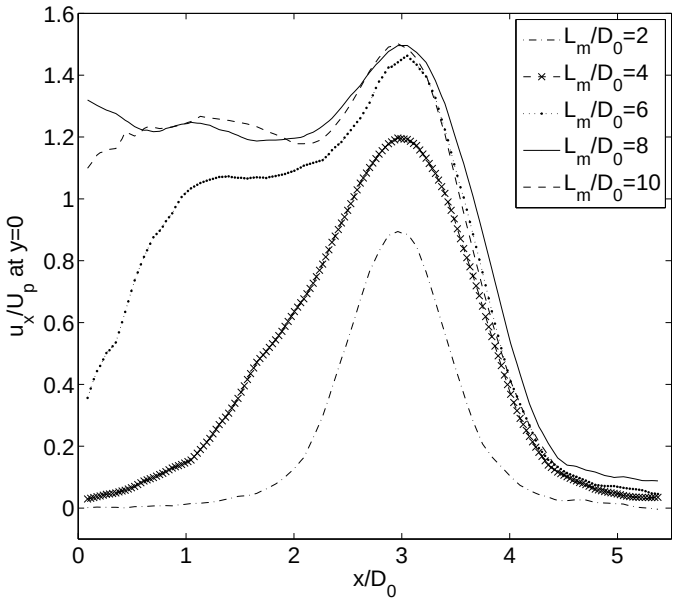

Figure 3.5: Horizontal velocity profile at $r = 0$ for different stroke ratios. Vortex ring centers at $x = 3D_0$. $Re_0 = 1200$.

presented in Fig. 3.4 could be slightly different from those reported in previous works; for example, Didden (1979) presented $D/D_0 = 1.1 - 1.4$ for rings with $L_m/D_0 = 2$. This difference results from the way through which the vortex ring center is located; in our case, the maximum curvature points. If we consider the maximum vorticity points as vortex centers (Fig. 3.3), the diameters for $Re_0 = 1200$ and $L_m/D_0 = 4$ would be $D_v \approx 1.4D_0$ instead of $D_v \approx 2D_0$. Didden (1979) measured vortex diameter using dye visualization images (movie films) and reported a sudden decrease (not observed in the present study) of the ring diameter after the end of each stroke.

The horizontal velocity profiles (u_x) at $r = 0$ (center line) are presented in Fig. 3.5 for different stroke ratios. For all cases the piston velocity is $U_p =$ 4.8cm/s and the vortex ring center is located at $x = 3D_0$. The Reynolds number is $Re_0 = 1200$. The plot indicates that the u-velocity is maximum at the x-location of the vortex ring center and that the velocity profile is symmetric when a single vortex ring is generated. In our experiments, the trailing jet appears when $L_m/D_0 \geq 4.5$ which is consistent with Gharib's experiments. Although the mean piston velocity is the same for all runs, the value of maximum velocity varies with L_m/D_0. When the piston is moving,

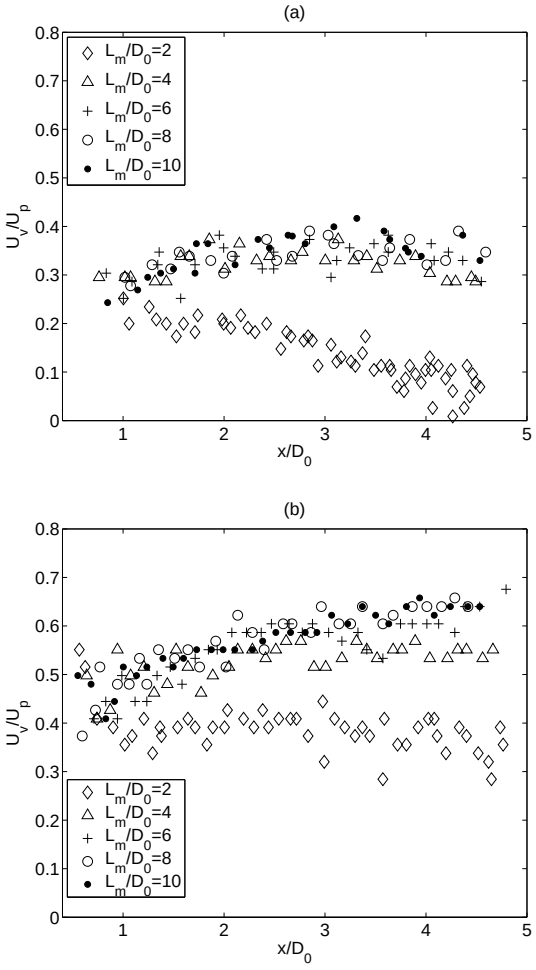

Figure 3.6: Propagation velocity of vortex rings for different stroke ratios. (a) $Re_0 = 150$ and (b) $Re_0 = 1200$.

there is an acceleration of u component at the center line because of the initial growth of boundary layer on the cylinder wall; therefore, for large stroke ratios $u_x/U_p > 1$ close to the nozzle.

Figure 3.6 shows the non-dimensional propagation velocity U_v of vortex rings for different L_m/D_0 for two Re numbers (a) $Re_0 = 150$ (b) $Re_0 = 1200$. The vortex ring velocity is obtained by a numerical differentiation of the vortex ring position based on the location of maximum curvature. For small

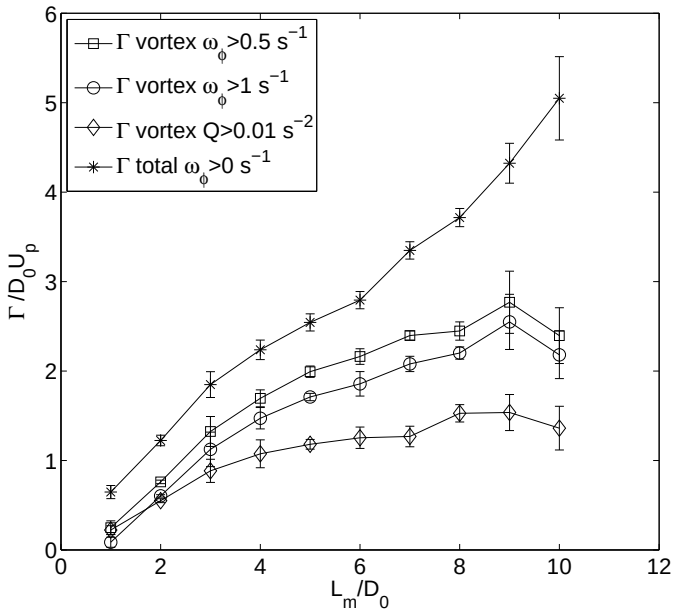

Figure 3.7: Non-dimensional vortex ring circulation as a function of the stroke ratio for $Re_0 = 1200$. $x = 8D_0$

stroke ratios ($L_m/D_0 = 2$) the decay of the propagation velocity is important. Didden (1979) and Weigand & Gharib (1997) indicated that vortex rings velocity decays with time. When $Re_0 = 1200$ and the stroke ratio is relatively large $L_m/D_0 \geq 6$, the vortex ring velocity initially is approximately $0.5U_p$ and then it increases slightly as the vortex ring moves away from the nozzle; however, a vortex ring velocity decay is expected for larger distances from the nozzle. The velocity for $L_m/D_0 = 4$ remains constant close to $0.55U_p$. In their analytical model Mohseni & Gharib (1998) predicted a propagation velocity $U_v = 0.5U_p$, which is close to this particular stroke ratio. The vortex ring velocity when $Re_0 = 150$ is considerable lower than the previous case. The maximum velocities are in a range $0.3 \leq U_v/U_p \leq 0.4$.

3.3 Vortex Circulation

Figure 3.7 shows the total non-dimensional circulation in the visible domain ($\omega_\phi > 0$) and the non-dimensional vortex ring circulation as a function of the stroke ratio L_m/D_0 for $Re_0 = 1200$. The vortex rings are located

at a position $x = 8D_0$. At this distance it is possible to observe a clear separation (minimum vorticity contour value) between the vortex rings and their trailing jet. The points plotted correspond to the average of 5 different runs of the piston. The error bars represent the standard deviation of data. In order to compare our calculation method with previous works, we present the vortex ring circulation in two forms. The first one is based on the Q criterion explained in section 1.5. The circulation is obtained from Eq. 1.7

$$\Gamma = \int_{A_Q} \omega_\phi dA \tag{3.1}$$

where ω_ϕ is the azimuthal vorticity defined as

$$\omega_\phi = \frac{\partial u_r}{\partial x} - \frac{\partial u_x}{\partial r}$$

and A_Q is the region of flow where $Q \geq 0.01 s^{-2}$. The second form of vortex ring calculation is based on the method used by Gharib *et al.* (1998). From the vorticity contours (Fig. 3.1b,e), they obtained the vortex ring circulation by integrating the vorticity contained within a given contour lever for either positive or negative senses. This contour level was determined to be at $1 s^{-1}$. In the presence of a trailing jet, the vortex ring circulation was measured when a clear separation between vorticity contours from the leading vortex ring and the trailing jet exited. Therefore the vortex ring circulation was measured at larger vortex positions from the nozzle: $x \gtrsim 9D_0$. For our experiments ($Re_0 = 1200$) we could observe this separation at $x \approx 8D_0$.

In figure 3.7 we observe that when using the Q criterion the values of vortex ring circulation are lower than those obtained by Gharib's method. This difference is mainly due to the smaller vortex ring area obtained when using Q criterion, see Fig 3.1c,f. The difference becomes smaller as L_m/D_0 decreases; this means that for these cases (when a trailing jet is not present) most of the non-zero vorticity could be associated with the vortex ring. On the contrary, as the stroke ratio increases some of the vorticity created in the flow, although high, based on the Q definition, cannot be associated with "rotation" of fluid particles. Thus, the resulting vortex ring area is reduced. Despite the above arguments, we observe that the trend of the curves is similar. This means that most of the bulk of vorticity is concentrated inside the core of the vortex ring. The large uncertainty for $L_m/D_0 \geq 9$ might be explained by the shedding of excess vorticity from the leading vortex ring (Gharib *et al.* 1998); hence, high irregularity in the vorticity contours is observed. It is important to note that for shorter distances from the

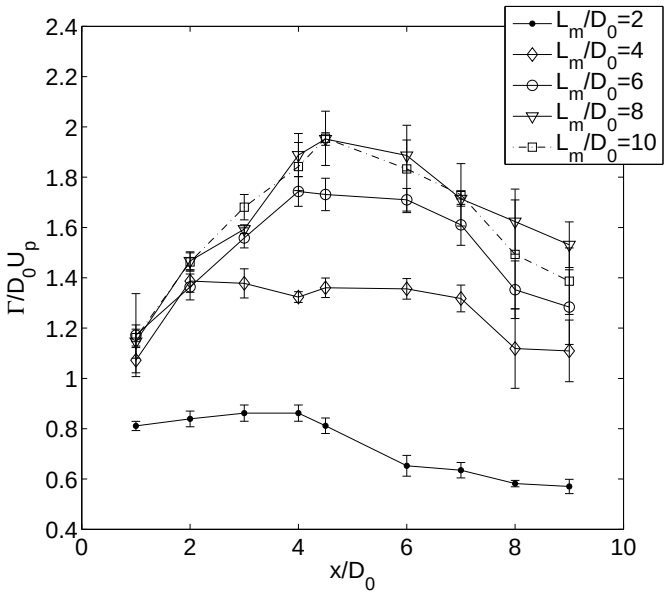

Figure 3.8: Non-dimensional vortex ring circulation at different distances from the nozzle. $Re_0 = 1200$.

nozzle exit, it is difficult (if not impossible) to observe vorticity contour separation between the leading vortex ring and the trailing jet. The same problem has been reported in numerical simulations (Rosenfeld *et al.* 1998). When Reynolds number is small enough this separation may not appear (Dabiri 2009). Moreover, the time or distance at which this "physical" separation occurs (for identical initial conditions) could slightly change with the lowest contour level chosen. Although the Q criterion seems to be a very broad definition of a vortex (i.e. it does not consider pressure minima), the method allows a less subjective vortex ring identification even in the formation stages.

Figure 3.8 shows the non-dimensional vortex ring circulation as function of the distance x/D_0, for different stroke ratios L_m/D_0, for $Re_0 = 1200$. It can be observed that the vortex ring circulation grows as the vortex moves away from the nozzle until the vortex reaches a distance between $4 \leq x/D_0 \leq 6$; after that, the vortex ring circulation, for this particular Reynolds number, decreases slightly. We can also observe that the larger the stroke ratio, the larger is the circulation value. However, the experimental

data suggests that there is a stroke ratio limit ($L_m/D_0 = 8$) above which the dimensionless circulation of vortex ring cannot increase.

Figure 3.9(a) shows the vortex ring circulation as a function of the stroke ratio L_m/D_0. The curves correspond to different vortex ring positions. For clarity we present only some of the total distances obtained. We can observe that the maximum vortex ring circulation for each stroke ratio depends on the distance at which the measurement is done; this has been reported by Rosenfeld *et al.* (1998). For example, close to the nozzle ($x = 3D_0$) the circulation for large stroke ratios ($L_m \geq 5$) has not reached its maximum value. This indicates that the vortex is still feeding of vorticity from the shear layer behind it, i.e. the vortex has not completed its formation. The maximum circulation values are reached at a distance within a range of $4.5D_0 \leq x \leq 7D_0$. Beyond this distance the vortex ring begins to dissipate vorticity; therefore, its circulation decreases (see vortex circulation for $x = 9D_0$). We can also observe from Fig. 3.9(a) that for relatively farther distances from the nozzle ($x \geq 4.5$) the maximum vortex ring circulation is attained when $L_m/D_0 \approx 8$. For this Reynolds number, a physical separation between vortex ring and trailing jet (minimum vorticity contour level is ± 1) is clearly seen at $x \approx 8D_0$.

Figure 3.9(b) shows the same plot for $Re_0 = 150$. The reduction of vortex ring circulation as the vortex moves away from the nozzle is remarkable. The graph indicates that the maximum values of circulation are obtained when the vortex ring is located within the range of $3D_0 \leq x \leq 5D_0$. For low stroke ratios this distance is even closer to the nozzle exit. This suggests that for low Reynolds numbers, the vortex ring formation is completed at closer distances from the nozzle. We can also observe from the data presented in Fig. 3.9(b) that the maximum vortex circulation is obtained when $L_m/D_0 \approx 5$. However, as the vortex ring separates from the nozzle ($x \geq 7D_0$) the maximum circulation is found when $L_m/D_0 \approx 8$. For this Re number we did not observe a physical separation between vortex ring and trailing jet.

If we consider the maximum circulation value for each stroke ratio regardless of the distance at which this value is reached, we obtain the plot shown in Fig. 3.10. In this graph we present four different Reynolds numbers and the experimental results from Gharib *et al.* (1998) and Akhmetov (2001). For the lower Reynolds number, $Re_0 = 150$ we observe that the maximum circulation values are reached when the stroke ratio $L_m/D_0 \approx 4$, for $Re_0 = 263$ $L_m/D_0 \approx 6$, for $Re_0 = 1200$ $L_m/D_0 \approx 8$ and for $Re_0 = 2037$ the vortex circulation grows monotically at least to $L_m/D_0 \approx 10$. We also observe that the vortex circulation is larger as Re decreases. This is more evident for $Re_0 = 150$. It is interesting to note that for $Re_0 = 150$ and

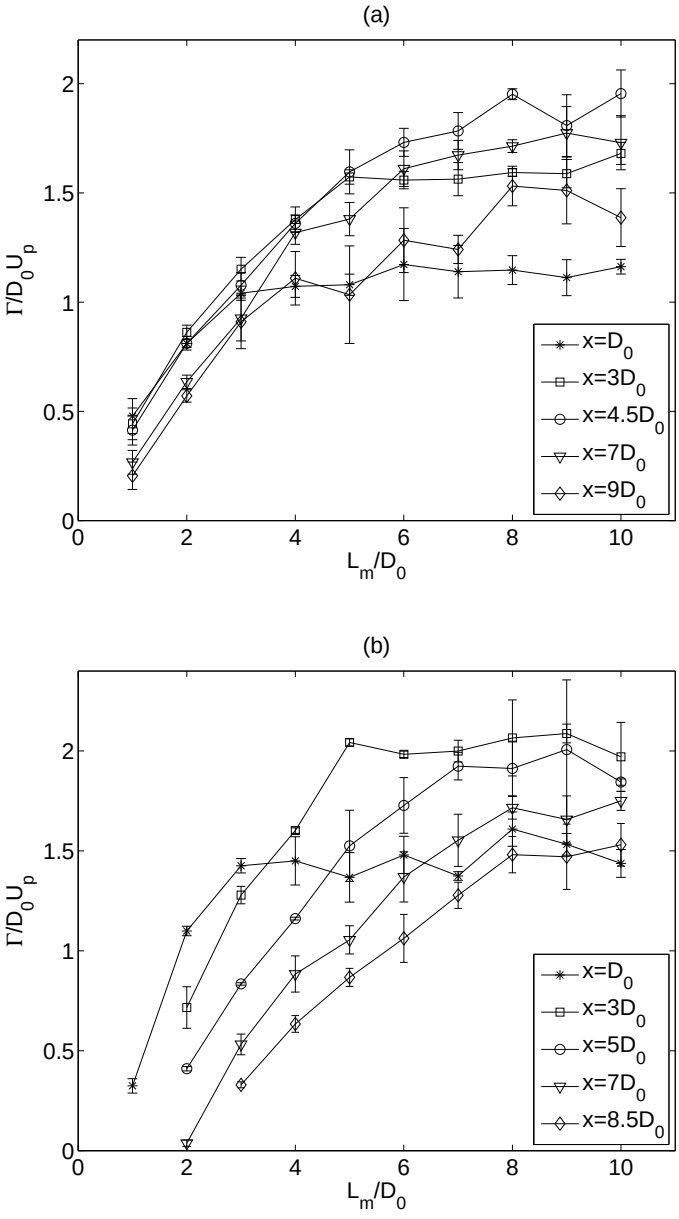

Figure 3.9: Non-dimensional vortex ring circulation as a function of L_m/D_0 for (a) $Re_0 = 1200$ and (b) $Re_0 = 150$.

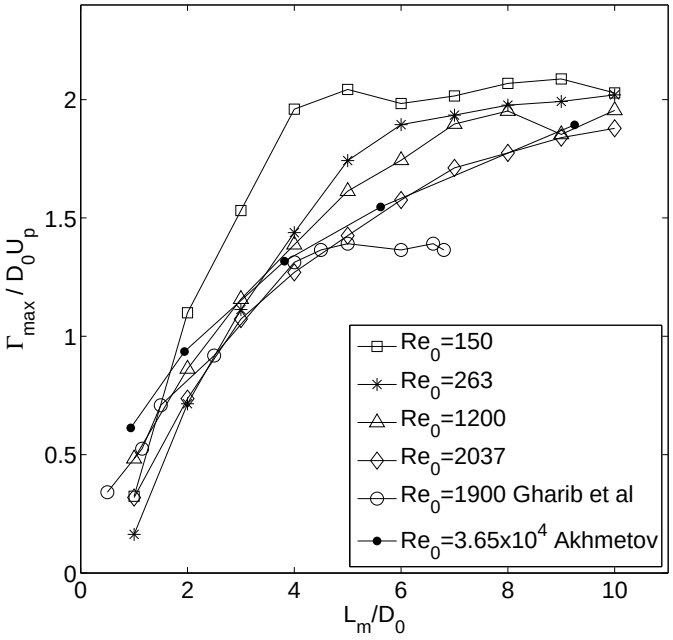

Figure 3.10: Maximum vortex ring circulation for each L_m/D_0.

$Re_0 = 1200$, the piston mean velocity and velocity program is the exactly the same. The maximum non-dimensional circulation value (for the Re_0 studied) is approximately $\Gamma/D_0U_p \approx 2$. This suggests that at this value, the vortex ring has reached a saturation condition beyond which it is not possible to attain more vorticity. The vortex circulation values for $Re_0 = 2037$ are similar to the results from Gharib *et al.* (1998) for $L_m/D_0 < 5$; however, our experimental results indicate that the vortex circulation keeps on increasing for $L_m/D_0 > 5$. This result is consistent with the experimental results from Akhmetov (2001) despite the difference between the Reynolds number.

Gharib *et al.* obtained the velocity and vorticity fields using the PIV technique. They did not specify the exact distance where the vortex ring circulation was measured; however, they stated that for the cases where a trailing jet appeared, "the vortex ring circulation was measured when a clear separation between vorticity contours of the vortex from those of the trailing region existed"; thus, the circulation was determined at a distance far enough away from the nozzle. Nevertheless, at larger distances, the vortex ring has lost part of its circulation because viscous dissipation. This could explain

the differences between the circulation values for larger L_m/D_0. Akhmetov (2001) generated vortex rings in air. He defined the non-dimensional jet length as $L* = U_0T_0/R_0$; where U_0 was the jet velocity, T_0 the discharge time and R_0 the nozzle radius. The jet length is equivalent to the stroke ratio $2L_m/D_0 = L* = 2U_pT_0/D_0$. Akhmetov determined the vortex circulation by integrating the velocity distribution

$$\Gamma = \oint_{ABCDA} \boldsymbol{u}(x,r) \cdot \mathrm{d}\boldsymbol{l} \tag{3.2}$$

along the closed rectangle $ABCDA$ which encloses the upper section of the vortex ring and whose side AB lies on the axis of symmetry. Assuming that the vortex ring propagation velocity u_0 remains constant as it moves through a velocity probe, Akhmetov (2001) determined the vortex ring circulation by the expression

$$\Gamma = u_0 \int_0^{t_A} u(t)dt \tag{3.3}$$

where $t_A \to \infty$. The velocity distribution as a function of time $u(t)$ was measured using the hot wire anemometry technique. The probe was placed far from the discharge nozzle on the axial axis.

3.4 Discussion

Some authors have suggested that changing the conditions of the ejected fluid, the formation number of vortex rings can be different from the value obtained experimentally by Gharib *et al.* (1998). We would like to compare our experimental results to those obtained by some analytical studies.

Mohseni & Gharib (1998) and Linden & Turner (2001) proposed models based on matching the properties of the ejected fluid to the corresponding properties of the "Fraenkel-Norbury" vortex ring family described in section 1.4.4. The effect of viscosity is considered negligible. The properties of the ejected fluid plug are based on the slug flow approximation (see section 1.4.2). The circulation Γ_p, the impulse I_p and the kinetic energy E_p of the plug fluid are defined as

$$\Gamma_p = \tfrac{1}{2}U_pL_m \tag{3.4}$$

$$I_p = \tfrac{1}{4}\pi U_pD_0^2L_m \tag{3.5}$$

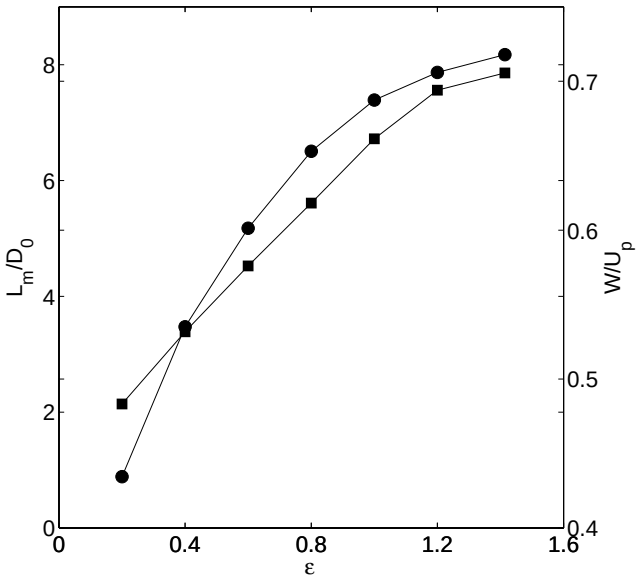

Figure 3.11: Critical stroke ratio (squares) and non-dimensional propagation velocity (circles) against non-dimensional mean core radius. Taken from Linden & Turner (2001).

$$E_p = \tfrac{1}{8}\pi c U_p^2 D_0^2 L_m \tag{3.6}$$

The mean core radius defined by Norbury is expressed as:

$$\alpha^2 = \frac{A}{\pi R_N^2} \tag{3.7}$$

Equating the above equations to the corresponding scaled relations in Norbury's (1973) analysis, and considering circulation, impulse and energy conserved, Mohseni & Gharib found the following equation

$$\frac{L_m}{D_0} = \sqrt{\frac{\pi}{2}}\frac{I_R^{1/2}\Gamma_R^{3/2}}{E_R} \tag{3.8}$$

Similarly, Linden & Turner found that

$$\frac{W}{U_p} = \frac{W_R I_R}{2E_R} \tag{3.9}$$

where $W = U_v$ is the propagation velocity of the ring. The values Γ_R, E_R, I_R, and W_R are available in tabulated form for different mean core radius α in Norbury's paper. Figure 3.11 shows the ratio between the velocity propagation and the ejection velocity as a function of α. The values are in the range $0.4 < W/U_p < 0.7$ which compare very well with our measurements for $Re_0 = 1200$ ($0.3 < U_v/U_p < 0.65$) showed in figure 3.6b. Figure 3.11 also shows the stroke ratio L_m/D_0 as a function of α. The maximum value of L_m/D_0 above which a single ring cannot be formed is $L_m/D_0 = 7.83$. This limit corresponds to Hill's spherical vortex. This value is close to our critical stroke ratio for $Re_0 = 1200$. This fact suggests that the vortex rings we are forming are "thicker" that the ones produced in Gharib's experiments. To verify the above result, we measured the size of vortex rings considering the non-dimensional radius R_Q based on the definition of α (Eq. 3.7):

$$R_Q^2 = \frac{A_Q}{\pi L_Q^2} \tag{3.10}$$

where L_Q is the distance between the maximum Q value (maximum vorticity) and the axis of symmetry ($r = 0$). As mentioned before, we consider the vortex ring area as A_Q: the region of flow where $Q \geq 0.01$, which is also the region within which we calculated the vortex ring circulation. Figure 3.12 shows the non-dimensional radius R_Q as a function of L_m/D_0 for two Reynolds numbers: $Re_0 = 1200$ and $Re_0 = 150$ (shown in Fig. 3.10). For $Re_0 = 1200$ we obtain $0.64 \leq R_Q \leq 0.85$. These values are higher than those predicted by Mohseni & Gharib (1998) for the cylinder-piston mechanism: $0.45 \lesssim \alpha \lesssim 0.6$ and their critical values of stroke ratios $3.0 \lesssim L_m/D_0 \lesssim 4.5$. In fact, we consider that our calculation of A_Q may be underestimated because regions with relatively small rotation rate are excluded. (see Fig.3.1 e and f). A bigger size allows vortices to attain more vorticity. The proximity of a trailing jet ($L_m/D_0 > 4$) can increase the vortex ring size (Fig. 3.4) and therefore, increase its circulation beyond the formation number $t^* = L/D_0 = 4$ obtained by Gharib *et al.* (1998). We think that when the vortex ring has 'separated' from the trailing jet, it has lost part of its circulation by viscous dissipation (Fig. 3.8).

For $Re_0 = 150$, we observe from Fig. 3.12 that the range of non-dimensional radius is $0.85 \leq R_Q \leq 1.23$ which are larger values than those for $Re_0 = 1200$. When the Reynolds number is small, the axial velocity profile $u_x(r)$ inside the tube becomes more parabolic. We will show in chapter 4 that, for a Newtonian fluid and laminar flow, the axial velocity at the tube center is $u_x = 2U_p$. As Re decreases the boundary layer δ increases

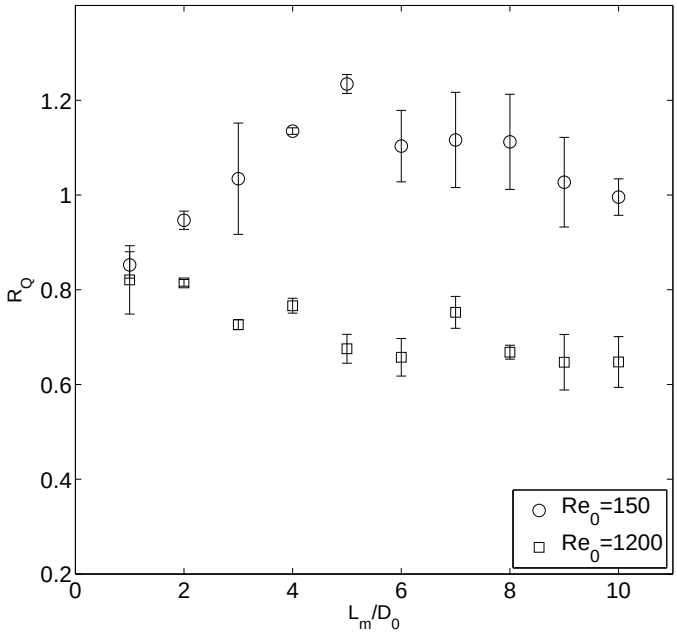

Figure 3.12: Non-dimensional radius (Eq.3.10) for $Re_0 = 150$ and $Re_0 = 1200$.

and this might produce thicker vortices at the nozzle exit capable to attain more vorticity; therefore, the saturation of circulation is achieved at a lower stroke ratio. This is demonstrated for $Re_0 = 150$ for which the critical value (maximum circulation) is $L_m/D_0 \approx 4$ (Fig. 3.10). For a parabolic input velocity profile Linden & Turner (2001) stated that corrections had to be made to the slug assumption. This correction consists in a change of the constants of the slug flow equations (3.4-3.6). Using the same matching procedure, Linden & Turner found that the maximum plug length is reduced by a factor of 0.43, i.e. the $(L_m/D_0)_{max}$ corresponding to the Hill's vortex would be 3.39. This result is consistent with the reduction of critical value of L_m/D_0 (formation number) for the case $Re_0 = 150$ presented in figure 3.10.

Gharib *et al.* (1998) proposed an analytical model to interpret their results. The model is based on a variational principle proposed by Kelvin (1880) and later by Benjamin (1976). This model states that a steady vortex ring must have maximum energy with respect to perturbations that preserve the impulse and vorticity. They suggested that close to $L_m/D_0 \approx 4$ the piston apparatus is no longer able to supply energy at a rate compatible with

this energy requirement. Gharib *et al.* (1998) discussed that the critical value of L_m/D_0 is determined by an energy constraint associated with the maximum energy carried by a vortex when the two cores touch. For rings with thicker cores, the excess of vorticity is left in the wake. Our results show that the trailing jet appears very close to this value; however, vortices created with larger L_m/D_0 had larger circulation. This suggests that the vortex generator used in this experimental setup allows the leading vortex to feed of more vorticity above $L_m/D_0 = 4$ by producing thicker vortices.

The analytical models proposed by Linden & Turner (2001) and Mohseni & Gharib (1998) consider that the formation of vortex rings is essentially an inviscid process. However, we have shown that for Reynolds numbers of O(100) the size of the vortices will be affected and a reduction of the formation number is expected. Hence, corrections in the slug assumption have to be made by considering a parabolic profile velocity at the exit.

In their numerical simulations Rosenfeld *et al.* (1998) showed that the vortex formation number $L_m/D_0 = 4$ could be reduced up to 77% (parabolic profile) or increased by 30% by manipulating the temporal and spatial exit velocity profiles. However, the maximum value of the vortex ring circulation (scaled by the maximum discharge velocity and the diameter of the cylinder) is only weakly dependent on the discharge velocity profile or velocity program. Their values of maximum vortex ring circulation are in the range $2.61 > \Gamma/L_m D_0 > 1.85$. These numerical values agree very well with our experimental results of maximum vortex ring circulations (Figs. 3.9 and 3.10). From these figures we can also observe that the pinch-off process occurs closer to the cylinder exit for lower Reynolds numbers.

Mohseni & Gharib (1998) also suggested that thicker vortex rings could be generated using a cylinder with a time varying exit diameter during formation; therefore, the formation number could be delayed to higher values. The above was confirmed experimentally by Dabiri & Gharib (2005); they found that the vortex ring pinch-off could be delayed up to $L_m/D_0 = 8$, which is very close to our results. Mohseni *et al.* (2001) carried out numerical simulations to study the formation of vortex rings that are generated by applying a long-duration non-conservative force. They showed that the pinch-off could be delayed ($L_m/D_0 > 4$) if the trailing shear layer accelerates relative to the forming vortex ring so that the shear layer energy was sufficient to be accepted by the vortex ring making them thicker (similar to Hill's spherical vortex). We do not have any experimental evidence that this kind of acceleration is occurring. However, when Reynolds number is low enough, the leading vortex ring velocity will decrease faster and the trailing jet may eventually catch the vortex ring up or may never separate from it; therefore

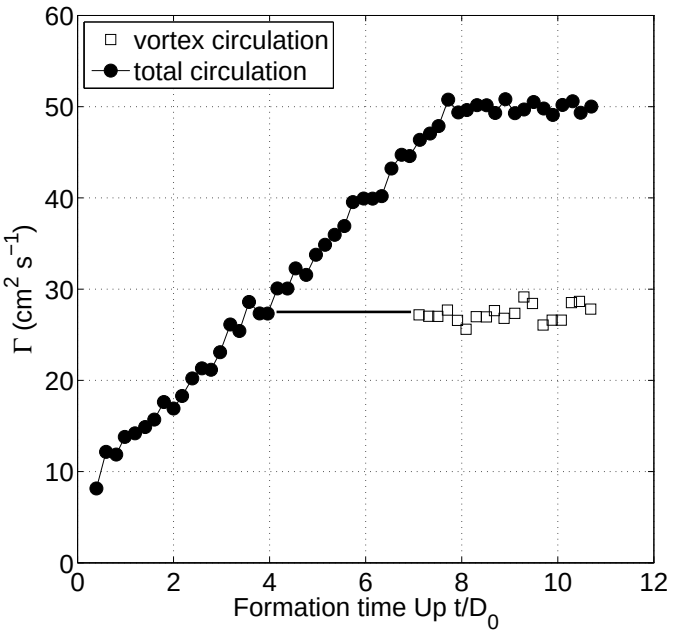

Figure 3.13: Vortex ring circulation as a function of formation time ($\bar{U_p}t/D_0$) for the case $L_m/D_0 \approx 8$, and $Re = \Gamma/\nu \approx 2800$ for pinched-off vortex ring. Taken from Gharib *et al.* (1998).

the vortex ring could accept more energy and achieve a different vortex ring configuration: increase their size and delay the formation number.

The formation number obtained by Gharib *et al.* (1998) is equal to the formation time that the total circulation in the domain reaches a value equal to the leading vortex ring after formation (Fig. 3.13). This computation requires that vortex ring has reached a physical separation (defined by Gharib *et al.* as pinch-off), but fails when this separation does not occur (which is, in fact the case for small Re). Our results from Figs. 3.9 and 3.10 are comparable with Fig. 6 from Gharib *et al.* (1998) and Fig. 9 from Rosenfeld *et al.* (1998) where circulation is plotted as a function of maximum stroke ratio L_m/D_0. Rosenfeld *et al.* presented the non-dimensional circulation of vortex rings at a formation time of $t^* \approx 10$ when physical separation is visible. Their numerical calculations reported that the maximum vortex ring circulation is reached when $6.5 \leq L_m/D_0 \leq 8$. These results are in agreement to our experimental results presented in Fig. 3.7 where physical separation is also reached. Of course, the maximum circulation could de-

pend on the time or distance at which the vortex ring circulation is measured (see Fig. 3.9a,b). For that reason we decided to consider the maximum circulation value for each stroke ratio regardless of the distance at which this value is reached: Fig. 3.10.

Akhmetov (2009 Chapter 3) pointed out the discrepancy between his experimental results (vortex ring circulation) and the results from Gharib *et al.* (1998). According to Akhmetov's data, presented in Fig. 3.10, the circulation of the vortex ring continues to increase monotonically with the jet length $L*$ at least up to $L* \approx 20$ (which corresponds to the notation of the stroke ratio $L_m/D_0 \approx 10$ adopted in this investigation). Akhmetov (2009) explained that "since the (production of) secondary vortices entrain a portion of vorticity of the vortex sheet flowing off the tube edge, it is evident that further growth of the circulation of the leading vortex ring would be limited by the circulation value that has existed by the moment when the secondary vortices start to emerge". He noted that this mechanism might explain the effect of limitation of vortex ring circulation. We observed in our experiments that as Re_0 decreases, the production of secondary vortex rings is limited or even not possible. Akhmetov (2001) also reported that the propagation vortex ring velocity practically do not change beyond $L_m/D_0 \approx 4$; while the core radius and the vortex radius increase continuously with L_m/D_0. As Re_0 decreases, Akhmetov (2001) observed that the vortex rings became practically 'spherical', similar in structure to a spherical Hill (1894) vortex. Finally, Akhmetov (2009) noted that "it is controversial to state that a dimensionless time of jet discharge equal exactly to $U_p t/D \approx 4-5$ is some universal time scale which characterizes the phenomenon of limitation of the growth of circulation of the vortex ring".

Chapter 4

Non-Newtonian vortices

In this chapter we present experimental results of the formation and evolution of vortex rings generated in non-Newtonian liquids. As mentioned before, we focused our investigation in shear-thinning liquids. The viscosity of these liquids reduces with the shear rate. We present different physical properties of the vortex rings as the trajectory, size, translation velocity, etc. We also describe how does the non-Newtonian behavior affect the critical stroke ratio for which the circulation value is maximum. To do that, we tested different liquids described in section 2.4: aqueous solutions of xanthan gum. The Reynolds number (Eq. 2.4) is defined in terms of the power law parameters: n is the power law index and m is the consistency. Most of the results in this chapter are presented in two forms. The first one is considering the same liquid (n fixed) with different piston velocities, i.e. different Reynolds numbers. In the second form, different liquids (with different n) are presented but the piston velocity is modified so the Reynolds number in all cases is the same (see table 2.1); a Newtonian liquid is also presented in this last case.

4.1 Image maps

In Figures 4.1, 4.2, 4.3 and 4.4 we present different image maps of non-Newtonian vortex rings. The image maps are: (a) the velocity field (b) vorticity field $[s^{-1}]$ (c) stream lines field (d) velocity magnitude [m/s] (e) Q criterion $[s^{-2}]$ and (f) the local strain $[s^{-1}]$. Fig. 4.1 shows image maps for a vortex ring generated in a 450 ppm (parts per million) xanthan gum aqueous solution. The stroke ratio is $L_m/D_0 = 4$ and the Reynolds number is $Re_0 = 265$. The vortex ring is located at a distance $x \approx 4D_0$ considering

maximum curvature. In this case we observe a single vortex ring without trailing jet; however, since the Reynolds number is relatively small, the vortex tends to broaden in the axial direction The above can be observed more clearly in the vorticity field (Fig. 4.1 b). The center of the vortex ring in the vector field coincides well with the vortex center in the stream lines map ($r \approx 1$), as it was observed with Newtonian vortices. The vortex center considering maximum vorticity is closer to the axis line at $r \approx 0.7$. Fig. 4.1(d) shows that the maximum velocity is located close to the axis line. The Q criterion map shows the regions with high rotation rate which correspond to the vortex ring core. Finally Fig. 4.1(e) shows the regions of flow with high strain. The largest strain occurs in front of the vortex ring as in the Newtonian case. The strain is obtained by computing the modulus of the 'rate of strain tensor' $|\boldsymbol{D}|$ (described in section 1.5) at all points in the grid. Figure 4.2 shows image maps of a vortex ring with the same liquid as the previous case, the same Reynolds number and a stroke ratio $L_m/D_0 = 8$. In this case we observe a vortex rings followed by a jet. In Fig. 4.2 (b) we observe zones of large vorticity in both the leading vortex and the trailing jet. In the Q criterion map we observe a 'deformation' of the vortex core, not seen in Newtonian vortex rings: the maximum Q value is deflected from the vortex center and the shape of the iso-Q lines are more elliptical compared with Newtonian cases. High strain values (Fig. 4.2 e) appear in front of the leading vortex as well as the trailing jet where there are large velocity gradients. Figures 4.3 and 4.4 show vortex ring for a aqueous solution of xanthan 900ppm (Xan-900); the stroke ratio is $L_m/D_0 = 4$ and $L_m/D_0 = 8$ respectively and the Reynolds number is $Re_0 = 262$. Observe that for all cases the maximum local strain values are in the order 10^0 (for example, 5.8 s^{-1} in Fig. 4.2 b). In Fig. 2.7 we presented the viscosity as function of the strain rate for different non-Newtonian liquids and we observed that the shear-thinning behavior is presented from 10^0 to 10^2 s^{-1}, i.e. we can guarantee that at the first stages of formation and evolution, we have non-Newtonian vortex rings. As the vortex velocity decreases, the local strain decreases too and the liquid in the vortex region behaves more as a viscous Newtonian fluid.

4.2 Vortex properties

In Fig. 4.5 we show the trajectories of vortex ring centers: (a) A xanthan 450ppm solution with different Reynolds numbers and a stroke ratio of $L_m/D_0 = 4$, (b) Various shear-thinning liquids and a Newtonian one with

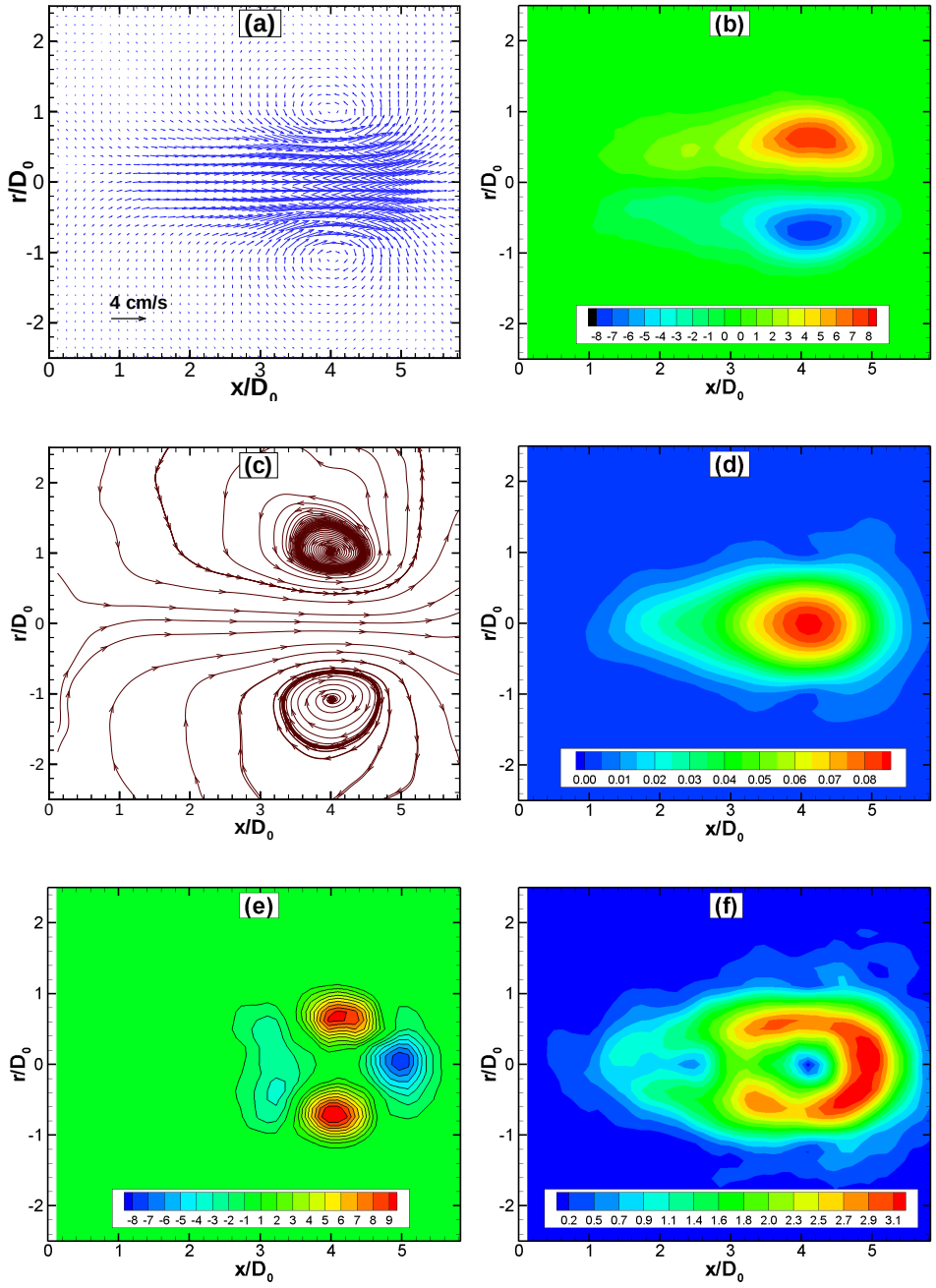

Figure 4.1: xanthan 450ppm $L_m/D_0 = 4$ $Re_0 = 265$ $x \approx 4D_0$. (a) velocity field (b) vorticity $[s^{-1}]$ (c) stream lines (d) velocity magnitude [m/s] (e) Q criterion $[s^{-2}]$ (f) local strain $[s^{-1}]$.

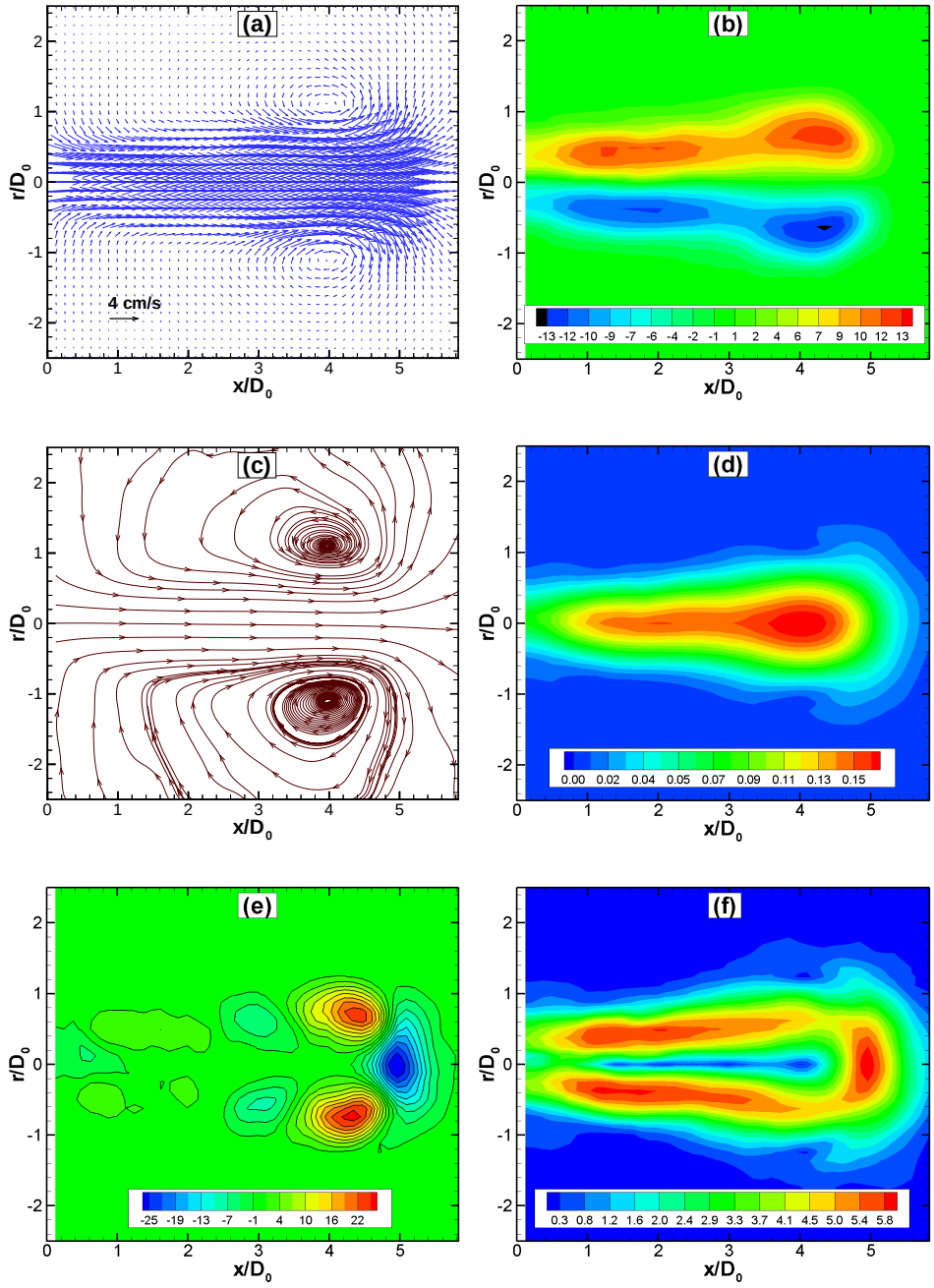

Figure 4.2: xanthan 450ppm $L_m/D_0 = 8$ $Re_0 = 265$ $x \approx 4D_0$. (a) velocity field (b) vorticity $[s^{-1}]$ (c) stream lines (d) velocity magnitude [m/s] (e) Q criterion $[s^{-2}]$ (f) local strain $[s^{-1}]$.

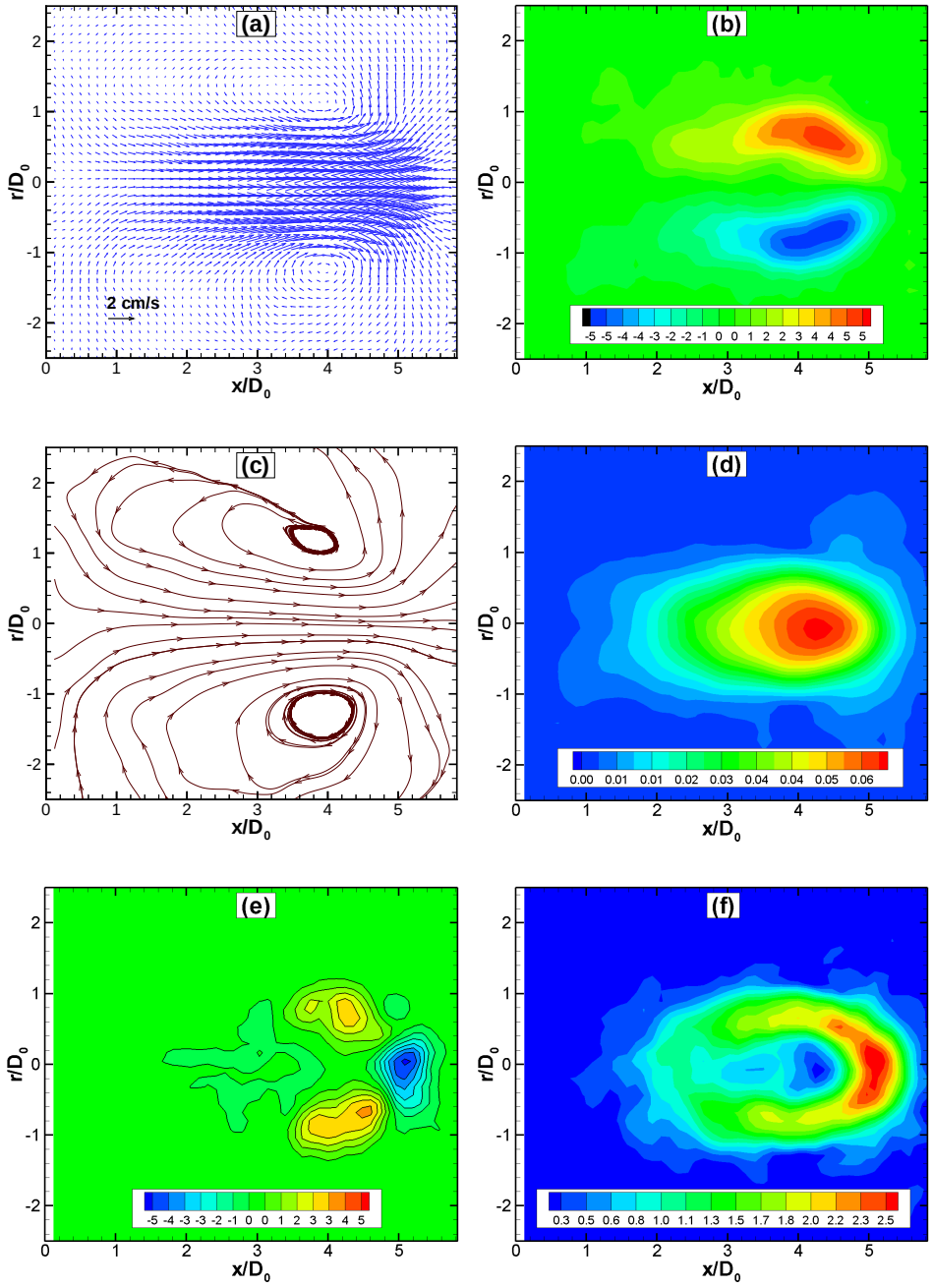

Figure 4.3: xanthan 900ppm $L_m/D_0 = 4$ $Re_0 = 262$ $x \approx 4D_0$. (a) velocity field (b) vorticity $[s^{-1}]$ (c) stream lines (d) velocity magnitude [m/s] (e) Q criterion $[s^{-2}]$ (f) local strain $[s^{-1}]$.

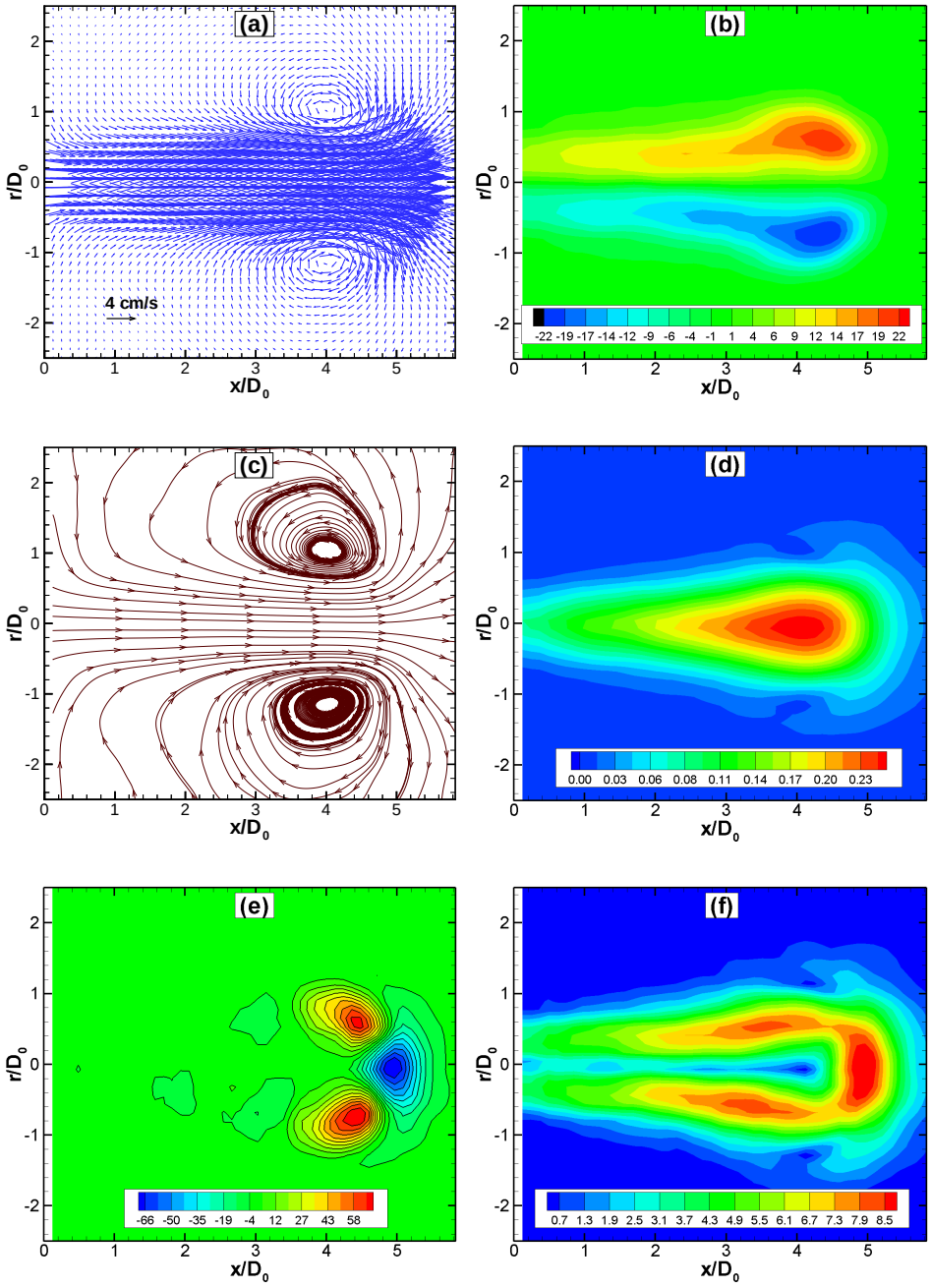

Figure 4.4: xanthan 900ppm $L_m/D_0 = 8$ $Re_0 = 262$ $x \approx 4D_0$. (a) velocity field (b) vorticity $[s^{-1}]$ (c) stream lines (d) velocity magnitude [m/s] (e) Q criterion $[s^{-2}]$ (f) local strain $[s^{-1}]$.

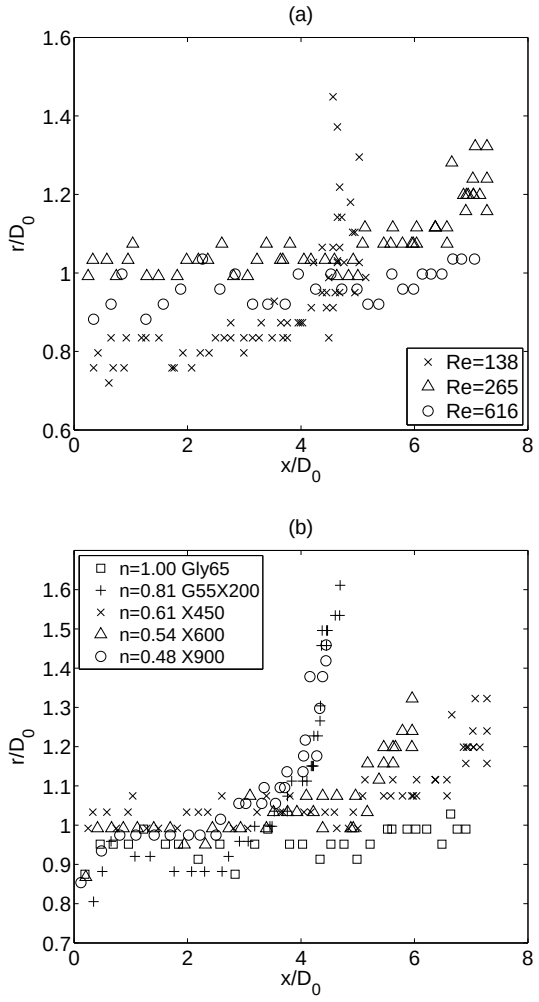

Figure 4.5: Trajectories of vortices (maximum curvature) (a) Xanthan 450ppm $L_m/D_0 = 4$ (b) Different liquids $Re_0 \approx 260$ $L_m/D_0 = 4$.

$Re_0 \approx 260$ and $L_m/D_0 = 4$. We present the position of the vortex center on the upper half plane ($r = 0$) considering maximum curvature. In Fig 4.5(a) we observe that the initial position of the vortex ring with $Re_0 = 138$ is $r \approx 0.8D_0$; just after four diameters of travel in the axial direction, the vortex ceases its movement in this direction and begins to move upwards (through the radial direction). This movement occurs symmetrically, i.e the

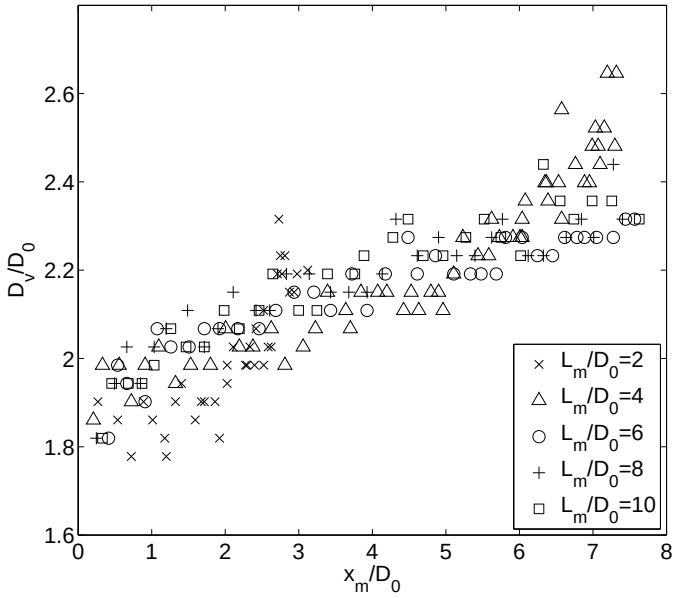

Figure 4.6: Vortex ring diameters for Xanthan 450ppp solution $Re_0 = 265$

vortex ring diameter increases. The vortex initial position for $Re_0 = 265$ and $Re_0 = 616$ is in the range $0.9 \leq r/D_0 \leq 1$, which is a slightly higher than the first case; however, in the same way, the vortex ring stops its path in the axial radiation and moves in the radial direction before it dissipates completely. Fig. 4.5(b) shows the trajectories of vortex rings generated in aqueous solutions with different concentration of xanthan gum: 450, 600, 900 ppm and an aqueous solution of glycerol 55 % weight with 200 ppm (G55X200). We also present the trajectory of a vortex ring in a Newtonian fluid: water-glycerol 65% weight (Gly65). The Reynolds number for all liquids is $Re_0 \approx 260$ (see table 2.1) and the stroke ratio is $L_m/D_0 = 4$. The initial position for all cases is near to $r = D_0$. We observe that as we increase the xanthan concentration (decreasing power index n) the vortex ring stops its axial movement closer from the exit nozzle and travels through the radial direction. The vortex path for G55X200 is similar as the Xan900 solution. For the Newtonian case, the initial vortex position is $r/D_0 \approx 1$ and it conserves the radial position along the seven diameters presented in the figure. This result is consistent with Fig 3.3 in which we plotted the trajectories of Newtonian vortices.

Fig. 4.6 shows the non-dimensional vortex ring diameter D_v/D_0 for

different stroke ratios for the Xanthan 450ppm solution and $Re_0 = 265$. x_m is the mean x-position of the centers (upper and lower vortex ring sections). First, we observe that the initial vortex diameter is in the range $1.8 \leq Dv/D_0 \leq 2$. When $L_m/D_0 = 2$ the vortex ring stops at $3D_0$ approximately. The vortex ring diameter increases as the vortex moves away from the exit nozzle and the trend is similar for all stroke ratios. This result is different from the diameters of Newtonian vortex rings where the initial diameter varies with the stroke ratio. Particulary, in Fig. 3.4 we observe that the vortex diameter increases with L_m/D_0 until it reaches a limit size close to $L_m/D_0 = 6$. The Reynolds number for these Newtonian vortices is $Re_0 = 1200$. The dependence of ring diameter on stroke ratio has been reported by Didden (1979).

Fig. 4.7 shows the horizontal velocity profiles u_x of vortex rings at the axial axis ($r = 0$): (a) A xanthan 450ppm solution with $Re_0 = 616$; (b) Different liquids with $Re \approx 260$ and a stroke ratio of $L_m/D_0 = 4$. For all cases the vortex ring center is located at $x = 4D_0$ considering the point of maximum curvature. We can observe that the maximum axial velocity values coincide well with the vortex rings center positions. Fig. 4.7 (a) shows that the value of the velocity profile u_x increases with the stroke ratio, despite the piston mean velocity is the same in all cases. This dependence on the stroke ratio was also reported in Fig. 3.5 where we presented the velocity profiles for Newtonian vortex rings; however, in that graph ($Re_0 = 1200$), the maximum velocity value was reached when $L_m/D_0 \approx 8$. This discrepancy may be due to the value of Reynolds number, i.e. in this non-Newtonian vortices Re_0 is considerably lower. Fig. 4.7 (b) shows the horizontal velocity profile of different shear-thinning fluids and the Newtonian case (Glycerol 65% solution). The piston velocity is different for all cases but the Reynolds number is the same. We observe clearly that when increasing xanthan concentration, i.e. decreasing power index n, the velocity profiles values decrease too. The velocity profile for G55X200 is similar to the Xan-900 solution profile. The velocity profile from the Newtonian case (Gly65) is the highest in the graph. We discuss this further in section 4.4.

Fig. 4.8 shows the non-dimensional propagation velocity U_v of vortex rings: (a) a xanthan 450ppm solution for different Reynolds numbers and $L_m/D_0 = 8$, (b) Different liquids with $Re_0 \approx 260$ and $L_m/D_0 = 4$. The propagation velocity is obtained by numerical differentiation of the vortex position, similar to Fig. 3.6. In Fig. 4.5 (a) we observe the vortex ring velocity for the same non-Newtonian fluid with different Reynolds numbers. The initial velocity is in the range $0.4 \leq U_v/U_p \leq 0.5$ for the three Re_0. The maximum vortex velocity ($\sim 0.6U_p$) is reached at $x \approx 3D_0$; beyond this

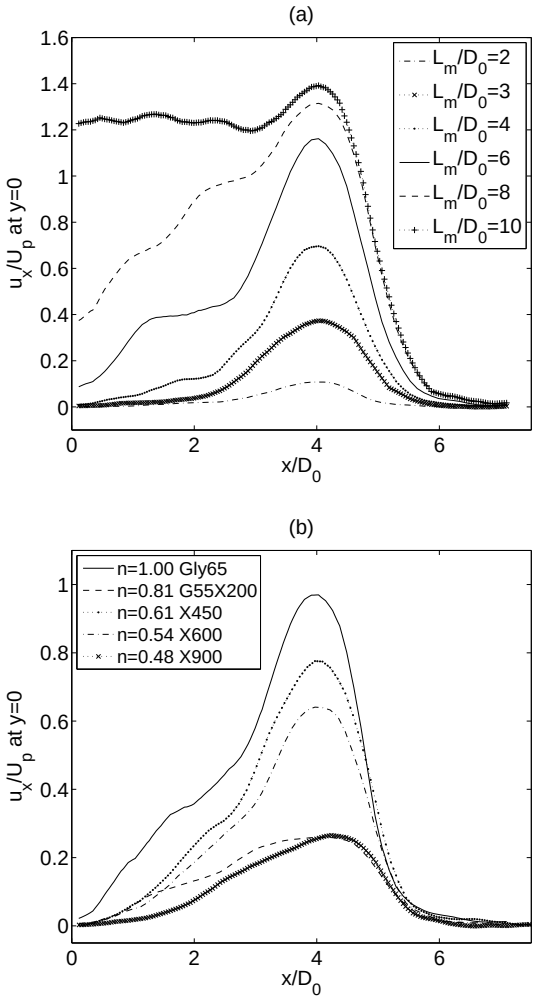

Figure 4.7: Horizontal velocity profile at $r = 0$ (a) Xanthan 450ppm $Re_0 = 616$ (b) Different liquids $Re_0 \approx 260$ and $L_m/D_0 = 4$.

distance the vortex propagation velocity remains constant for $Re_0 = 265$ and $Re_0 = 616$, but a reduction of velocity is expected farther. For the lower Reynolds number the vortex ring velocity decays closer to the nozzle, as was expected. It is important to remark that Mohseni & Gharib (1998) predicted analytically a propagation velocity of $U_v = 0.5U_p$ and Linden & Turner (2001) also predicted a maximum propagation velocity of $U_v =$

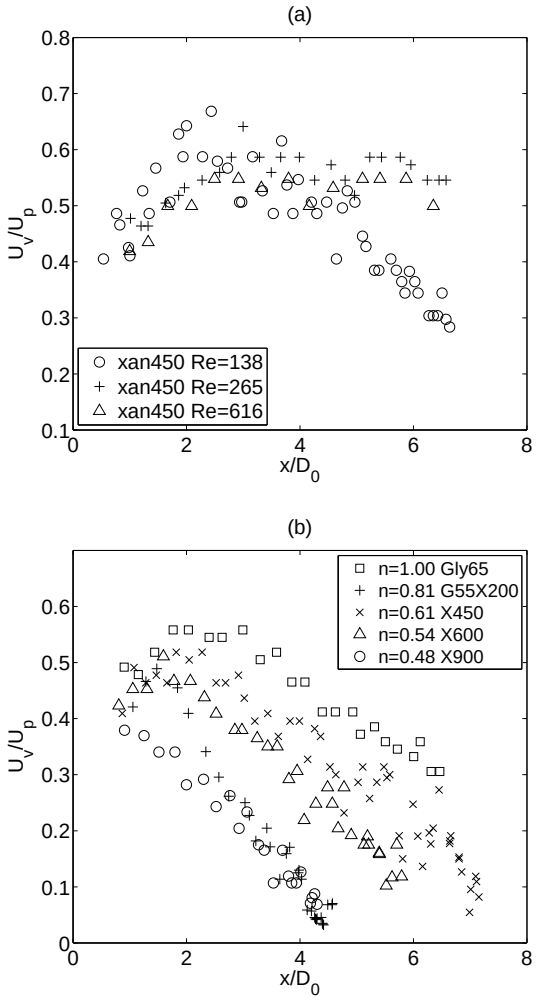

Figure 4.8: Propagation velocity of vortex rings (a) Xanthan 450ppm different Re_0 and $L_m/D_0 = 8$ (b) Differen liquids $Re_0 \approx 260$ and $L_m/D_0 = 4$.

$0.7U_p$ (see Fig. 3.11), both in Newtonian fluids. Fig 4.8 (b) shows the propagation velocity of vortex rings in different non-Newtonian liquids (the same reported). The mean piston velocity is different in each liquid, but in the same way as before, the Reynolds number is the same for all cases. The stroke ratio is $L_m/D_0 = 4$. The initial velocity also lays in the range $0.4 \leq U_v/U_p \leq 0.5$. It is interesting to note that the vortex propagation

decreases with the xanthan concentration presented in the solution. On the contrary, the propagation velocity for the Newtonian case is the highest. This graph is consistent with Fig 4.7(b) where we observe that the horizontal velocity u_x decreases with the xanthan concentration and the maximum velocity occurs when the liquid is Newtonian. Theses issues will be discussed later in this chapter.

4.3 Vortex circulation

Fig. 4.9 shows the non-dimensional vortex ring circulation as a function of the distance x/D_0 (a) a Xanthan 900ppm solution with $Re_0 = 262$ and different stroke ratios, (b) different liquids with $Re \approx 260$ and $L_m/D_0 = 8$. The vortex circulation was obtained using Eq. 1.7. The points plotted correspond to the average of 5 different runs of the piston and the error bars represent the standard deviation. It is important to note that for all non-newtonian fluids studied in the present thesis, we did not observe a 'physical separation' between the leading vortex ring and its trailing jet (large stroke ratios). Here we show the vortex circulation of one liquid (Fig. 4.9 a). We observe that for $L_m/D_0 = 4$ the vortex circulation decreases as soon as the vortex is forming. For larger stroke ratios the vortex circulation first increases, reaches a maximum value and beyond a certain distance x/D_0 from the the exit, the circulation decreases. We observe that for $L_m/D_0 = 8$ the vortex circulation remains constant in the range presented in the graph. The distance for which the vortex circulation decays, depends on the stroke ratio and in general on the Reynolds number. In Fig. 4.9(b) we present the vortex circulation for the same shear-thinning fluids presented in previous graphs and the Newtonian liquid Gly-65% for a stroke ratio $L_m/D_0 = 8$. The Reynolds number is the same in all cases. We observe that, at any distance, the circulation value is slightly larger for liquids with lower xanthan gum concentration. In other words, the vortex circulation is larger for larger power index n values. It is interesting to note that the circulation trend for all liquids is similar.

Fig. 4.10 shows the non-dimensional vortex ring circulation as a function of the stroke ratio L_m/D_0. (a) Xanthan 450ppm solution with $Re_0 = 265$ (b) Xanthan 900ppm with $Re_0 = 262$. The curves correspond to different vortex ring positions, considering maximum curvature. As we expected, the maximum vortex ring circulation for each stroke ratio depends on the distance of measurement. This result has been reported by Rosenfeld *et al.* (1998) for Newtonian vortex rings. Fig. 4.10 (a) shows that the maximum val-

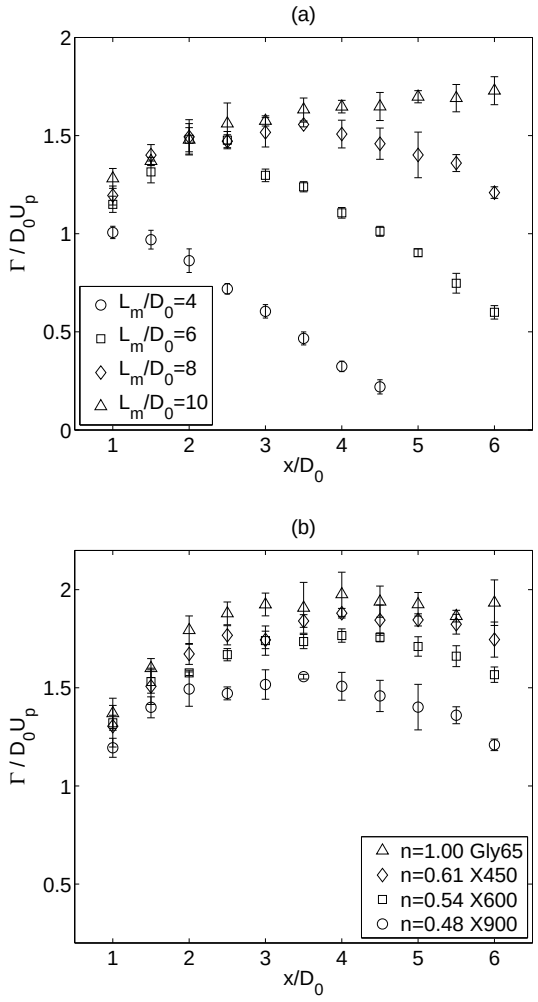

Figure 4.9: Non-dimensional vortex ring circulation as a function of the distance x/D_0 (a) Xanthan 900ppm $Re_0 = 262$ (b) Different liquids with $Re_0 \approx 260$ and $L_m/D_0 = 8$.

ues of vortex ring circulation for L_m/D_0 =1,2,3 occur at a distance close to $x/D_0 = 1$. For larger stroke ratios the maximum circulation is reached farther. Fig. 4.10 (b) shows the same plot for a liquid with more xanthan gum concentration. The trend is similar; however, despite the fact that the Reynolds number is the same, the maximum vortex ring circulation for each stroke ratio is lower than the previous case.

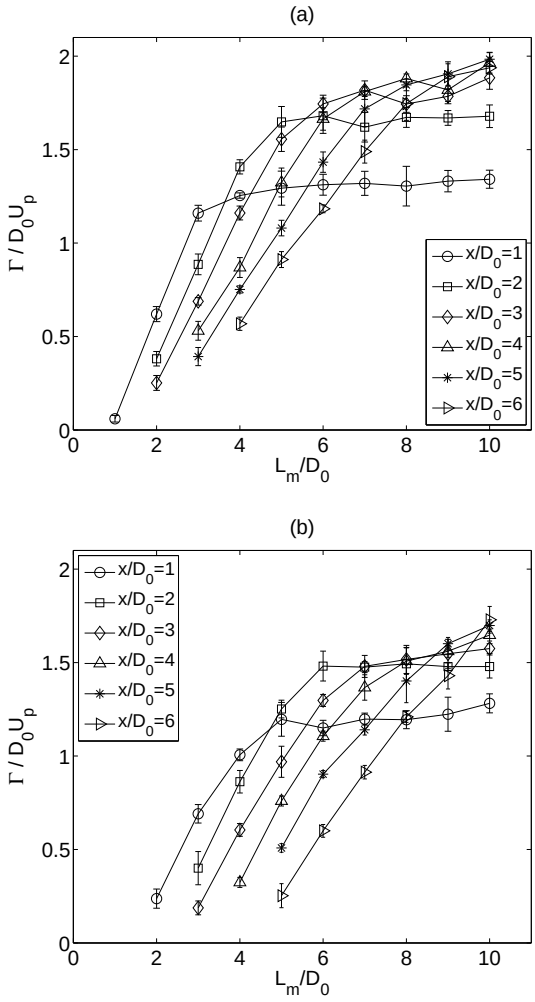

Figure 4.10: Non-dimensional vortex ring circulation as a function of L_m/D_0 at different distances (a) Xanthan 450ppm $Re_0 = 265$ (b) Xanthan 900ppm $Re_0 = 262$.

Fig. 4.11 shows the non-dimensional maximum vortex circulation as a function of L_m/D_0 for (a) Xanthan 450ppm solution with different Reynolds numbers and (b) different liquids with $Re_0 \approx 260$. In Fig. 4.11(a) we observe that for stroke ratios $L_m/D_0 \leq 4$ the vortex circulation is larger as Reynolds number is reduced (compare the cases $Re_0 = 138$ and $Re_0 = 616$). This results is similar to the presented in Fig. 3.10, where the vortex ring

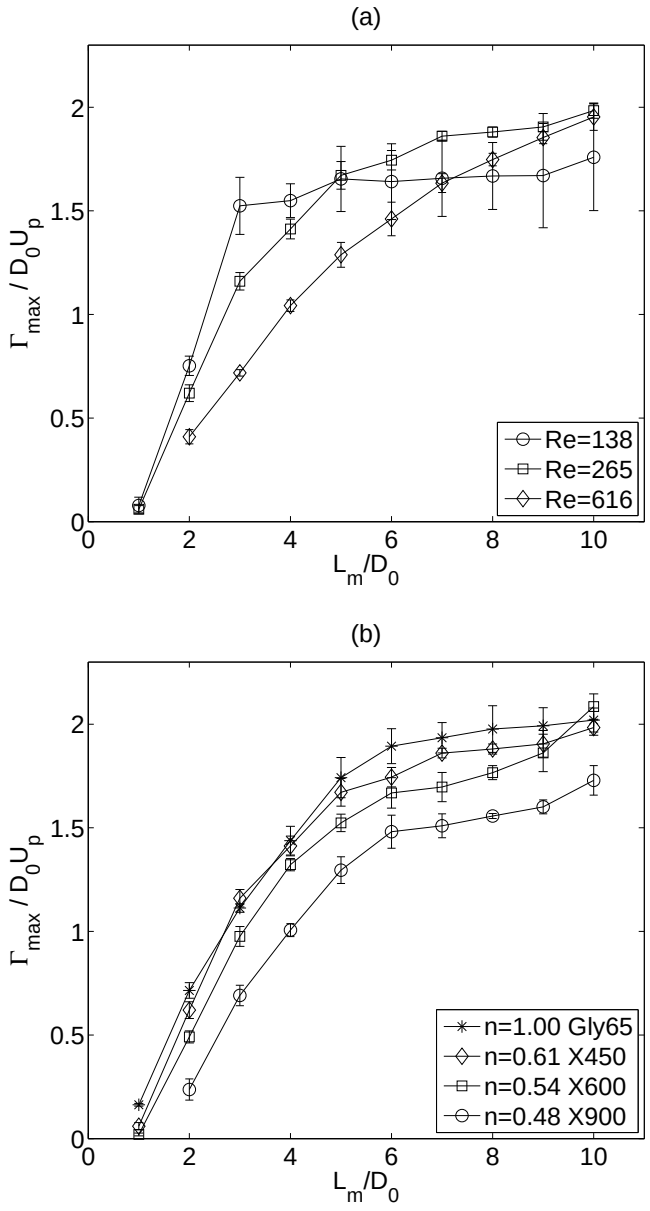

Figure 4.11: Maximum vortex ring circulation as a function of L_m/D_0 (a) Xanthan 450ppm (b) Different liquids $Re_0 \approx 260$.

circulation for $Re_0 = 150$ reached a saturation value (close to $\Gamma/D_0U_p = 2$) when $L_m/D_0 \approx 4$ while for $Re_0 = 1200$ the vortex circulation, for the same stroke ratio was $\Gamma/D_0U_p = 1.4$. All the maximum vortex ring circulation values for larger Reynolds numbers, were below this saturation value. In Fig. 4.11(a), we observe that when $Re_0 = 138$ the vortex ring circulation saturates at $\Gamma/D_0U_p \approx 1.7$. Nevertheless, unlike the Newtonian results, we observe that is possible to further increase the vortex ring circulation for larger Reynolds numbers if L_m/D_0 is high enough. Remind that as we increase the strain rate (rising up the piston velocity and Re_0) on a shear-thinning fluid, the viscosity is reduced. Fig. 4.11(b) shows the maximum vortex ring circulation for different shear thinning liquids and the Newtonian liquid Gly65%. We kept the Reynolds number fixed, in order to study the effect of the power index n on the vortex ring circulation. Remember that n is related with the slope of the line obtained in the plot viscosity versus strain rate; while the consistency m is related to the viscosity when $\dot{\gamma} \to 0$. First we observe that the larger the xanthan gum concentration the lower the vortex vortex ring circulation for each L_m/D_0. The Newtonian liquid has the largest values of circulation. In other word, the vortex ring circulation increases with n. It is important to observe that the trend of the curves for all liquids is very similar: the vortex ring circulation increases with the stroke ratio and close to $l_m/D_0 = 6$, we detect a change of slope, which suggest that the vortex has reached a 'saturation' state of formation.

4.4 Discussion

To aid our discussion, we solve the flow through a round pipe for a power law fluid. The purpose of this exercise is to gain some insight in the production of vorticity within the tube. Consider the flow through a circular tube with radius R shown in Fig. 4.12. We assume that the flow is symmetric, steady, laminar, incompressible and fully developed; the gravity is negligible and there are isothermal conditions. The axial velocity $u_x = u_x(r)$, $u_\theta = 0$ and $u_r = 0$; thus, the continuity equation is satisfied identically and the momentum balance is expressed as:

$$0 = -\frac{\partial p}{\partial x} + \frac{1}{r}\frac{\partial}{\partial r}(r\tau_{rx}) \tag{4.1}$$

where the pressure gradient $-\partial p/\partial x = G =$ constant. Using the definition of shear stress for a power-law fluid we obtain

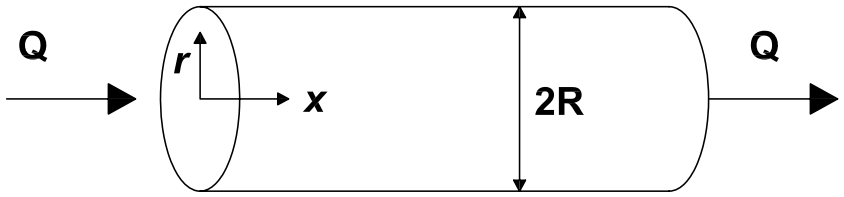

Figure 4.12: Flow through a circular tube

$$0 = Gr + \frac{\partial}{\partial r}\left[rm\left(\frac{\partial u_x}{\partial r}\right)^n\right] \tag{4.2}$$

Integrating we find (considering symmetry conditions)

$$\frac{\partial u_x}{\partial r} = -\left(\frac{G}{2m}\right)^{1/n} r^{1/n} \tag{4.3}$$

Integrating again, the axial velocity can be obtained, considering non-slip at the wall

$$u_x = \frac{n}{n+1}\left(\frac{G}{2m}\right)^{1/n}\left[R^{(n+1)/n} - r^{(n+1)/n}\right] \tag{4.4}$$

In figure 4.13(a) we show the axial velocity profile of fluids with different power law index n; we consider G, m, and R constants. For a Newtonian fluid ($n = 1$) we observe a parabolic profile; a more pluglike velocity profile is observed as n decreases; i.e. the axial velocity at the tube center becomes flatter. We also observe that the velocity close to the wall is larger as we decrease n. We can determine the flow rate by integrating the velocity profile

$$Q = \int_0^{2\pi}\int_0^R u_x r dr d\theta = 2\pi\int_0^R u_x r dr \tag{4.5}$$

$$Q = \frac{\pi R^3}{1/n+3}\left(\frac{GR}{2m}\right)^{1/n} \tag{4.6}$$

G can be understood as the constant force (per volume) acting over the slug of fluid to conserve the flow rate Q constant. This force is related to the motor torque acting over the piston. We can determine the actual flow rate by computing the volume of fluid discharged through the tube exit during a known time:

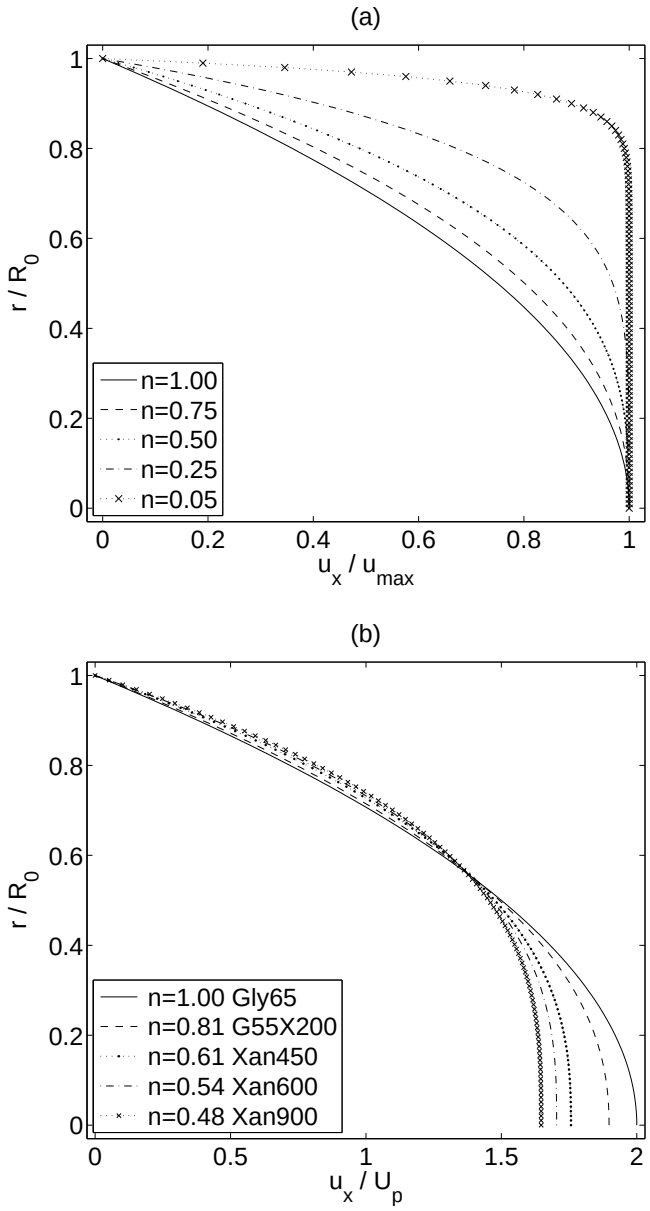

Figure 4.13: Axial velocity profile (a) different n with constant G,m and R, (b) test liquids used in the present investigations for $Re_0 \approx 260$.

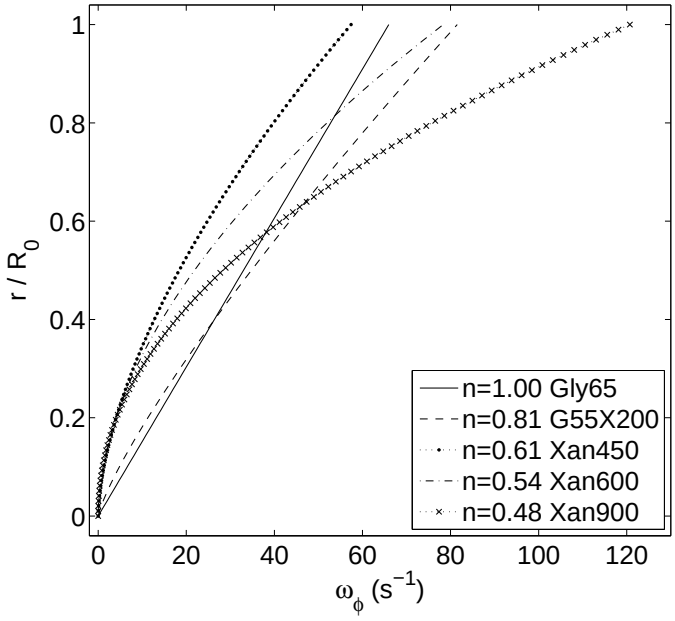

Figure 4.14: Vorticity distribution for the test liquids

$$Q = \frac{\pi R^2 L_m}{T_0} = \pi R^2 U_p \tag{4.7}$$

where L_m is the total piston displacement, T_0 is the discharge time and U_p is the piston velocity. We assume that the piston has an impulsive velocity program. Substituting expression 4.7 in Eq. 4.6, we obtain

$$G = \frac{2m}{R}\left[\left(\frac{U_p}{R}\right)\left(\frac{1}{n}+3\right)\right]^n \tag{4.8}$$

thus, the axial velocity can be expressed as:

$$u_x = \frac{3n+1}{n+1}\left[1 - \frac{r^{(n+1)/n}}{R^{(n+1)/n}}\right] U_p \tag{4.9}$$

Considering the properties of the liquids presented in table 2.1, we can compute the actual axial velocity using Eq. 4.9. The velocity profiles are presented in Fig. 4.13(b). We present liquids with different xanthan concentration but with similar Reynolds number $Re_0 \approx 260$. For all cases the maximum velocity value is located at the center of the tube. The maximum

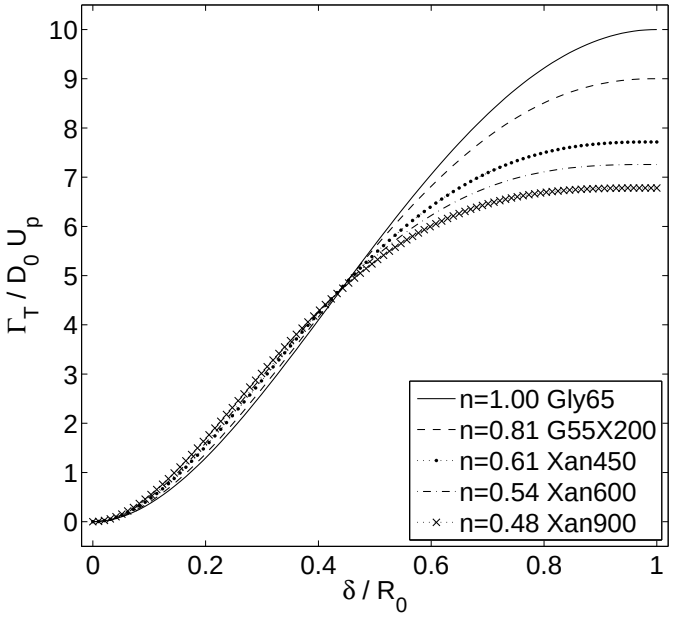

Figure 4.15: Total circulation as a function of δ for the test liquids; $L_m/D_0 = 5$.

velocity for the Newtonian fluid (Gly-65%) is $u_{max} = 2U_p$. The maximum velocity for the shear-thinning liquids is lower than this value. However; as n decreases, the velocity at the wall can be slightly larger than the Newtonian case. This can be explained as follows: the shear rate is larger close to the wall; in this zone, the apparent liquid viscosity for shear-thinning liquids decreases considerable and thus, the liquid flows easier close to the wall. We can also determine the vorticity distribution:

$$\omega_\phi = -\frac{\partial u_x}{\partial r} = \frac{3n+1}{n}\left[\frac{r^{1/n}}{R^{(n+1)/n}}\right]U_p \tag{4.10}$$

thus, the vorticity at the wall is

$$\omega_\phi|_{\text{wall}} = \frac{3n+1}{n}\frac{U_p}{R} \tag{4.11}$$

In Fig. 4.14 we show the vorticity distribution for the test liquids at different distances from the tube center. We observe that for all cases, the vorticity value increases as we approach to the wall. For the Newtonian case the dependence with r is linear. It is interesting to note that for the shear-

thinning liquid with $n = 0.61$ (Xan-450ppm) the vorticity is always lower than the Newtonian case, while for the liquid with $n = 0.48$ (Xan-900ppm) the vorticity increases considerably close to the wall. The vorticity close to the tube center is larger for the Newtonian liquid.

Finally we can take the 'slug' approximation model described in section 1.4.2 to determine the circulation ejected through the tube nozzle. The circulation was defined in Eq. 1.23:

$$\Gamma = \int_0^{T_0} \left[-\frac{u_x^2}{2} \right]_{R-\delta}^{R} dt$$

where δ is the boundary layer size; hence, we obtain

$$\Gamma_T = \left(\frac{3n+1}{n+1} \right)^2 R^{-2(n+1)/n} \left[R^{(n+1)/n} - (R-\delta)^{(n+1)/n} \right]^2 \frac{U_p L_m}{2} \quad (4.12)$$

With this formula we obtain the total circulation ejected during the piston displacement. For large L_m/D_0, part of this circulation is confined inside the leading vortex ring and another part is left behind in a wake. Some circulation is canceled by the entraining fluid outside the tube (Didden 1979). In Fig. 4.15 we show the total circulation as a function of δ for a stroke ratio of $L_m/D_0 = 5$. For small δ the total circulation is slightly larger as n decreases; the circulation for the Newtonian liquid is the lowest. For large δ values, the total circulation is larger as n increases; the circulation for the Newtonian liquid case is notably larger than the others as $\delta \to R$. Remember that the Reynolds number is the same for all liquids. There is a crossing point where all shear thinning curves 'touch' the Newtonian curve. This point is located at different δ for each liquid, but is close to $\delta \approx 0.45R$. When δ has this value the total circulation values are approximately the same for all liquids for any L_m/D_0.

In Fig. 4.16 we show the total circulation as a function of L_m/D_0 for (a) $\delta = 0.052R$ and (b) $\delta = R$. We observe that when δ is small, the circulation is larger for the most shear-thinning fluid (Xan-900ppm); however, if we consider $\delta = R$, the total circulation ejected from the tube is reduced as n decreases. The question is, how large is the boundary layer δ for a given liquid?. The slug approximation for Newtonian vortices described before, assumes that $\delta \ll R$ and the velocity at the edge of the boundary layer is equal to the piston velocity U_p. As the Reynolds number decreases, this approximation becomes incorrect; observe the velocity profiles in Fig. 4.13(b). In fact, we can observe that the maximum velocity for any case

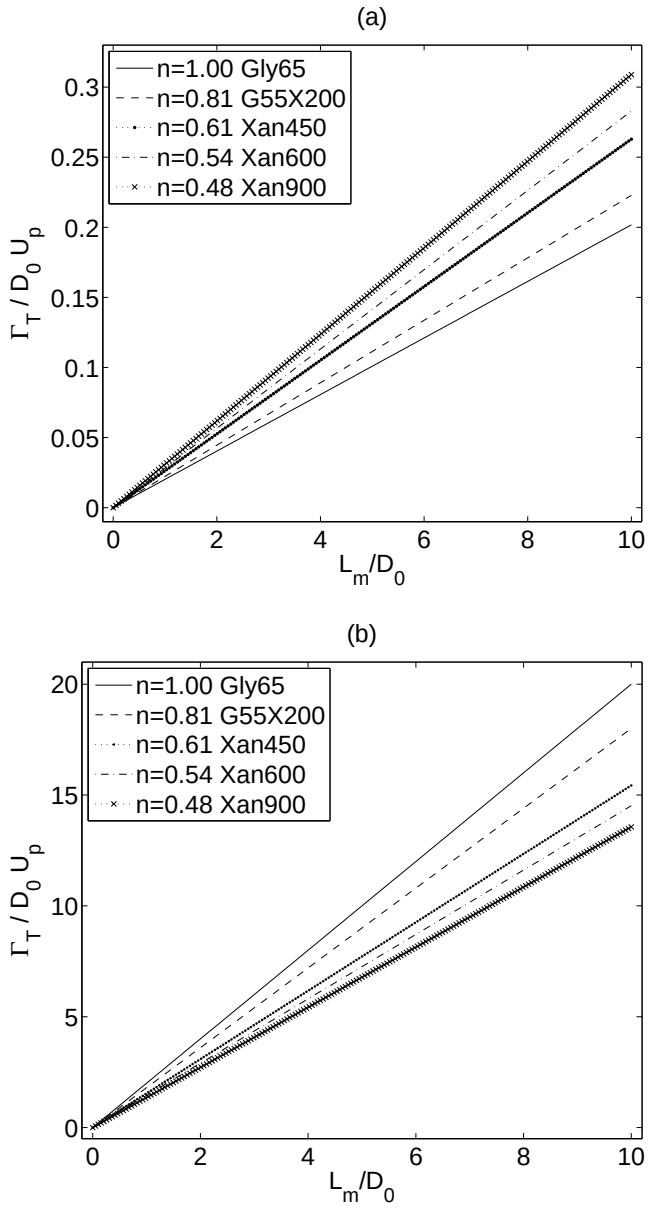

Figure 4.16: Total circulation as a function of L_m/D_0 for the test liquids (a) $\delta = 0.052R$ (b) $\delta = R$.

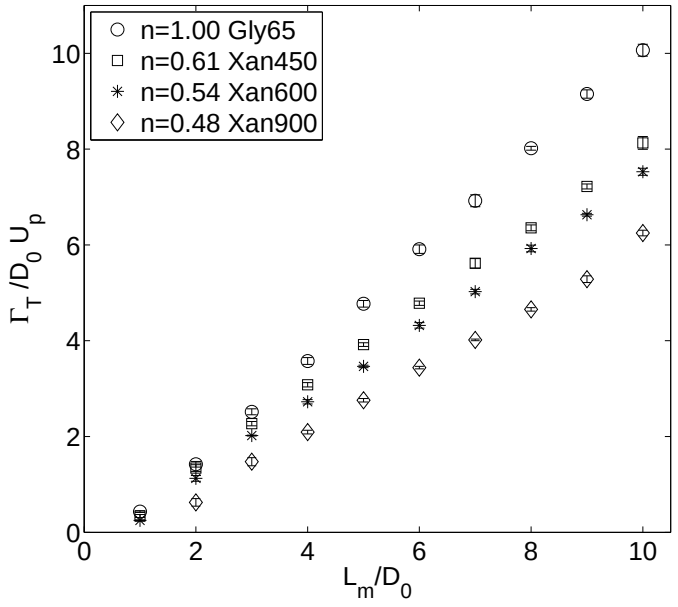

Figure 4.17: Experimental total circulation as a function of L_m/D_0 for the test liquids.

is $u_{max} > 1.5Up$. We can guarantee laminar flow because the Reynolds number $Re_0 \approx 260$ is sufficiently small. Didden (1979) also reported that at large discharge times, boundary layer grows leading to an increment in the velocity at the center of the cylinder in order to satisfy continuity. These arguments suggest that δ might be as large as the radius.

In Fig. 4.17 we show the experimental total circulation for the test liquids. The total circulation is determined by integrating the vorticity $\omega_\phi > 0$ in the visible domain (see Fig. 3.7). Similarly to the vortex circulation, the total circulation changes along the axis direction; therefore, we plot the maximum circulation value for each L_m/D_0. We observe that the total circulation increases with the stroke ratio and is larger for the Newtonian case (Gly-65% $n = 1$). As n decreases the total circulation decreases too. These experimental results are in agreement with the results presented if Fig. 4.16(b) for which $\delta = R$; however, the circulation values in this plot are larger. In fact, the experimental values are approximately 50% lower than the predicted values; for the Xanthan-900ppm solution $\Gamma_{exp} \approx 0.4\Gamma_{predicted}$. The difference between the circulation values might be explained by the fact that the velocity gradients outside the cylinder are lower than inside;

therefore, the vorticity is reduced and the circulation too. As soon as the flow is ejected from the cylinder, the jet loses its strength because of viscous dissipation. This effect is more critical for lower Re_0.

The experimental results (see Fig. 4.9 and Fig. 4.11) presented in this chapter indicate that the vortex ring circulation decreases with n. We have shown that the total circulation ejected from the tube is reduced for more shear-thinning liquids; thus, the circulation confined inside the vortex ring, will be reduced too. It is important to note that as we increase the xanthan concentration, the consistency m increases. This value is related to the liquid viscosity as the shear strain rate $\dot{\gamma} \to 0$; i.e. zones of flow where the local velocity is low (low shear strain) the apparent viscosity increases considerably. This is the case of the stagnant fluid surrounding the vortex rings in movement. For example, the vortex ring in a xanthan 900ppm solutions have to move in a more viscous stagnant fluid than any other lower concentration. Therefore, the vortex ring propagation velocity will reduce faster; this was shown in Fig.4.8 (b).

All the non-Newtonian vortex rings studied in this investigation have a considerably low Reynolds number; it was not possible to observe a 'physical separation' between the leading vortex ring and its trailing jet; some authors have stated that there is not vortex ring pinch-off if it is not possible to guarantee the mentioned separation. Therefore, it is difficult to study a vortex ring formation number. However, in Fig. 4.11(b) we observe that the vortex ring circulation increases with the stroke ratio L_m/D_0 until it reaches a 'saturation state' close to $L_m/D_0 = 6$ where we detect a change of the slope. This suggests that the vortex ring cannot attain vorticity in the same rate as L_m/D_0 increases; thus the vortex ring has reached a limited size or limited state of formation.

Chapter 5

Conclusions

The main objective of this study was to conduct experiments to analyze the formation of vortex rings at Reynolds numbers in the range 100 to 2000. To our knowledge measurements at this low Re with $L_m/D_0 > 4$ do not exist in the specialized literature. To find the conditions at which vortices are formed, we had to consider an identification scheme which was different from what had been used for flows at higher Re. We proposed the use of the so-called Q criterion to identify and measure the vortex strength. We used a calculation of the curvature of Lagrangian trajectories to locate the vortex centers. We used these techniques to analyze the formation process, obtain some vortex properties and determine the dependence of the vortex ring circulation on the stroke ratio L_m/D_0. We found the same qualitative trend as previous investigations but we found some differences in the critical value of the stroke ratio at which the circulation inside the leading vortex ring is maximum and remains constant for higher L_m/D_0. For $Re_0 = 1200$ we observed that the critical value of L_m/D_0 was approximately 8 and for $Re_0 = 150$ it was approximately 4. For the case $Re_0 = 2037$ we observed that the vortex ring circulation increases monotonically with the stroke ratio at least to $L_m/D_0 \approx 10$. We explained that these differences are, in fact, possible according to the discussion of several published works.

We also found that as the Reynolds number increases the vortex ring circulation decreases for the same L_m/D_0; this is more evident for the case for small values of Re. We explained in chapter 4 that as the thickness of the boundary layer increases, the total circulation ejected from the cylinder also increases. Evidently, for lower Reynolds numbers we have a more parabolic velocity profile inside the tube and the layer size increases. A larger boundary layer may produce thicker vortex rings which might increase their ability

to attain more vorticity and consequently more circulation. A value of the non-dimensional vortex ring circulation $\Gamma_{max}/D_0U_p \approx 2$ may indicate a saturation condition beyond which it is not possible to increase the vortex circulation for any Reynolds number.

By measuring the non-dimensional radius R_Q of the vortex rings we showed that thicker vortices can be produced as the Reynolds number decreases. We also demonstrated that the vortices generated in our experiments are thicker than those predicted analytically by Mohseni & Gharib (1998). A bigger size allows vortices to attain more vorticity, increase their circulation and therefore experience a delay in the formation number. In their conclusions, Gharib *et al.* (1998) argued that for some cases, it was possible to increase the circulation of a vortex ring after its formation through entrainment of the leading vortex of the trailing jet by the vortex ring.

In some cases (when Re was high enough), we were able to observe a 'physical separation' between the leading vortex ring and the trailing jet; This occurred when $L_m/D_0 \approx 4$ in concordance with Gharib *et al.* (1998) experiments; however, we think that for $L_m/D_0 \geq 4$, because of the proximity of the trailing jet, the vortex ring is able to increase quickly its circulation, but as soon as it reaches a saturation value, the vortex ring sheds the excess of vorticity into its wake. This phenomenon has been reported by Gharib *et al.* (1998) in their conclusions. This rapid change of circulation is less evident for lower stroke ratios $L_m/D_0 \leq 4$, where trailing jet is not present. For the case of Re=150, the vortex ring reaches this saturation state at $L_m/D_0 \approx 4$. We observed that the vortex ring circulation (for our Re numbers) changes continuously during the formation and propagation of the vortex rings. As the circulation does not remain constant, the impulse, energy, and consequently, the propagation velocity will change as well. The measurements of vortex ring diameter and velocity propagation indicate that there is a stroke ratio limit above which the vortex size and velocity cannot increase. The vortex identification scheme used in this paper allows us to obtain measurements of the vortex ring circulation with small uncertainty, since the same cutoff criterion can be used at any instant of the vortex ring formation, any distance from the exit and any Reynolds number. The experimental results are in agreement with theoretical models and numerical studies reported in the literature.

In the present investigation, we studied the vortex ring formation in shear-tinning liquids, using different xanthan gum concentrations. We carried out experiments to study some properties of these non-Newtonian vortices. We tested different liquids with different rheological properties and

change experimental configurations in order to keep the Reynolds number constant. In particular, we determined how the vortex ring circulation was affected by the power index n. We observed that the vortex diameter grows in the axial direction x in the same proportion for all L_m/D_0 and $Re_0 = 265$. The horizontal velocity at the vortex center increases with the stroke ratio for a given Re. For the same Reynolds number $Re_0 \approx 260$ and $L_m/D_0 = 4$ the horizontal velocity decreases with the power index n. The vortex ring propagation velocity also decreases with n. This can be explained by the fact that the stagnant fluid surrounding the vortex ring is more viscous than the vortex itself; i.e. when the shear rate $\dot{\gamma} \approx 0$ the liquid viscosity (which is related with the consistency m), increases. We observed that at low $\dot{\gamma}$ the viscosity is larger as the concentration of xanthan gum increases. The larger the concentration, the faster the propagation velocity and the horizontal velocity decrease.

Our results indicate that the vortex ring circulation decreases with n. We showed that the total circulation ejected from the tube is reduced for more shear-thinning liquids considering $\delta > 0.5R_0$. From the axial velocity profiles, we concluded that the size of the boundary layer δ is as large as the radius itself. If the total plug circulation decreases for more shear thinning fluids, we expect that the vortex ring circulation will be reduced too. We also observed that the vortex circulation increases with L_m/D_0 until it reaches a change of the slope close to $L_m/D_0 = 6$, for which the vortex ring has reached a limited state of formation.

Appendix A

Conference presentations


ISSN 0187-4713
SUPLEMENTO DEL BOL. SOC. MEX. FIS. 21-3, 2008
LI Congreso Nacional de Física
II Congreso Latinoamericano de Física
XXIII Encuentro Nacional de Divulgación Científica
XIV Congreso de la División de Fluidos y Plasmas
Universidad Autónoma de Zacatecas
Zacatecas
Del 20 al 24 de octubre de 2008
PROGRAMAS Y RESÚMENES
SMF
Sociedad Mexicana de Física

Fluidos No Newtonianos ***Salón Caxcan***

Modera: Dr. Arturo Olvera, IIMAS-UNAM

S.VII.1 **Dynamics of non Newtonian Vortex Rings**
Carlos Palacios Morales, Ian Monsivais Montoliu, Roberto Zenit Camacho Instituto de Investigaciones en Materiales, UNAM chacharly@yahoo.com The dynamics of formation and evolution of vortex rings created in a piston-cylinder arrangement is studied. The purpose of this investigation is to compare the formation process of Newtonian and non Newtonian vortex rings. The ratio of the piston displacement L and the nozzle diameter D determine the vortex size and evolution. Experiments with different conditions are presented: translation velocity of the piston, stroke ratio L/D, a Newtonian fluid and a shear thinning fluid. Measurements of the 2D velocity field were obtained with a PIV technique. The vortex circulation was computed considering a vortex identification scheme (Q criterion). In its evolution the vortex 'feeds' of vorticity and increases its size; after some time its strength begins to dissipate. In the case of Newtonian fluids the results show that there is a critical number of L/D above which the circulation inside the vortex can not increase and remains constant (Gharib et al., 1998). The critical number, called formation number is between 3.5 and 4.5 for Newtonian fluids. We have observed that for a shear thinning fluid the critical number can increase considerably (up to twice the Newtonian value). Also, we observed that the shape of the rings is modified by the non-Newtonian properties of the flu

fluido puede describirse como un líquido Newtoniano que llega en tiempos cortos a un flujo estacionario, otra parte del mismo, dependiendo de la rapidez de corte, no presenta flujo o su flujo presenta grandes fluctuaciones de velocidad. Los perfiles de flujo explican también algunas de las diferencias observadas en las curvas de esfuerzo vs. rapidez de corte, en la birrefingencia y en el dicroísmo en flujo de la muestra. Mostramos también algunas similitudes entre el comportamiento de este sistema y lo que se observa en polímeros y otros sistemas de micelas cilíndricas.

S.VII.3 **Análisis de los flujos estacionarios de soluciones diluidas de polímeros desde el punto de vista de la deformación afín.** *Michael J. Brown , jackgibbs1@gmail.com, Instituto de Investigaciones en Materiales, UNAM;y Enrique Geffroy Departamento de Reología, Instituto de Investigaciones en Materiales Universidad Nacional Autónoma de México Ciudad Universitaria, México DF* El modelo de mancuerna Hookeana describe la dinámica de polímeros en solución mediante una competencia entre la deformación afín por el flujo y la relajación lineal de la mancuerna hacia el equilibrio. Para flujos estacionarios bidimensionales es factible obtener una solución cerrada del tensor de configuración de la mancuerna que consta de integrales de deformación afín los que son amortiguadas exponencialmente por la relajación. En el límite de número Deborah grande, uno puede expandir esta solución a partir de las integrales afinas. En esta plática, usaremos tal expansión asintótica regular del modelo de mancuerna Hookeana para entender el flujo cortante simple de una solución diluida de polímeros alrededor

BULLETIN
OF THE AMERICAN PHYSICAL SOCIETY

PROGRAM OF THE 61st ANNUAL MEETING OF THE DIVISION OF FLUID DYNAMICS

November 23–25, 2008
San Antonio, Texas

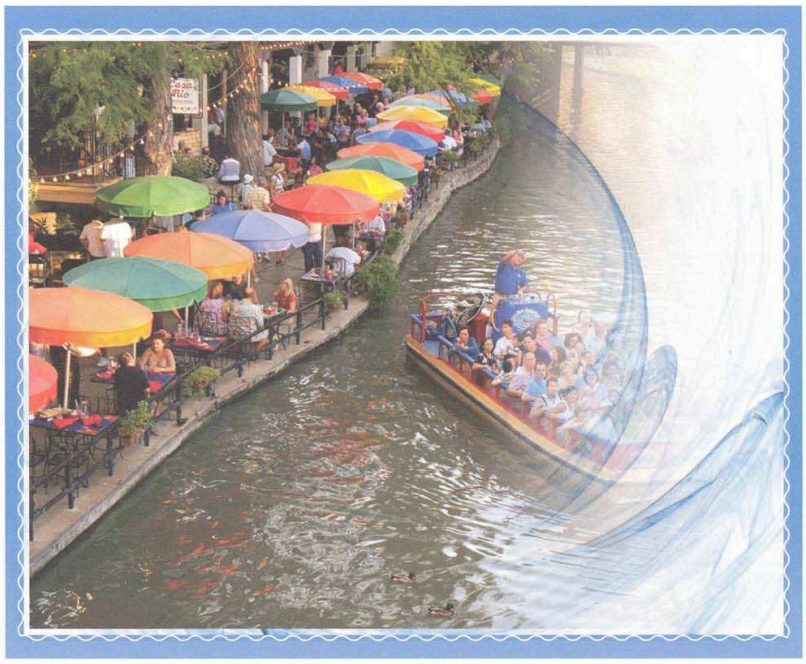

November 2008
Volume 53, No. 15

APS physics

8:26

GU 3 Dynamics of non newtonian vortex rings C. PALACIOS, I. MONSIVAIS, R. ZENIT, *Universidad Nacional Autonoma de Mexico* The dynamics of formation and evolution of vortex rings created in a piston-cylinder arrangement is studied. The purpose of this investigation is to compare the formation process of Newtonian and non Newtonian vortex rings. These kind of vortices are present in many engineering applications and natural phenomena. The ratio of the piston displacement L and the nozzle diameter D determine the vortex size and evolution. Experiments with different conditions are presented: translation velocity of the piston, stroke ratio L/D, a Newtonian fluid and a shear thinning fluid. Measurements of the 2D velocity field were obtained with a PIV technique. The vortex circulation was computed considering a vortex identification scheme (Q criterion). In its evolution the vortex ''feeds'' of vorticity and increases its size; after some time its strength begins to dissipate. In the case of Newtonian fluids the results show that there is a critical number of L/D above which the circulation inside the vortex can not increase and remains constant (Gharib *et al.*, 1998); in other words the vortex has a finite size. The critical number, called formation number, is between 3.5 and 4.5 for Newtonian fluids. We have observed that for a shear thinning fluid the critical number can increase considerably (up to twice the Newtonian value). Also, we observed that the shape of the rings is modified by the non-Newtonian properties of the fluid.

9:05

GU 6 Vortex Ring State and Asymmetric Thrust Oscillations* GREGORY McCAULEY, OMER SAVAS, *University of California Berkeley* FRANCIS CARADONNA, *NASA Ames Research Center* When the helical vortices of a rotor are not convected away, the vortices may form a ring-like structure about the rotor disk. This vortex ring state (VRS) is most common during rapid descent and leads to thrust oscillations coupled to the formation and subsequent breakdown of the ring. Experimental observations at and near VRS were made using strobed particle image velocimetry on a three-blade rotor in a towing tank. Simultaneous strain gage readings allowed direct measurement of the rotor's thrust history in this state. Operating conditions near the cusp of VRS were investigated to offer insight into the initial evolution of this undesirable state. In addition, asymmetries in the periodic thrust histories during non-axial descent are analyzed in conjunction with corresponding vorticity evolutions. Salient features of the vortex wake structure during highly asymmetric thrust oscillations are discussed in contrast to VRS cases with nearly symmetric thrust oscillations.

*Supported by NASA Ames Research Grant NCC2-5507.

Bibliography

[1] D.G. Akhmetov, "Formation and basic parameters of vortex rings", J. Appl. Mech. Tech. Phys. **42**(5), 794-805 (2001).

[2] D.G. Akhmetov, *Vortex Rings*, Springer (2009).

[3] E.J. Anderson and M.E. Demont, "Jet flow in steadily swimmming adult squid", J. Exp. Biol. **208**, 1125-1146 (2005).

[4] H.A. Barnes, J.F. Hutton and K. Walters, *An Introduction to Rheology*, Elsevier (1989)

[5] I.K. Bartol, P.S. Krueger, W.J. Stewart and J.T. Thompson, "Pulsed jet dynamics of squid hatchlings at intermediate Reynolds numbers", J. Exp. Biol. **212** 1506-1518 (2009a).

[6] I.K. Bartol, P.S. Krueger, W.J. Stewart and J.T. Thompson, "Hydrodynamics of pulsed jetting in juvenile and adult brief squid Lolliguncula brevis: evidence of multiple jet modes and their implications for propulsive efficiency", J. Exp. Biol. **212** 1889-1903 (2009b).

[7] N. Benard, S. Jarny and D. Coisne, "Definition of an experimental blood like fluid for laser measurements in cardiovascular studies", Appl. Rheol. **17**, 44251-1 - 44251-8 (2007).

[8] T.B. Benjamin, "The alliance of practical and analytical insights into the non-linear problems of fluid mechanics". In *Applications of Methods of Functional Analysis to Problems in Mechanics*. (Ed. P. Germain & B. Nayroles). Lecture Notes in Mathematics, **503** 8-28 Springer (1976).

[9] W. Braun, F. de Lillo and B. Eckhardt, "Geometry of particle paths in turbulent flows", J. Turbul. **7**, 62 (2006).

[10] P. Chakraborty, S. Balachandar and R.J. Adrian, "On the relation between local vortex identification schemes", J. Fluid Mech. **535**, 189-214 (2005).

[11] M. S. Chong, A.E. Perry and B.J. Cantwell, "A general classification of three-dimensional flow fields", Phys. Fluids A **2**, 765-777 (1990).

[12] J.O. Dabiri and M. Gharib, "Delay of vortex ring pinch-off by an imposed bulk counter-flow", Phys. Fluids **16** L28-30 (2004).

[13] J.O. Dabiri and M. Gharib, "Starting flow through nozzles with temporally variable exit diameter", J. Fluid Mech. **538** 111-136. (2005)

[14] J.O. Dabiri, S.P. Colin and J.H. Costello, "Fast-swimming hydromedusae exploit velar kinematics to form an optimal vortex wake", J. Exp. Biol. **209** 2025-2033 (2006).

[15] J.O. Dabiri, "Optimal Vortex Formation as a Unifying Principle in Biological Propulsion", Annu. Rev. Fluid Mech. **41** 17-33 (2009).

[16] N. Didden, "On the formation of vortex rings: Rolling-up and production of circulation", Z. Angew. Mech. Phys. **30**, 101-116 (1979).

[17] L.E. Fraenkel, "On steady vortex rings of small cross-section in an ideal fluid", Proc. Roy. Soc. Lond. **A316**, 29-62 (1970).

[18] L.E. Fraenkel, "Examples of steady vortex rings of small cross-section in an ideal fluid", J. Fluid Mech. **51** 119-135 (1972).

[19] M. Gharib, E. Rambod, K. Shariff, "A universal time scale for vortex ring formation", J. Fluid Mech. **360** 121-140 (1998).

[20] M. Gharib, E. Rambod, A.Kheradvar, D.J. Sahn, "Optimal vortex formation as an index of cardiac health", Proc. Natl. Adad. Sci. USA **103** 6305-6308 (2006).

[21] A. Glezer, "The formation of vortex rings", Phys. Fluids **31** 3532-3542 (1988).

[22] A. Glezer and D. Coles, "An experimental study of a turbulent vortex ring", J. Fluid Mech. **211**, 243-283 (1990).

[23] G. Haller, "An objective definition of a vortex", J Fluid Mech. **525**, 1-26 (2005).

[24] W.M. Hicks, "Researches on the theroy of vortex rings-Part II.", Philos. Trans. R. Soc. London A **176**, 725-780. (1885).

[25] M.J.M. Hill, "On a spherical vortex", Philos. Trans. R. Soc. London A **185**, 213-245. (1894).

[26] J.C.R. Hunt, A. Wray and P. Moin, "Eddies, stream, and convergence zones in turbulent flows", Center for Turbulence Research Report CTR-S88 (1988).

[27] S. James and C. Madnia, "Direct numerical simulation of a laminar vortex ring", Phys. Fluids **8**, 2400-2414. (1996).

[28] J. Jeong and F. Hussain, "On the identification of a vortex", J. Fluid Mech. **285**, 69-94 (1995).

[29] F. Kaplanski and U. Rudi, "Dynamics of a viscous vortex ring", Int. J. Fluid Mech. Res. **26**, 618-630 (1999).

[30] L. Kelvin, "The translatory velocity of a circular vortex rings", Philos. Mag. **33**, 511-512 (1867).

[31] L. Kelvin, "Vortex statics", Philos. Mag. **10**, 97-109 (1880).

[32] P.S. Krueger, J.O. Dabiri and M. Gharib, "The formation number of vortex rings formed in uniform backgroud coflow", J. Fluid Mech. **556** 147-166 (2006).

[33] H. Lamb, *Hydrodynamics*, Cambridge Univ. Press (1932).

[34] T.T. Lim and T.B. Nickels, "Vortex rings", In *Fluid Vortices* (Ed. S.I. Green) 95-153. Kluwer (1995).

[35] P.F. Linden and J.S. Turner, "The formation of 'optimal' vortex rings, and the efficiency of propulsion devices", J. Fluid Mech. **427** 61-72 (2001).

[36] C. Macosko, *Rheology-Principles, Measurements and Applications*, John Wiley & Sons (1994).

[37] T. Maxworthy, "Some experimental studies of vortex rings", J. Fluid Mech. **81** 465-495 (1977).

[38] A. Michalke and A. Timme, "On the inviscid instability of certain two-dimensional vortex-type flows", J. Fluid Mech. **29** 647-666 (1967).

[39] K. Mohseni and M. Gharib, "A model for universal time scale of vortex ring formation", Phys. Fluids **10** 2436-2438 (1998).

[40] K. Mohseni, H. Ran and T. Colonius, "Numerical experiments on vortex ring formation", J. Fluid Mech **430** 267-282 (2001).

[41] D.W. Moore, "The effect of compressibility on the speed of propagation of a vortex ring", Proc. R. Soc. London **A397**, 87-97 (1985).

[42] J. Norbury, "A steady vortex ring close to Hill's spherical vortex", Proc. Camb. Phil. Soc. **72**, 253-84 (1972).

[43] J. Norbury, "A family of steady vortex rings", J. Fluid Mech. **57** 417-431 (1973).

[44] A. Okubo, "Horizontal dispersion fo floatable trajectories in the vicinity of velocity singularities such as convergencies", Deep-Sea. Res. **17**, 445-454. (1970).

[45] N.T. Oullette and J.P. Gollub, "Curvature Fields, Topology, and the Dynamics of Spatiotemporal Chaos", Phys. Rev. Lett. **99**, 194502 (2007).

[46] M. Raffel, C. Willert and J. Kompenhans, *Particle Image Velocimetry. A practical guide*, Springer (1998).

[47] M. Rosenfeld, E. Rambod and M. Gharib, "Circulation and formation number of laminar vortex rings", J. Fluid Mech. **376**, 297-318 (1998).

[48] P.G. Saffman, *Vortex Dynamics*, Cambridge Univ. Press (1992)

[49] K. Shariff and A. Leonard, "Vortex rings", Ann. Rev. Fluid Mech. **24**, 235-279 (1992).

[50] S. Shetty, X. Assay-Davis and P. Marcus, "On the interaction of Jupiter's Great Red Spot and Zonal Jet Streams", J. Atmos. Sci. **64** 4432-4444 (2007).

[51] S. Stanaway and B. Cantwell, "A numerical study of viscous vortex rings using a spectral method", NASA TM 101041 (1988).

[52] A. Weigand and M. Gharib, "On the evolution of laminar vortex rings", Exp. Fluids **22** 447-457 (1997).

[53] J. Weiss, "The dynamics of enstrophy transfer in 2-dimensional hydrodynamics", Physica D. **48**, 273-294. (1991).

[54] C. Willert and M. Gharib, "Digital particle image velocimetry", Exp. Fluids **10**, 181-193 (1991).